USGS
science for a changing world

Prepared in cooperation with and funded in part by the Arctic Landscape Conservation Cooperation (ALCC)

Changing Storm Conditions in Response to Projected 21st Century Climate Change and the Potential Impact on an Arctic Barrier Island–Lagoon System—A Pilot Study for Arey Island and Lagoon, Eastern Arctic Alaska

Open-File Report 2020–1142

U.S. Department of the Interior
U.S. Geological Survey

Cover: View from the western end of Barter Island looking southeast toward Arey Lagoon. Image and other oblique images of the North Slope of Alaska are available for download at http://pubs.usgs.gov/ds/436/ (Gibbs and Richmond, 2009).

Changing Storm Conditions in Response to Projected 21st Century Climate Change and the Potential Impact on an Arctic Barrier Island–Lagoon System—A Pilot Study for Arey Island and Lagoon, Eastern Arctic Alaska

By Li H. Erikson, Ann E. Gibbs, Bruce M. Richmond, Curt D. Storlazzi, Ben M. Jones, and Karin A. Ohman

Prepared in cooperation with and funded in part by the Arctic Landscape Conservation Cooperation (ALCC)

Open-File Report 2020–1142

U.S. Department of the Interior
U.S. Geological Survey

U.S. Department of the Interior
DAVID BERNHARDT, Secretary

U.S. Geological Survey
James F. Reilly II, Director

U.S. Geological Survey, Reston, Virginia: 2020

Suggested citation:
Erikson, L.H., Gibbs, A.E., Richmond, B.M., Storlazzi, C.D., Jones, B.M., and Ohman, K.A., 2020, Changing storm conditions in response to projected 21st century climate change and the potential impact on an arctic barrier island–lagoon system—A pilot study for Arey Island and Lagoon, eastern Arctic Alaska: U.S. Geological Survey Open-File Report 2020–1142, 68, p., https://doi.org/10.3133/ofr20201142.

Associated data for this publication:
Erikson, L.H., Gibbs, A.E., Richmond, B.M., Jones, B.M., Storlazzi, C.D., and Ohman, K.A., 2020, Modeled 21st century storm surge, waves, and coastal flood hazards, and supporting oceanographic and geological field data (2010 and 2011) for Arey and Barter Islands, Alaska and vicinity: U.S. Geological Survey data release, https://doi.org/10.5066/P9LGYO2Q.

ISSN 2331-1258 (online)

Acknowledgments

Funding for this study was provided by the Arctic Landscape Conservation Cooperative (ALCC), and we wish to thank ALCC's Philip Martin and Jennifer Jenkin for collaborative support and discussions that sharpened our thinking and improved our overall study.

We thank the U.S. Geological Survey Coastal and Marine Hazards and Resources Program.

We also acknowledge the World Climate Research Programme's Working Group on Coupled Modeling, which is responsible for CMIP5, and we thank the climate modeling groups (listed in table 4 of this report) for producing and making available their model output.

The U.S. Department of Energy's Program for Climate Model Diagnosis and Intercomparison provides coordinating support and led development of software infrastructure in partnership with the Global Organization for Earth System Science Portals for CMIP.

Contents

Figures

Tables

Conversion Factors

International System of Units to U.S. customary units

Multiply	By	To obtain
	Length	
micrometer (μm)	0.00003937	inch (in.)
millimeter (mm)	0.03937	inch (in.)
centimeter (cm)	0.3937	inch (in.)
meter (m)	3.281	foot (ft)
kilometer (km)	0.6214	mile (mi)
meter (m)	1.094	yard (yd)
	Area	
square meter (m^2)	0.0002471	acre
square kilometer (km^2)	247.1	acre
square meter (m^2)	10.76	square foot (ft^2)
square kilometer (km^2)	0.3861	square mile (mi^2)
	Rate	
meter per second (m/s)	3.281	foot per second (ft/s)
millimeter per year (mm/yr)	0.03937	inch per year (in/yr)
meter per year (m/yr)	3.281	foot per year ft/yr)
millimeter per decade (mm/decade)	0.003937	inch per year (in/yr)
centimeter per decade (cm/decade)	0.03937	inch per year (in/yr)
meter per decade (m/decade)	0.3281	foot per year ft/yr)
cubic meter per day (m^3/d)	35.31	cubic foot per day (ft^3/d)
cubic meter per day (m^3/d)	264.2	gallon per day (gal/d)
	Pressure	
kilopascal (kPa)	0.009869	atmosphere, standard (atm)
kilopascal (kPa)	0.01	bar
kilopascal (kPa)	0.2961	inch of mercury at 60 °F (in Hg)
kilopascal (kPa)	0.1450	pound-force per inch (lbf/in)
kilopascal (kPa)	20.88	pound per square foot (lb/ft^2)
kilopascal (kPa)	0.1450	pound per square inch (lb/ft^2)
	Density	
kilogram per cubic meter (kg/m^3)	0.06242	pound per cubic foot (lb/ft^3)

Temperature in degrees Fahrenheit (°F) may be converted to degrees Celsius (°C) as follows:

$$°C = (°F - 32) / 1.8.$$

Datum

Altitude and elevation, as used in this report, refers to distance above approximate mean sea level. There is no established vertical geodetic, nor tidal datum for much of Arctic Alaska, including where this study took place. For this study, a temporary marine pressure sensor was installed for the duration of the 2011 open water season. A mean sea level elevation was determined using this data and is considered a proxy for a local mean sea level datum in the study area (hereafter referred to as MSL). All vertical measurements are referenced to that reference elevation.

All times are reported in Coordinated Universal Time UTC. The Alaska standard time (AKST) zone is AKST= UTC minus 9 hours.

Horizontal coordinate information is referenced to North American Datum of 1983 (NAD 83).

Variables and Abbreviations

H_s	significant wave height
L	wavelength
T_p	peak wave period
D_p	peak wave direction?
d	depth
TWL	total water level
R	wave run-up
SS	storm surge
$rSLR$	relative sea-level rise
η_{tide}	astronomic tide levels
SLA	sea level anomalies
η_Q	riverine water levels
BCC	Beijing Climate Center, China
CMIP	Coupled Model Intercomparison Project
CTD	conductivity, temperature, and depth
D3D	Delft3D
DEM	digital elevation model
GCM	global climate model
GDD	growing degree day
IBE	inverse barometer effect
INM	Institute for Numerical Mathematics, Russia
IPCC	Intergovernmental Panel on Climate Change
JD	Julian day
MIROC	Model for Interdisciplinary Research on Climate, Japan
MSL	mean sea level
NARR	North American Regional Reanalysis
NCAR	National Center for Atmospheric Research

NCDC	National Climatic Data Center
NCEP	National Centers for Environmental Prediction
NOAA	National Oceanic Atmospheric Administration
NOS	National Ocean Service
RCP	representative concentration pathway
SLP	sea level pressure
USGS	U.S. Geological Survey
WW3	WaveWatchIII

Changing Storm Conditions in Response to Projected 21st Century Climate Change and the Potential Impact on an Arctic Barrier Island–Lagoon System—A Pilot Study for Arey Island and Lagoon, Eastern Arctic Alaska

By Li H. Erikson,[1] Ann E. Gibbs,[1] Bruce M. Richmond,[1] Curt D. Storlazzi,[1] Ben M. Jones,[2] and Karin A. Ohman[3]

Executive Summary

Arey Lagoon, located in eastern Arctic Alaska, supports a highly productive ecosystem, where soft substrate and coastal wet sedge fringing the shores are feeding grounds and nurseries for a variety of marine fish and waterfowl. Arey Lagoon is partially protected from the direct onslaught of Arctic Ocean waves by the Arey Barrier Island chain (Arey Island) which provides additional important habitat for migratory shorebirds and waterfowl. In this work, the stability of Arey Island and its ability to mitigate ocean-derived flooding of low-lying tundra and coastal wet sedge along the fringes of Arey Lagoon were evaluated with respect to sea-level rise and changing storm conditions brought about by 21st century climate change.

Historical shoreline change rates dating back to 1947 and computed from T-sheets, satellite imagery, and airborne lidar were used to assess the stability of the mainland shores and Arey Island. In order to evaluate future stability and the ability of Arey Island to mitigate wave energy delivery to the lagoon, hindcast (probable past conditions: 1981–2010) and future coastal storm conditions (2011–2100) were simulated with a suite of numerical models. Model simulations were further used to quantify anticipated changes in flood frequency, duration, and extent for Arey Island and coastal wet sedge areas along the mainland shores of Arey Lagoon.

Historical shoreline change results derived from satellite imagery, ground surveys, and digital elevation models show that the western part of Arey Island remained mostly stable (average long-term rate -0.1±0.3 meters per year [m/yr]), whereas the eastern part migrated to the southwest (landward) by as much as 900 m (at most 14.3 m/yr, since the late 1940s). Review of imagery spanning 64 years (1947 to 2011) suggests that the landward migration may have been driven in part by a series of breaching events followed by reformation and near reattachment of island sections. Wave and storm-surge projections modeled to the year 2035 were used to simulate morphodynamic change to assess the potential for increases in island migration rates or deterioration. Results indicate that the western part of Arey Island will remain reasonably stable, whereas the eastern section will continue to be subject to breaching and landward migration. The extent to which migration might continue depends on availability of sediment and accommodation space within the lagoon. Model simulations done as part of this study assume unlimited sediment supply. However, if sediment availability were limited, vertical accretion (for example by wave runup and aeolian transport) along the low-relief eastern section of Arey Island would be outpaced by sea-level rise, and much of the eastern part of the island chain would be fully submerged by the end of the century.

Model simulations indicate that extreme wave heights in deep water (>500 meters [m]), seaward of the continental shelf, will increase at a rate of 0.35 meters per decade for the representative concentration pathway (RCP) 4.5 (stabilizing emissions) and 0.49 meters per decade for the RCP8.5 (“business as usual”) climate scenarios through the year 2045. By the end of the 21st century, extreme wave heights might reach as high as 8 m but are expected to be on the order of 6±1 m based on the average of extremes from four different global climate models (GCMs).

In contrast to the offshore wave climate, there is no apparent temporal trend in extreme wave heights at the 10-m depth contour immediately offshore of Arey Island. This is likely a result of the broad continental shelf, which enables dissipation of wave energy, and limits higher wind-wave growth owing to the shallow water depths. Although there is no apparent trend, maximum significant wave heights are projected to reach 4.4 m by the end of the 21st century in the nearshore area, exceeding any previous events by approximately 0.4 m, as deemed by hindcast model runs.

Model hindcasts (simulations for which known or closely estimated inputs of past events are used as boundary conditions) indicate that the 1980s and early 1990s were relatively quiescent with a storm count of less than two per

[1]U.S. Geological Survey.

[2]University of Alaska Fairbanks (formerly with U.S. Geological Survey)

[3]Michael Baker International (formerly with U.S. Geological Survey).

year. This can, at least in part, be attributed to the shorter open-water season, which has more than doubled since that time from about 50 days in the early 1980s to approximately 120 days in the 2010s. The first and last days of the open-water season in the vicinity of Arey Island were derived from weekly satellite data for the years 1981 through 2013 and GCM projections for the remaining years until 2100. Results from satellite imagery and four GCMs indicate that the onset of the open-water season will become 2 days earlier per decade and the end will become 4 days later per decade. The open-water season will extend into late November by the year 2100. Because storm intensity and frequency are typically greater in late summer and early fall compared to the earlier open-water season months, the later refreeze increases the vulnerability of the coast to more frequent and extensive erosion and flooding.

Data analysis and model runs show that although storm waves are most prominent from the northeast and northwest, storms from the west and northwest cause the greatest barrier island breaching and Arey Lagoon mainland flooding. This is because westerly winds elevate storm-surge water levels, allowing waves to reach farther inland. Storms from the east and northeast quadrant yield a water-level setdown (water moves away from the shore) in response to the Coriolis force.

Extreme storm-surge levels, for the RCP4.5 scenario, are projected to increase at a rate of 0.15 meters per decade for the period of 1981 to 2050; thereafter, no trend is apparent. The timing of increasing surge levels and subsequent leveling corresponds to radiative forcing of the RCP4.5 scenario, which assumes stabilization near the middle of the century. Storm-surge modeling was not done for the more severe RCP8.5 scenario. Slightly more than 20 percent of the projected increases in extreme surge levels are attributed to sea-level rise, which was accounted for in all model runs by raising (projections) or lowering (hindcasts) the water level by 0.03 meters per decade relative to 2010, the midperiod year of the digital elevation model (DEM) used in all simulations. The 5-m-horizontal-resolution DEM was constructed from airborne lidar and bathymetry data collected in 2009 through 2011.

Extreme surge levels, computed with the numerical model, range from 0.5 to 1.3 m and 1.0 to 2.0 m above mean sea level (MSL) for the hindcast and projected periods, respectively. The historical surge values (maximum 1.3 m above MSL) are comparable to measurements at the nearest tide station located in Prudhoe Bay about 170 kilometers (km) west of Arey Lagoon, where the maximum event recorded since 1990 is 1.4 m above MSL (August 11, 2000).

Assuming that Arey Island will remain dynamically stable (migrate, widen, shrink, breach and reform, but continue to protect the mainland from wave energy), the potential for storm surge and sea-level rise to flood the shores of Arey Lagoon was evaluated by applying numerically simulated water levels to the DEM, and ensuring hydraulic connectivity between ocean and land. Flood maps were generated for the 25-year and maximum events of the first and latter halves of the 21st century. The 25-year (1.70 m) and maximum (1.95 m) events are slightly higher (0.10 and 0.15 m) for the first half of the century compared to the latter half (RCP4.5). Because of the generally low relief, these extreme flood events translate to more than 9 square kilometers (km^2) of flooded tundra, much of which consists of salt-intolerant vegetation (Jorgenson and others, 2002).

Bi-monthly flood extents, including sea-level rise, that might be expected to maintain halophytic vegetation were estimated by extracting the second highest monthly modeled water level and computing the median value on a per decade basis from the early 1980s through 2100. Median monthly water levels range from 0.44 m above MSL (referenced to the year 2010) for the 1981–1990 decade to 0.77 m above MSL for the 2091–2100 decade. When applied to the DEM, this translates to an area twice as large by the end of the century compared to 1981–1990 (~2.21 km^2 to ~4.43 km^2 along Arey Lagoon shores).

By combining the frequency and magnitude of extreme storm surge events with the progression of monthly inland flood extents modeled for the 21st century, it might be possible to identify areas along this stretch of coast where non-saline vegetation communities will be inundated and salt tolerant vegetation may take over. Permafrost thawing, subsidence, erosion, and sedimentation rates are other critical areas of future research that are needed to more accurately predict wetland gains, losses, and habitat-type conversions. Although specific factors will differ for other barrier islands and lagoons in the Arctic, it is expected that the findings in this report, particularly those regarding changes in oceanographic conditions, are generally applicable to the approximately 540 km of barrier islands and lagoons (Jorgenson and Brown, 2005) along the U.S. and Canadian shores of the Beaufort Sea.

Introduction

The Beaufort Sea coast of eastern Alaska is characterized by nearly 600 kilometers (km) of shallow (<5 meters [m]) estuarine lagoons connected to the ocean by one or more restricted inlets cut through barrier islands (Jorgenson and Brown, 2005; Gibbs and Richmond, 2015). The lagoons are typically fed by streams and small rivers that drain northward across the Arctic coastal plain from the Brooks Range. Depending on the hydrologic balance between freshwater inputs and ocean water exchange past the barrier islands, lagoon salinity can vary from nearly fresh to hypersaline.

The lagoons, including adjacent mainland areas and barrier islands, are highly productive ecosystems that support a variety of habitats. Birds from six continents nest and forage in river deltas, on barrier islands and spits, in lagoons, and along the shoreline during the summer months (Craig and Haldorson, 1981; Griffiths and Dillinger, 1981; Johnson and Richardson, 1981; Derksen and others, 1982; Truett, 1984; Kendall, 2005; US Fish and Wildlife Service, 2012). Large

waterfowl (for example, brant) are particularly abundant and highly value wet sedge meadows and salt marshes that fringe the lagoon shores. Whereas salt marshes are patchy and narrow owing to the small tide range (~0.15 m, National Oceanic and Atmospheric Administration [NOAA], 2015), wet sedge meadows are more ubiquitous and tolerate less frequent salt water exchange (see Viereck and others, 1992, for descriptions of wet sedge meadows). For example, saline-dependent vegetation valued by brant and other geese is maintained by flooding one to two times per month, whereas other slightly saline meadows rely on approximate annual saltwater flooding.

In addition to habitats fringing lagoon shores, soft substrate within the lagoons provides physical refuge from predation and serves as nursery and feeding ground for marine fish. In contrast to the open coast, organic materials (benthic and suspended matter) within the lagoons are largely contributed by terrestrial sources (Dunton and others, 2006). This difference in sediment composition highlights the diversity in habitat offered by lagoons and the importance of the limited sediment exchange between lagoons and the open coast.

Crucial to maintaining the diverse ecosystems of a coastal lagoon system is the barrier. Barrier islands (and spits connected to land) provide nesting grounds for birds, modulate the exchange of sediment and fresh and saltwater, reduce wave energy and consequential disturbance of lagoon benthic communities, and protect the mainland from ocean waves. Barrier islands along Alaska's Beaufort Sea coast are primarily formed by wave action and, compared to wave dominated barrier islands in other climates, their features predominantly reflect storm conditions rather than long-period ocean swell (Stutz and Pilkey, 2011).

An issue affecting the balance of these northern ecosystems is the warming Arctic climate. In response, permafrost is thawing, hydrologic processes are changing, and biological systems are evolving (Hinzman and others, 2005). The combination of sea-level rise (for example, Sultan and others, 2011; Yin, 2012), declining sea-ice extents (Stroeve and others, 2007), and increasing storm intensity and frequency (Bengtsson and others, 2006; Atkinson, 2005) likely foreshadow changes in the wave climate and total water levels at the shore, both of which directly influence the extent and frequency of flooding and consequently habitat availability within a lagoon and adjoining mainland shore.

During periods of high storm surge and waves (see section on clarification of terms for a description of these physical processes), water may move rapidly over the barrier in a process called overwash, which delivers sediment eroded from the front of the barrier onto the back side of the barrier and into the lagoon (Wilby and others, 1939). Increasing storm intensity, combined with sea-level rise, could yield more frequent barrier breaching (breakthroughs) resulting in deterioration of the barrier, thereby reducing its capacity to modulate the exchange of sediment and water and buffer the lagoon and mainland from incoming wave energy. Lagoon substrate could experience increased sedimentation rates from overwash fans and altered sediment transport patterns that would bring in higher quantities of marine sediment and thus reduce the relative proportion of terrestrial organic material of the seabed sediments.

If the protective ability of a barrier is decreased, low-lying mainland habitats may become more vulnerable to flooding of greater frequency, depth, and extent. Along Smith River and Garry Creek estuaries near the western end of the Alaska's Beaufort Sea coast, for example, historical non-saline vegetation communities have already shifted toward halophytic (salt-tolerant) conditions. Tape and others (2013) analyzed soil stratigraphy and vertical imagery and found that sedimentation of marine sediments allowed high-quality goose-forage plants to expand inland resulting in a redistribution of geese populations. Data suggested that the vegetation changed in the 1970s and that the change evolved over at least a decade. They attributed the change to surface deflation by permafrost thaw and increased marine flooding brought on by greater storm frequency and intensity (Arp and others, 2010).

The ice-rich permafrost soils and low relief of the Arctic coastal environment makes vegetation highly sensitive to saltwater flooding. Saltwater flooding can kill typical tundra vegetation (Reimnitz and Maurer, 1979), and repeated inundation likewise increases thermal conductivity, potentially triggering permafrost degradation and subsidence (Tape and others, 2013), which in turn makes the surface more prone to flooding. Reimnitz and Maurer (1979) documented wrack lines (lines of dried debris deposited by marine flood events) along the Alaska's Beaufort Sea coast following a storm in September 1970. Because of varied geography (coastline shape and orientation), distance of storm center from the shore, and non-uniform but overall lowland elevation, the landward position of the wrack lines ranged from 20 to 5,000 m from shore (total surge height was estimated to be 1.4 to 3 m above mean sea level). The farthest inland extent was observed at the Kuparok River delta and the Colville River Delta. Salt-killed areas from the 1970 storm were still mostly dead and devoid of colonizing halophytes 30 years later (in the early 2000s) on the Colville River Delta (Jorgenson and others, 1996).

Changes in shoreline morphology and flooding will likely alter the composition of habitats supported by Arctic coastal lagoons and may lead to new biological succession trajectories. Will these changes provide coastal habitat types that fish and fauna can adapt to or will the changes outpace the rate at which biological communities can respond to the new environmental conditions? Answers to these questions fundamentally depend on having an understanding of how the physical environment will change. To this end, this study aims to assess the stability of barrier islands and vulnerability of coastal wet sedge and low-lying tundra to flooding under the provision of sea-level rise and changing storm conditions brought about by climate variability in the 21st century (fig. 1).

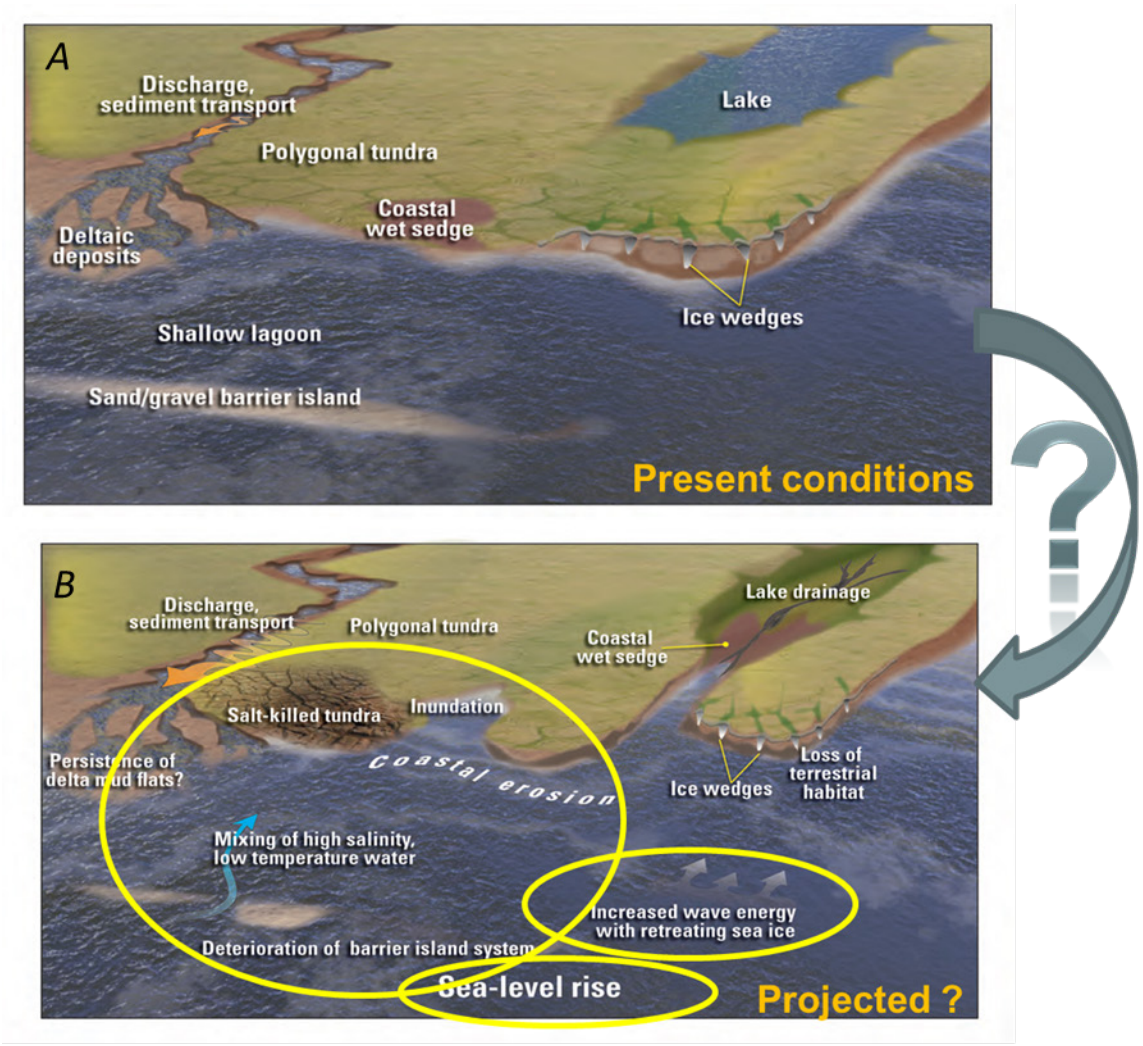

Figure 1. Schematic of Arctic coastal landscape, current (*A*) and potential projected conditions in response to Arctic warming (*B*). Ovals highlight the topics of study addressed in this report (for example, increased wave energy, sea-level rise, and potential deterioration of the barrier island, salt-killed tundra, and inundation. Figure modified from Martin and others, 2009, figure 4.1.

Arey Island and Lagoon, located approximately 100 km west of the United States-Canada border, along the Beaufort Sea coast and within the Arctic National Wildlife Refuge, was selected as a pilot study site. Specific objectives of this study are as follows:

- Quantify historical shoreline change rates of Arey Island and the fringing mainland coastline within Arey Lagoon
- Project ocean storm conditions (magnitude and frequency) for the 21st century and assess changes with respect to past conditions
- Evaluate the future stability of Arey Island and its capacity in modulating wave energy reaching coastal wet sedge areas
- Evaluate the effects of sea-level rise and changes in storm conditions on the frequency and extent of intermittent flooding and permanent inundation of low-lying tundra and coastal wet sedge areas valued by large waterfowl.

The remainder of this report begins with a section on that provides descriptions and illustrations of physical processes and related terminology relevant for understanding the cause and effect of atmospheric and oceanographic forcings relevant to barrier-island stability and coastal flood vulnerability. A description of the study area is then presented followed by an overview of data and methods. Findings for each of the objectives listed above are then presented in the results section and lastly summarized along with concluding remarks in the final section.

Clarification of Key Terms

Wind-Generated Waves

Wind-generated waves are surface gravity waves that form when winds blow over the open-water surface and transfer wind energy into the water column. Ocean waves can be formed by several disturbing forces (tectonic activity, ships, and so on) that transfer energy to the water column, but this report only concerns wind-generated waves, the most common wave type in the ocean.

All wind waves grow from capillary waves (for example, Garrison, 1996). Capillary waves form as wind friction stretches the water surface and as the surface tension tries to restore the water surface to smoothness. The rough water surface deflects the surface wind, slows it, and causes wind energy to be transferred into the water moving the capillary wave crest forward. Increasing energy in the water surface expands the circular orbits of water particles in the direction of the wind, and eventually capillary waves become wind waves when gravity supersedes capillary action as the restoring force. In the process, simultaneous wind waves of many heights and lengths form, resulting in a chaotic looking sea surface. The irregular peaked waves in the area of wave formation are termed seas. Because waves with longer wavelengths (>~200 m) move faster than waves with shorter wavelengths, they leave the area of wave formation sooner. Mature waves from a storm sort themselves into groups having similar wavelengths and speeds. The process of wave separation or dispersion produces the familiar smooth undulations of the ocean called swell. Swell waves often move thousands of kilometers from a storm to the shore.

Because wind waves are seldom monochromatic but instead have varying heights and lengths, it is convenient (and usually sufficient) to describe wave conditions with four statistical descriptors: significant wave height, H_s, represented by the mean of the highest one-third of waves; wavelength, L, equal to the distance between consecutive wave crests or troughs; peak period, T_p, time of travel of the highest energy wave; and D_p, the peak cardinal direction of maximum wave energy propagation (fig. 2). In deep water, wave height, period, and length are affected by windspeed, wind duration (how long the wind blows), and fetch, the distance over water that the wind blows in a single direction.

In the open ocean, waves transmit energy, not water mass. In water depths (d) shallower than half the wavelength ($d < 1/2L$) the waves begin to be influenced by the bottom. As the depth decreases, the transport of water mass increases proportionally, and significant wave height increases until some point where the ratio of H_s/d exceeds a threshold and the waves start to break and rapidly dissipate energy. In very

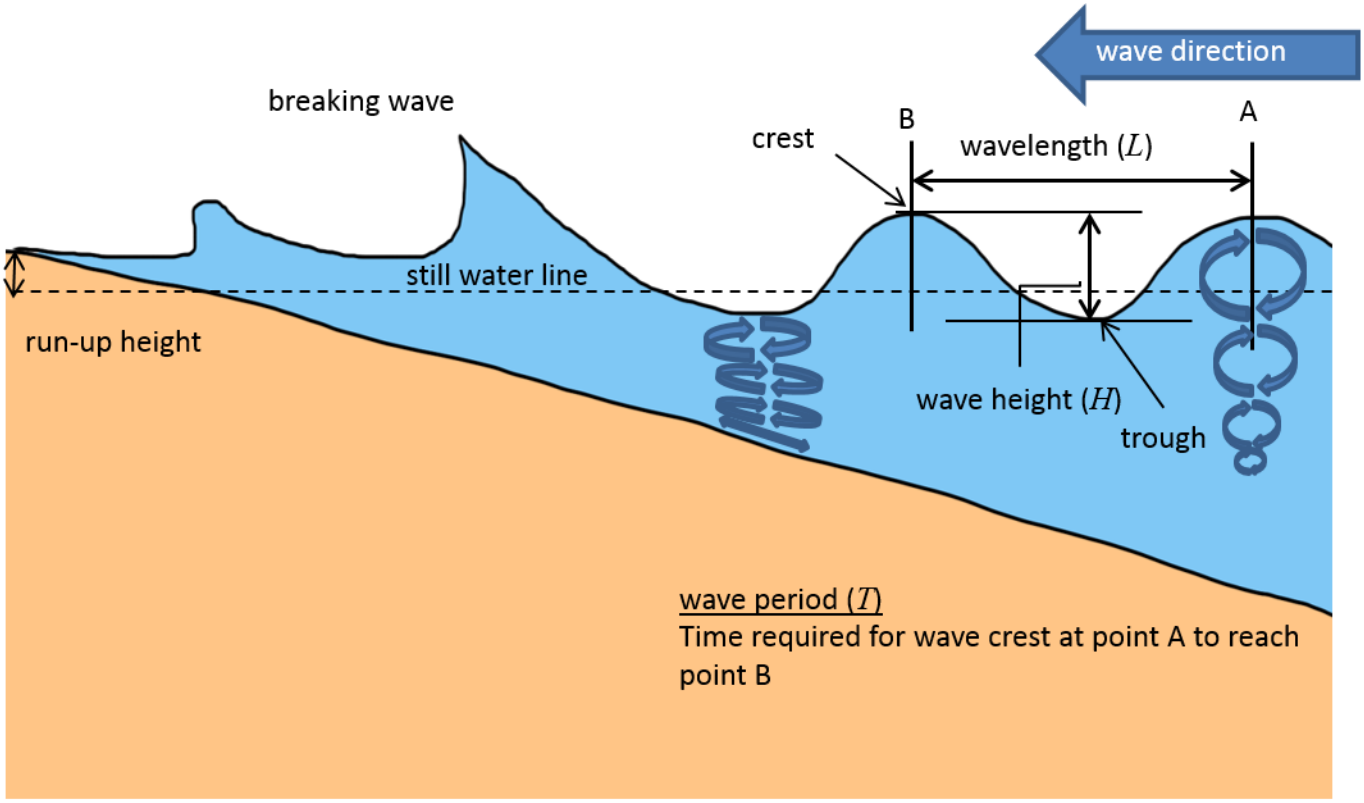

Figure 2. Schematic diagram illustrating wave characteristics.

shallow water (surf zone) this process becomes dominant over all other processes. When waves are breaking, they carry water shoreward. As they break, the water particles move toward the shore with considerable momentum that allows water to run up a sloping beach. The total runup height is the summation of two dynamically different processes: (1) setup, the time-averaged water level at the shore in response to breaking waves, and (2) swash, the time-varying fluctuations about the temporal mean (Stockdon and others, 2006; Longuet-Higgins and Stewart, 1964; Hunt, 1959).

Storm Surge

Storm surges are temporary changes in coastal water levels caused by high winds and strong atmospheric pressure gradients. Lower atmospheric pressure physically draws water levels up in what is called the inverse barometer effect (IBE). This effect occurs even under pack ice (Wise and others, 1981). In deep water, a 1-millibar decrease in sea level pressure will cause a water-level rise of about 1 centimeter (cm). This can be important in the Alaskan Beaufort Sea where atmospheric pressures can drop to 940 hectoPascals (hPa), a deviation of more than 50 hPa or 50 cm of water when compared to "normal" pressures (~1,012 hPa).

The frictional drag of strong winds blowing over water creates a surface stress that "pushes" a mass of water in the downwind direction. Stronger and longer periods of wind stress and larger areas of fetch allow for a greater mass of water to be entrained, which in turn yield larger water-level changes at the shore. Besides windspeed and fetch, several other factors influence storm surge levels at the coast: ground speed of the storm, relative angle between the storm track and coast, shape of the coastline, presence of barrier islands, and bathymetry. Areas with a narrow continental shelf produce low surge height as excess water is driven up the shelf but can rapidly flow back to the deeper areas. In regions with a wide, gently sloping shelf, like the Beaufort Sea, water is piled up and pushed upward against the coast.

Additionally, the Coriolis force, influenced by the rotation of the Earth, causes water to deflect to the right in the northern hemisphere (left in the southern hemisphere). Surface currents generated by strong winds and under the influence of Coriolis are directed at about a 30° angle to the right of the wind direction (Williams and others, 1973). Each layer of water acts on the layer below which also is deflected to the right but under weaker force owing to drag between water column layers. In deep water, the resulting pattern is a mass transport of water nearly 90° to the right of the wind direction and the effect is known as the Ekman spiral. Over continental shelves where seabed friction plays a controlling role, the effect is lessened and the transport is closer to 45° to the right of the wind direction. Because the Beaufort Sea continental shelf is wide, relatively shallow, and located in the high-latitude northern hemisphere, storms from the west (winds blowing to the east) yield elevated water levels along the Alaska coast. Westerly winds and waves create currents moving toward the east that are deflected to the right by Coriolis, onto the shallow continental shelf, pushing the water up to the coast. The opposite occurs with easterly storms (winds blowing from the east). Easterly storms cause the currents to move toward the west which are deflected to the right and offshore, yielding a set down or drawdown of water from the coast. Results from model simulations of constant westerly and easterly 20 meters per second (m/s) winds illustrate the point (fig. 3).

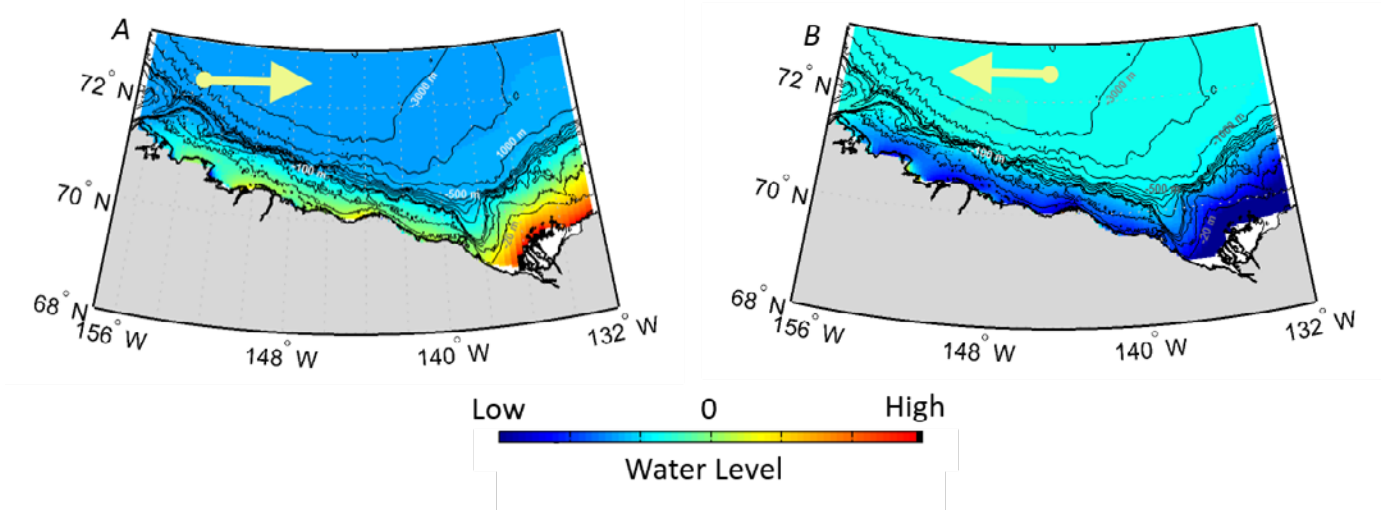

Figure 3. Example of surge response to wind direction and Coriolis force at high northern-hemisphere latitudes. Net water transport is 90° to the right of the wind direction in the northern hemisphere. *A*, Westerly winds promote a positive storm surge along the coast. *B*, Easterly winds drive waters offshore and reduce water levels along the coast. Arrows depict constant wind direction (due west and east, respectively) for a constant windspeed of 20 meters per second over one day. Bathymetric contours are at 1,000 meters (m), followed by 500, 100, and 20 m intervals closer to shore.

Notably the term "storm tide" is sometimes used; however, it should not be used interchangeably with "storm surge" as storm tides refer to the combination of a storm surge and astronomic tides (regular deterministic water-level changes owing to planetary orbits). In the Alaskan Beaufort Sea, storm surges (1–3 m) are an order of magnitude larger than astronomic tides (~0.15 m).

Total Water Levels

The combination of wave run-up (R), storm surge (SS), relative sea-level rise (rSLR) (accounting for sea-level rise and land subsidence or uplift), astronomic tides (η_{tide}), and other factors such as longer term sea-level anomalies (SLA) and riverine water levels (TWL) contribute to the total water level (η_Q) at the shore (fig. 4) using the following equation:

$$TWL = R + SS + \eta_{tide} + rSLA + \eta_Q \quad (1)$$

Persistent sea-level anomalies lasting months to years result from prolonged but temporary changes in water temperature (thermal expansion), salinity variations (density changes), coastal currents, and large-scale atmospheric patterns. Analysis of tide-gauge data on the North Slope of Alaska suggests sea-level anomalies can elevate water levels by as much as 0.25 m (Sultan and others, 2011). The last term in equation 1 represents amplified water levels that might occur at the confluence where elevated coastal water levels propagate upstream and meet with seaward-directed fluvial flows causing a "backflow". Because wave run-up and storm surge are episodic and typically larger than the combined effect of the remaining terms, the primary focus of this study is on these storm-related contributions to the total water level. For the case of decadal flood maps generated as part of this study, sea-level rise is also added to the total water level. However, in the case of joint occurrence with high astronomic tide and sea-level anomalies, total water levels could be tens of centimeters higher.

Barrier Island Overwash and Breaching

Barrier island overwash is the flow of water and sediment over a beach crest that does not directly return to the originating water body (for example, the ocean) (Donnelly and others, 2004). Overwash begins when wave run-up, which usually coincides with storm surge and works to elevate the height of waves and run-up, exceeds the local beach or dune crest height (see fig. 5 for example of overwash feature across Arey Island). As the water level in the ocean rises such that the beach or dune crest is inundated, a steady sheet of water (sheetwash) and sediment (washover) runs over the barrier. Sediment transported by overwash can be deposited onto the upper beach or behind the barrier in the lagoon. Overwash primarily occurs in association with large storms and can be a precursor to breaching by initiating erosion of the beach face, lowering

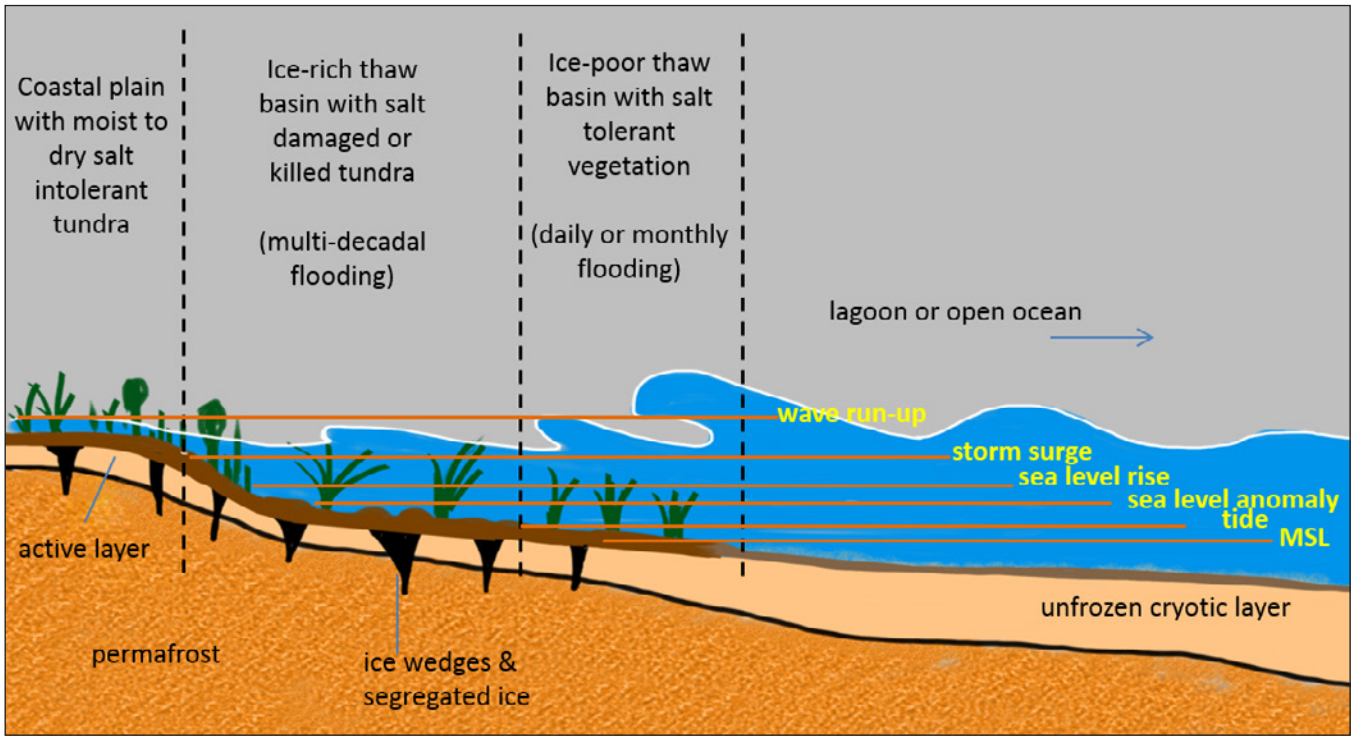

Figure 4. Schematic cross section of Arctic coastal wet sedge and tundra subject to flooding and inundation by sea water. Time variation of the total water level, which constitutes any combination of astronomic tides, sea-level rise, storm surge, and wave run-up, dictates the extent, frequency, and duration of flooding. Discrete vegetation and basin descriptors modified from Jorgenson and Marcot (2012) and Tape and others (2013). MSL, mean sea level.

the crest elevation of the beach, and transporting sediment from the beach and back beach into the bay (Kraus and others, 2002; Kraus and Walmsely, 2003). Overwash is commonly cited as the primary mechanism of barrier island migration (for example, Hequette and Ruz, 1991; Morton and Sallenger, 2003) but changes in along-shore sediment transport patterns and sea-level rise may also contribute to migration up the continental shelf (Kraft and others, 1973).

Figure 5. Aerial image showing overwash feature on Arey Island. Image from Google Earth, 2004.

Study Area

Regional Setting

The study area is located along Alaska's Beaufort Sea coast, at the edge of the Arctic Coastal Plain, a broad, gently sloping tundra-covered surface that extends from Cape Beaufort in the Chukchi Sea into Canada (fig. 6). The Arctic Coastal Plain is composed primarily of unconsolidated Quaternary silts, sands, and gravels of marine, alluvial, fluvial, glaciofluvial, and aeolian origin (Black, 1964; Hopkins and Hartz, 1978). A surficial layer (2–3 m thick) of Late Pleistocene and Holocene peaty/muddy thaw-lake sediment covers most of the region (Hopkins and Hartz, 1978). Coastal sediments become coarser and coastal bluffs become higher from west to east (Reimnitz and others, 1988; Barnes and Rollyson, 1991). Coarse sediment, including gravel, dominates most of the barrier islands. Earlier studies (Arnborg and others, 1966; Barnes and Reimnitz, 1974) reported that rivers do not deliver coarse material to the coast or barrier islands; sand and gravel loads are deposited a few kilometers inland, and only easily re-suspended fine sand, silt, and clay reach the lagoons and estuaries. Because wave energy is relatively low and the open-water season is short, the total amount of littoral sediment transport along the beaches and barrier islands is considered to be relatively small compared to lower latitude coasts (Hopkins and Hartz, 1978).

The region is in a zone of continuous permafrost, where the ground is perennially frozen to depths of several hundred meters, except for a thin surficial seasonal thaw layer and a layer under deep lakes and river channels (Rawlinson, 1993; Jorgenson and Brown, 2005). Ground ice typically occupies

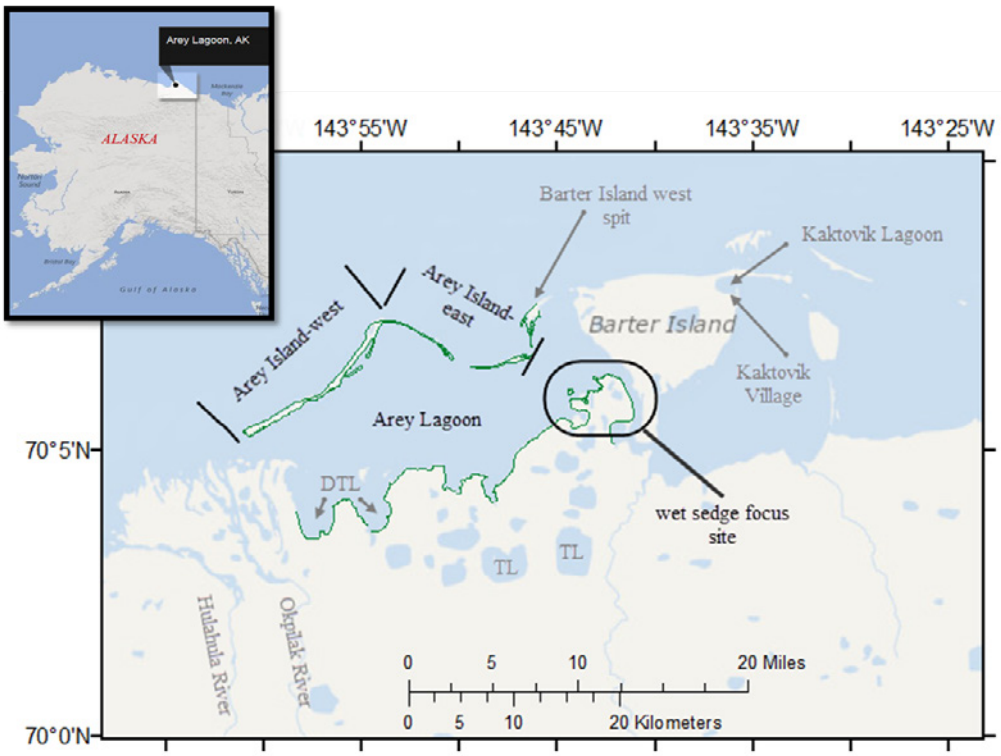

Figure 6. Map of the study area showing Arey Island west and east, Arey Lagoon, and the adjoining mainland coast, eastern Arctic Alaska. Study site consists of a coastal wet sedge focus site, thermokarst lakes (TL), and drained thermokarst lakes (DTL).

60–80 percent of the volume of near-surface deposits (Brown and Sellman, 1973), and it is a major factor contributing to the high coastal erosion rates (Barnes and others, 1992).

The continental shelf of the Beaufort Sea is approximately 100 km wide. Marine sediment is dominated by mud, possibly transported from the Mackenzie River in Canada over the past 15,000 years (Harper and others, 1988), and shows signs of ice gouging (long narrow furrows caused by ice drifting into shallow waters) (Rearic and others, 1990).

Coastal waters typically begin freezing in late September or October, with ice first forming on the more sheltered and brackish lagoons and thickening throughout the winter to a maximum of approximately 2 m (Dunton and others, 2006). Shorefast ice is typically anchored to the coast along the 2-m isobath (Reimnitz, 2000) and extends seaward to about 20-m water depth (Barnes and others, 1984; Reimnitz and Kempema, 1984) where it joins the multiyear pack ice. The pack ice is a conglomerate of older and reformed floating ice pieces of various sizes, ages, and origins. September is typically the month when the pack ice is farthest from shore and thus has the greatest fetch (distance over which the wind blows) for wave growth and wind-induced storm surge. The distance from shore to the edge of the pack ice has increased dramatically in recent years contributing to increased storminess. Satellite records show that the median fetch due north of Arey Lagoon was approximately 200 km between 1979 and 2000; in 2007 and 2012 the September fetch had increased to 450 and 1,000 km, respectively (Brodzik and Armstrong, 2013).

Most of the shoreline change occurs between late July and the onset of shorefast ice. Starting in late July to mid-August, weather low-pressure cells originating in the Pacific Ocean or Chukchi Sea traverse eastward across Alaska and the Beaufort Sea bringing with them high winds that can generate storm surges possibly as high as 3 m and waves as high as 6 m (Hume and Schalk, 1967; Wiseman and others, 1973; Hopkins and Hartz, 1978; Swail and others, 2007).

Astronomic tides are small in the region. The closest continuously recording tide gauge is at Prudhoe Bay (170 km west of Arey Lagoon), which has a diurnal range of 21 cm (NOAA, 2016). Because of the low tidal range, water level is influenced more by storms and atmospheric changes (background winds and sea level pressures) than by astronomical tides.

Local Setting

The areas adjacent to Arey Lagoon include a barrier island chain, a river delta (of the glacially fed Okpilak and Hulahula Rivers), and low-lying wet sedge tundra with ice-wedge polygonal networks and thermokarst lakes (fig. 6). Arey Lagoon and the adjacent coastline face northwest. Winds are most frequently from the east and southeast quadrants, whereas storm winds of consequence are primarily from the west to north. The lagoon is shallow (<1 m) and the bottom consists of very fine to coarse sediment. Presumably, much of the fine glacially derived sediment from the Okpilak and Hulahula Rivers settles in the lagoon.

The arcuate, chevron-shaped Arey Island barrier chain fronting Arey Lagoon presently consists of an east and a west section separated by a narrow inlet (fig. 6). Here we refer to the segmented chain as “Arey Island” for simplicity. Based on 2009 airborne light detection and ranging (lidar) data, the northeast-southwest trending section of the island (Arey Island-west) is approximately 5.6 km in length, varies between 60 and 350 m in width, and has mean and maximum elevations of 0.6 and 2.7 m above approximate mean sea level (MSL), respectively. The northwest-southeast trending section of the island (Arey Island-east) is also approximately 5.6 km in length, varies between 31 and 260 m in width (with the widest section being at the eastern terminus), is generally of lower relief compared to Arey Island-west (mean and maximum elevations of 0.2 and 1.9 m above MSL, respectively), and is bisected by a shallow pass that is less than 2 m deep and 1 km wide. The eastern part of the barrier island chain has experienced substantial morphologic change since 1947 and is very dynamic compared to the relatively stable western part of the island (see Shoreline Change section later in this report). Arey Island supports some low-lying vegetation. Wrack lines consisting of large logs and debris are pervasive on the island, commonly at locations of maximum elevation and bird nesting sites on the wider sections of the island (Kendall, 2005).

The fringing shores of Arey Lagoon are composed of drained and undrained thermokarst lakes and tundra. The soil and vegetation assemblages consist of wet germinated tundra dominated by sedges and grass with little moss or shrub cover. A coastal wet sedge area (~10-m width) frequented by migrating geese was selected as a focus site for this study (fig. 6). This site consists of numerous shallow brackish water ponds disconnected from the lagoon. As part of this study, the area was surveyed in 2011 and inspected for evidence of past flood events. Distinct wrack lines were widespread throughout the wet sedge focus site, indicating the occurrence of former extensive flood events.

Only limited data and anecdotal evidence on the relationship between shoreline change, storm surge, high wave events, and flooding potential were available prior to this study. Water levels, wave characteristics, and water quality parameters do not appear to have been measured previously within Arey Lagoon. Water levels were measured on at least two separate occasions in Kaktovik Lagoon, abutting the village of Kaktovik on the opposite side of Barter Island; August–October 2008 (NOAA, 2008) and September 2009–September 2010 (T. Jorgenson, verbal communication, 2010). No major storms passed the area during either of these measurement campaigns; maximum water levels from each campaign only reached 0.51 m (October 17, 2008) and 0.41 (August 3, 2010) above MSL. The closest continuously operating water-level gauge is at Prudhoe Bay (170 km west of Arey Lagoon). The gauge has been in operation since 1990 (NOAA, 2016) where the maximum event recorded was 1.4 m above MSL on August 11, 2000 (from astronomic tides and storm surge). The only other source of data on storm surge heights is inferred from the landward position of wrack lines following a storm in

1970; from these observations and elevation data available at the time, Reimnitz and Maurer (1979, fig. 6) estimated a maximum flood level of 2.4 m above MSL in the study region. However, as noted by Reimnitz and Maurer, driftwood lines do not necessarily mark the highest water level of a storm surge—it may have been higher or lower. In areas where the shore is exposed to waves and the nearshore slope is steep, wave run-up can be considerable, and driftwood comes to rest at an elevation representing the sum of storm surge and maximum wave run-up.

Data and Methods

Historical Shoreline Positions

Historical shoreline positions were delineated using 1947 and 1987 National Ocean Service (NOS; formerly U.S. Coast and Geodetic Survey) T-sheets, 2003 QuickBird satellite imagery, and a 2009 airborne lidar-derived Digital Elevation Model (DEM) (Gibbs and Richmond, 2015). The shoreline reference features digitized were the "approximate mean high-water line" as mapped on the 1947 T-sheets, the "mean high-water line" as mapped on the 1987 T-sheets, and the land-water interface interpreted from the Quickbird imagery and lidar DEM. Because the tide range is small in this region, the land-water interface is expected to be roughly representative of the approximate mean high-water line. Shoreline change rates were calculated every 50 m along both the open-ocean/barrier coast and the lagoon coast using the U.S. Geological Survey (USGS) developed Digital Shoreline Analysis System (D SAS) extension for ArcGIS (Thieler and others, 2009). A summary of the data sources, spatial extent, scale, resolution, and measurement uncertainties in terms of root-mean-square summations (after Hapke and others, 2006) are listed in table 1. Annualized shoreline position uncertainties are shown in table 2. Additional information on methodologies used for shoreline derivation and the associated measurement errors and uncertainties in the datasets can be found in Gibbs and others (2011) and Gibbs and Richmond (2015).

Table 2. Annualized uncertainty in shoreline position

[Annualized uncertainty is total uncertainty (table 1) divided by the total number of years between measurements, in meters per year]

	1987	2003	2009
1947	0.6	0.3	0.3
1987		1.3	0.9
2003			1.4

Model Simulation Methodology

The simulation strategy developed to determine the frequency and magnitude of coastal flooding, barrier island overwash, and morphodynamic change combines several numerical models (table 3). Time- and space-varying wind and atmospheric sea-level pressure fields, generated with regional model and reanalysis products and global climate models (GCMs), were obtained from outside sources and are discussed further in the next section.

Ten-meter-elevation winds were applied to two-dimensional surfaces of WaveWatchIII (WW3, Tolman, 1999) and SWAN (Booij and others, 1999) model grids. Both WW3 and SWAN models are third-generation, physics-based spectral wave averaging models; these models were used to simulate the generation and propagation of waves in the Beaufort Sea to the study site. The WW3 global grid (resolution 1°×1.25°, maximum northern latitude of 78°, ver. 3.14) was used to simulate hourly time-series of deepwater waves (Erikson and others, 2016). Waves generated with the WW3 global model were incorporated into the open boundaries (edges of the model domain) of the SWAN model to ensure that long-component

Table 1. Summary of shoreline data source information and average uncertainties.

[na, not applicable; NOAA, National Oceanic and Atmospheric Administration; USFWS, U.S. Fish and Wildlife Service; USGS, U.S. Geological Survey]

Parameter	T-sheets (1947)	T-sheets (1987)	QuickBird (2003)	Lidar (2009)
Source-ID	T08626 T08627	T01509	r1c10 r1c11 r2c11 r2c10 r2c11	na
Scale	1:20,000	1:50,000	1:12,000	na
Source	NOAA	NOAA	USFWS	USGS
Measurement Uncertainty (meters)				
Georeferencing	11	12	6	na
Digitizing	5	5	3	6
Survey	10	15	na	na
Total shoreline position	16	20	6	6

Table 3. Models employed and parameters simulated in this study.

Model	Parameter(s) simulated
WaveWatchIII	Waves in deep (>500-meter) water
SWAN (via Delft3D WAVE)	Waves; wind-wave generation and propagation of deepwater waves to the shore
Delft3D FLOW	Storm surge and other water-level fluctuations; currents; sediment transport
XBEACH	Wave propagation from 10-m water depth to land; water levels; wave run-up; morphodynamic change

waves generated from distant storms were included in the simulations. The SWAN model used three nested, curvilinear grids with a resolution ranging from 1 km at the continental shelf to less than 30 m in the area of Arey Island and Lagoon (fig. 7*A*). Bathymetry and elevation data collected for this study were used to populate the grids near the study site. Nearshore bathymetry was supplemented with NOAA soundings from the late 1940s (NOAA, 2010), and remaining areas were filled with data from a 1-km-resolution DEM (Danielson and others, 2008). The 1-km-resolution DEM is based on soundings from numerous sources, including Electronic Navigation Chart point soundings, research vessel underway soundings, multibeam swath mapping datasets, and digitized point soundings from paper nautical charts. Details on model settings are provided in appendix 2 of this document.

Storm surge, hydrodynamics, and long- and cross-shore sediment transport were simulated with the Deltares Delft3D (D3D) and XBEACH models (Deltares, 2010; Roelvink and others, 2009). Three D3D FLOW grids were used to generate storm surge (fig. 7*B*), whereas a single high-resolution grid (10-m spacing) was developed for the sediment transport simulations. The D3D model was run in a depth-averaged mode and dynamically coupled with the SWAN model to simulate surf zone longshore currents and cross-shore wave setup and calculate sediment transport. The D3D module was forced with the same wind-fields used in the SWAN simulations as well as space and time-varying sea-level pressure fields covering the entire domains. D3D grid bathymetry was developed from the same depth data sources as used for the SWAN model.

Morphodynamic changes to Arey Island were simulated with the cross-shore XBEACH model. XBEACH accounts for wave-group-generated surf and swash motions, as well as avalanching processes, making it particularly suited to model overwash and breaching. A total of 33 shore-normal profiles were extracted from the DEM. The transects extend from the

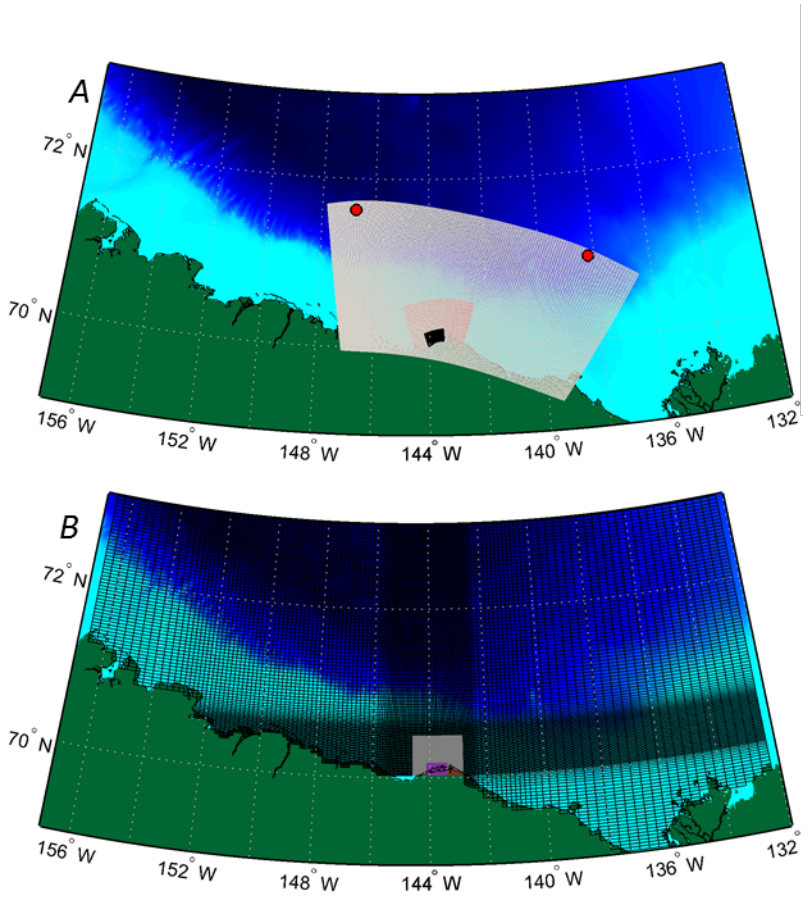

Figure 7. Maps of the eastern Arctic Alaska coast showing model grids used in the study. *A*, Three nested SWAN grids used to simulate wave growth and propagation across the continental shelf. Red circles indicate points at which WaveWatch3 model outputs were extracted and used as boundary conditions to the SWAN model. *B*, Three domain decomposition Delft3D-FLOW (D3D) grids used to simulate storm surge. Filled colors represent depths from 3,000 meters (blue) to exposed land surface (green). Bathymetry from Danielson and others (2008).

10-m isobath offshore of Arey Island, across the barrier island, and into the Lagoon; along-transect points were spaced at 20 m in the offshore and refined to 1 m in the shallow waters and across the island. Time-series of storm surge levels and wave heights, periods, and incident directions simulated with the SWAN and D3D models were extracted for individual storm events at the 10-m isobath and applied at the offshore end of each XBEACH transect. A single representative sediment grain size of 300 μm (medium sand; samples ranged in grain size from 200 μm to >2,000 μm; see appendixes) was assumed for all simulations. Sediment thickness was limited to 2 m based on a rough estimate of the barrier island active layer thickness as measured during field surveys in July 2011.

Meteorological Forcing and Sea-ice Data

Wind, sea-level pressure, and sea-ice extent from reanalysis products and GCMs were used to provide boundary conditions and force the wave and storm surge model simulations. The National Centers for Environmental Prediction (NCEP) / National Center for Atmospheric Research (NCAR) North Amercian Regional Reanalysis (NARR) (Mesinger and others, 2006) dataset provided spatial- and time-varying wind, sea-level pressure, and sea-ice extent for the years 1981 through 2010. NARR is an atmosphere and land surface hydrology dataset of the North American domain developed from a reanalysis of NCEP/NCAR's global models. The reanalysis is based on addition and assimilation of observational data from monitoring stations, radiosondes, satellites, aircraft reports, and other sources. The spatial and temporal resolutions of the NARR dataset are 32 km and 3 hours, respectively. Whereas other atmospheric reanalysis products, such as the Arctic System Reanalysis (https://rda.ucar.edu/datasets/ds631.0/) are now available, the total years of record are commonly too short to encompass a full climatological record (~30 years) and thus the NARR dataset was chosen for this study.

Sea-ice extent and atmospheric forcing for the period from 2010 to the end of the 21st century were obtained from four coupled GCMs (table 4). The models are considered coupled in the sense that they are atmosphere-ocean general circulation models coupled with land and sea-ice modules. GCM outputs used in this study were generated in support of the Coupled Model Inter-Comparison Project, phase 5 (CMIP5) (World Climate Research Programme, 2011; Taylor and others, 2012).

A benefit of using outputs from GCMs rather than relying on historical trends to assess future conditions is that the approach allows for climate evaluations in response to increasing greenhouse gases. Two scenarios were focused upon in this study: "stabilizing" and "business as usual" scenarios, termed RCP4.5 and RCP8.5, respectively (van Vuuren and others, 2011; Moss and others, 2010; Meehl and Hibbard, 2007). The CMIP5 scenarios differ slightly from past CMIP work, where climate scenarios were based on narrative storylines (van Vuuren and others 2011). The new scenarios are termed "representative concentration pathways" (RCPs) and are labeled according to the approximate target radiative forcing at about year 2100, relative to the pre-industrial period. RCP4.5 represents a concentration pathway that approximately results in a radiative forcing of 4.5 Watts per square meter (W/m^2) at year 2100 owing to mitigation of greenhouse gas emissions by mid-century; RCP8.5 results in a radiative forcing of 8.5 W/m^2 at year 2100 owing to continued growth in greenhouse gas emissions throughout the 21st century (Vuuren and others, 2011).

For the purpose of assessing projected storms, GCMs were selected based on the following criteria: (1) availability of near surface (10-m height) wind and sea-level pressure output, (2) frequency of synoptic (non-averaged) outputs, and (3) availability of projections to the year 2100. Near surface winds at 10-m height were required as inputs to the numerical wave and surge models. A high temporal resolution was preferred as it increases the probability of capturing extreme events which might be missed if the period between GCM outputs is too long. Our intent to extend the analysis to the year 2100 limited our choice of GCMs, as most of the CMIP5 model projections for scenarios RCP4.5 and RCP8.5 were only available for the middle and end periods of the 21st century (2026–2045

Table 4. Atmospheric forcing models used in this study.

Modeling center	Model name	Period covered	Model resolution
National Centers for Environmental Prediction, USA	NARR	1979*–2010	0.28°×0.28° ~31 km×~10 km**
Model for Interdisciplinary Research on Climate, Japan	MIROC5	2006–2100	1.4°×1.4° ~48 km×~156 km
Beijing Climate Center, Meteorological Administration, China	BCC-CSM1.1	2026–2045 and 2081–2100	2.8°×2.8° ~96 km×~311 km
Institute for Numerical Mathematics, Russia	INM-CM4	2026–2045 and 2081–2100	2.0°×1.5° ~52 km×~222 km
NOAA Geophysical Fluid Dynamics Laboratory, USA	GFDL-CM3	2026–2045 and 2081–2100	2.5°×1.5° ~52 km×~278 km

*Data from 1981 through 2010 were used in this study

**Approximate east-west and north-south distances at latitude 72° N.

and 2081–2100). An exception is the MIROC5 model, for which a complete time-series to the year 2100 was available for RCP4.5. Because MIROC5 includes a complete temporal dataset and a grid resolution finer (1.4°) than other GCMs, it was used as the source for wind and sea-level pressure projections in storm surge and nearshore wave modeling.

Wind Adjustments

Prior to applying atmospheric forcing to the numerical models, wind and sea-level pressure data from the NARR and MIROC5 models were compared to the 2006–2010 observational record at Barter Island Airport (lat. 70.133° N., long. 143.576° W., National Climatic Data Center [NCDC], 2013), located approximately 14 km east of the study site. Airport observations were available hourly and extracted for the months of July–November to approximate the open-water season. Winds measured at 0.6 m off the ground and reported relative to true north were converted to the standard 10-m height using wind-stress relationships developed by Large and Pond (1981) and rotated 26°10′ east (magnetic declination) to a geographic north reference frame. Because the anemometer was located adjacent to the open ocean, no adjustment for over-land measurements to over water measurements was necessary.

Data from the NARR and MIROC5 grid cells closest to the airport observation site were compared to observations in a probabilistic manner (fig. 8). A time-series comparison is only valid for the NARR reanalysis dataset; it is not expected that timing of events will be simulated accurately with a global model such as MIROC5, but rather it is the overall seasonal and multi-year timing of events as well as frequency that are of relevance with the GCMs. Comparison of cumulative probabilities in figure 8 shows that winds near land from both the NARR and MIROC5 datasets underestimate observations. A model reference level of 0.2 m above ground was assumed and used to convert the model wind data to the 10-m neutral level (Large and Pond, 1981), significantly improving comparison to observations (fig. 8). A similar approach was used by Graham and others (2012) for adjusting GCM winds in preparation for wave simulations in the Pacific Ocean. Wind adjustments were made to all windspeeds used in the storm surge and nearshore (SWAN) wave models. No adjustments were made to wind directions.

Sea-level Rise

Information about relative sea-level rise along the North Slope of Alaska is limited by the short observational water-level records and poorly known rates of vertical land movement. The longest water-level record available along the Alaskan Arctic coast is at Prudhoe Bay from 1990 to the present (NOAA, 2016). The Prudhoe Bay station is located about 170 km west of Arey Lagoon. Analysis of monthly mean water levels at Prudhoe Bay, including the removal of seasonal variations, showed a sea-level increase of 2.3±2.6 millimeters per year (mm/yr), with no statistical significance (Sultan and

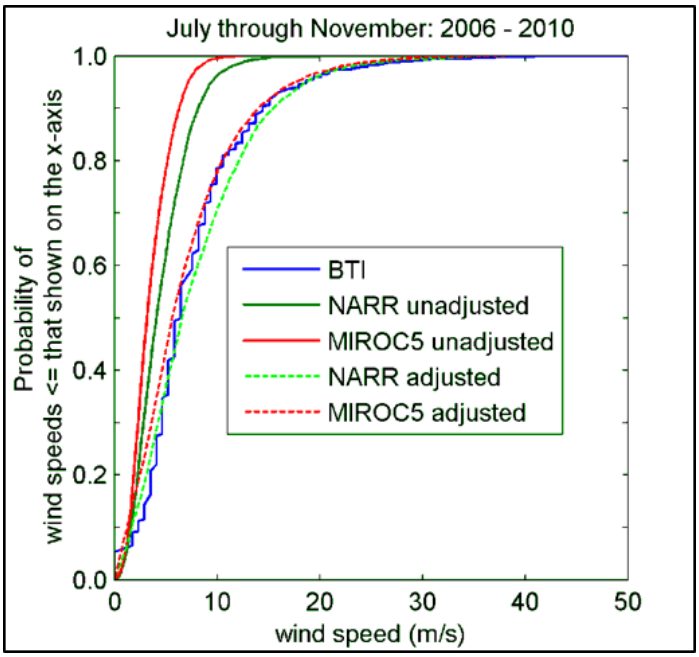

Figure 8. Plot comparing measured and model-hindcasted winds at the Barter Island, Alaska, landing strip (BTI) (lat 70.134° N, long 143.577° W). Data are plotted as cumulative probabilities of all measured and modeled windspeeds from July through November, 2006 through 2010, the period of coincident measurements and available hindcast data.

others, 2011). The only other tide gauge on the Beaufort Sea coast with measurements spanning more than 1 year is the Tuktoyaktuk water-level gauge located in the Northwest Territories of Canada, approximately 390 km east of the study site. Based on measurements from 1962 through 1997, Manson and Solomon (2007) found a statistically significant sea-level rise of 3.5±1.1 mm/yr.

A study using late Holocene diatom biostratigraphy (Campeau and others, 2000) concluded that rates of sea-level rise ranged from approximately 1.1 to 2.5 mm/yr from 3,000 years before present to the late 1900s. Although Intergovernmental Panel on Climate Change (IPCC) model projections of sea-level rise vary greatly, the largest increases are projected to occur in the Arctic as suggested by seven of nine CMIP3 global models which predicted an increase of 0.30 to 0.40 m by the year 2100 (IPCC, 2007) along Alaska's Arctic coast. Yin (2012) analyzed long-term sea level projections for Arctic Alaska from 34 different CMIP5 GCMs under three greenhouse gas emissions scenarios and calculated an increase of 0.25 to 0.35 m by the year 2100 for the midrange scenario RCP4.5 considered in this study. The higher radiative forcing scenario, RCP8.5, was projected to increase sea level by 0.35 to 0.40 m by 2100 in the vicinity of eastern Arctic Alaska. Contributions from land-ice melt and the related global halosteric (that is, the volume increase caused by freshening of the water column) sea-level rise were not considered in the GCM runs, nor were local factors such as vertical land motion or change in mean sea level resulting from land ice melt (Milne and others, 2009). In consideration of the spread in estimated sea-level rise rates (fig. 9) and the relative proximity of each of the Prudhoe Bay and Tuktoyaktuk tide gauges, an upper value of a constant 3.5 mm/yr (0.315 m by 2100) was assumed for all model simulations.

Field Observations and Model Evaluation

Waves, currents, and water levels were measured between July 12 and September 26, 2011, at two sites: approximately 500 m offshore of Arey Island (5-m water depth) and within the lagoon (~1-m depth). The measurements were used to assess background conditions and were compared with model simulations. The highest waves measured offshore of Arey Island were predominantly from the northwest to north with a peak wave period in the range of 4 to 8 s. The maximum wave height measured was 0.98 m (peak wave period of 7.7 s). Wave heights within the lagoon were negligible and bottom currents averaged more than 82 days (July 12 to September 26/27, 2011) during the open-water season were nearly twice as high offshore of Arey Island (0.69 m/s) compared to inside the lagoon (0.38 m/s; fig. 7). The principal current direction was to the southwest and south-southwest at the offshore and lagoon sites, respectively. Water levels at the offshore site and within Arey Lagoon were nearly identical throughout the observation period and, following removal of the tidal signal, only reached a maximum of 0.28 m above MSL in early September 2011.

Observations of measured wave heights and water levels are compared to model simulations as cumulative probability plots in figure 10. Considering the rather low measured energy environment (significant wave height <1 m and water level <0.30 m), comparisons are quite good. In particular, the higher events which are of importance to this study were captured well with a modeled maximum significant wave height of 0.93 m (compared to measured 0.98 m) and modeled maximum water level of 0.36 m (compared to measured 0.28 m).

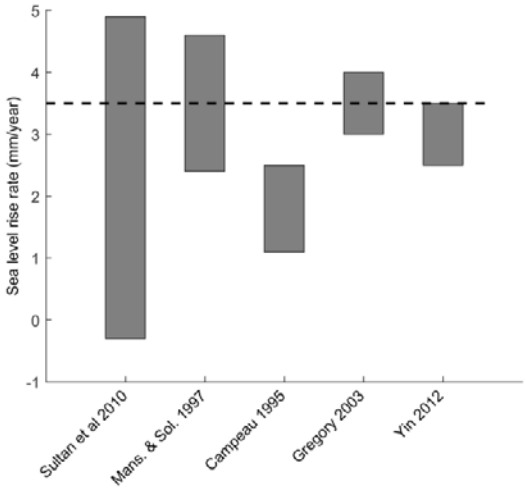

Figure 9. Bar chart showing published ranges of sea level rise rates in the Beaufort Sea, Alaska, and western Canada. Dashed horizontal line at 3.5 millimeters per year (mm/yr) (3.5 centimeters per decade) depicts the constant sea-level rise rate used in this study.

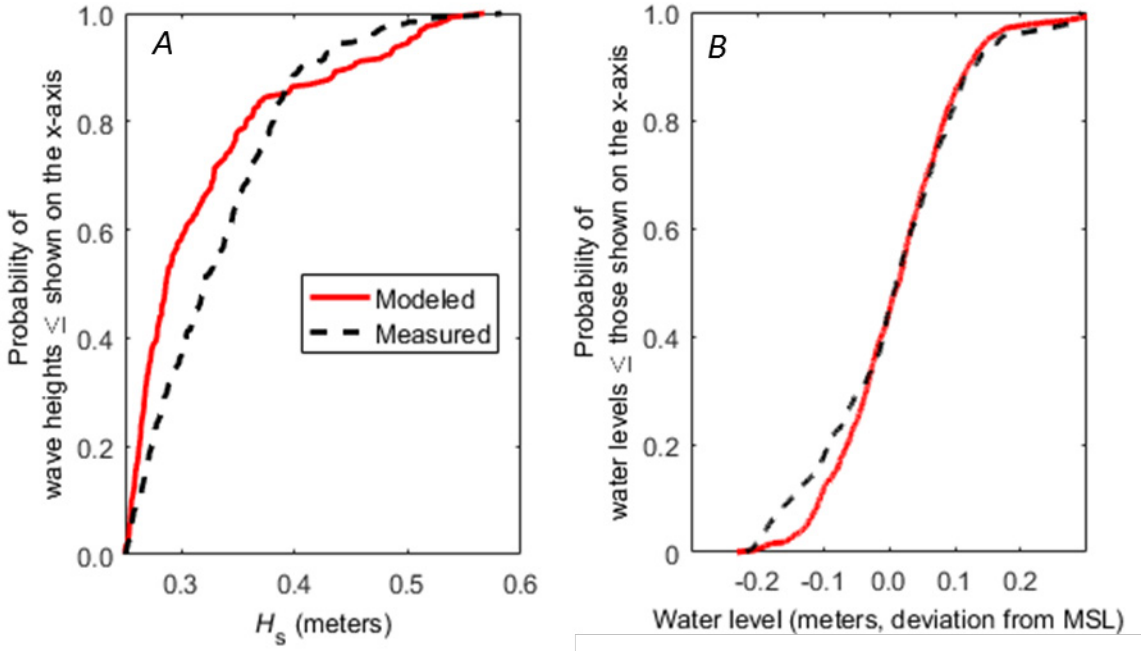

Figure 10. Cumulative probability plots comparing modeled and measured wave heights (H_s) and water levels at the nearshore observation site located in 5-meter water depth seaward of Arey Island, Alaska. MSL, mean sea level. Dashed lines in *A* show the upper and lower 95-percent confidence bounds.

Results

Historical Shoreline Change

Arey Island Breaching History

A time-series of historical images that were not included in the shoreline change analysis because of inconsistencies in scale and quality of imagery provide a qualitative record of the dynamic history of Arey Island through the years (fig. 11). The imagery shows that Arey Island-west remained fairly stable through time whereas the eastern section experienced landward migration and several breaching events. The imagery shows a single breaching of the western section between 1947 and 1955, compared to multiple breachings of the eastern section in the periods 1979–1985 and 1992–1994 and in 1999. Amid these breaching events, island sections reformed and nearly reattached. An exception to this was following the breach(es) in 1999 when, over a 5-year period through 2004, the opening continued to widen to at least 1,500 m and the easternmost section of the island chain detached from the spit connected to Barter Island. After 2004, and up through 2011, deposition resulted in a near-continuous barrier island with a narrow opening near the midsection of the eastern part that in 2011 was nearly inaccessible by small vessels. Although these images are useful for estimating the timing and location of breach events, a more quantitative estimate of the overall stability of Arey Island is desired. To this end, four historical shorelines were digitized and shoreline change rates computed; results of these are presented below.

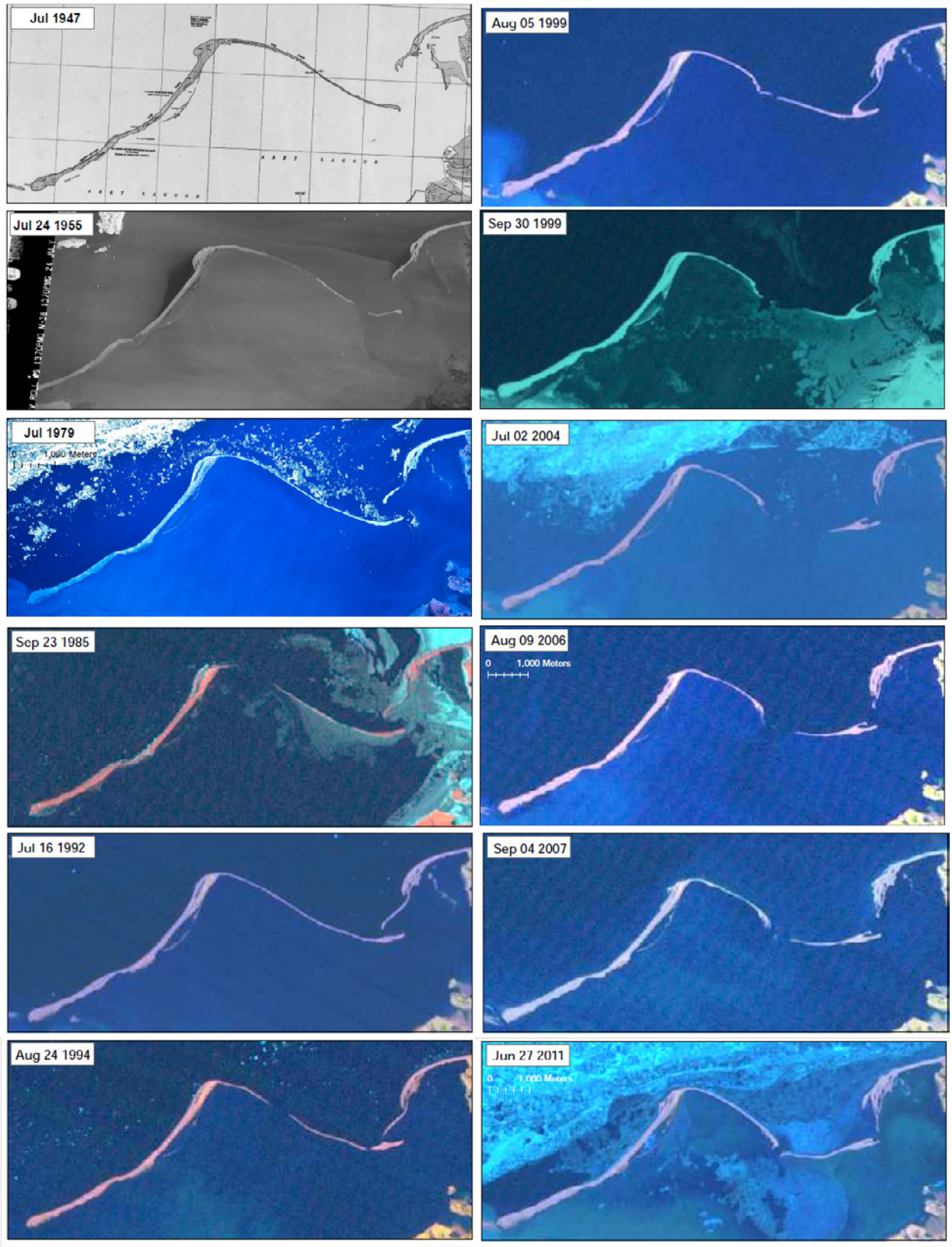

Figure 11. A series of 12 images that highlight the morphodynamic history of Arey Island, Alaska. 1947, NOS T-sheet; 1955, aerial photography; 1979–2011, LANDSAT satellite imagery.

Arey Island Shoreline Change Rates

The average long-term (1947–2009) rate of change along the exposed, open-ocean coast of Arey Island is −3.8±0.3 meters per year (m/yr) (range = −14.4 to 2.5 m/yr) (table 5); however, as alluded to previously, the eastern and western parts of the island experienced considerably different patterns of shoreline change throughout the study period (figs. 12 and 13). The western part of the island remained mostly stable to slightly accretional, whereas the northwest-southeast trending eastern section migrated southwest (landward) and segmented into multiple islands.

T-sheets show Arey Island as one continuous island, nearly 11 km long, in 1947 (figs. 11 and 12). By 1987, the relatively lower and narrower eastern part of the island migrated 410 m southwest (figs. 12 and 13), and by 2009, sections migrated as much as 900 m farther landward.

In contrast, the western part of the island remained relatively stable between 1947 and 2009, averaging −0.1±0.3 m/yr (table 5). An approximately 1.5-km-long erosional segment is present between kilometers 8 and 9.5 on fig. 13, with a maximum landward excursion of about 250 m and apparent westward migration between 1947 and 2009 (fig. 12). Both east and west of this erosional section the long-term change is slightly accretional (less than 100 m).

Average rates of change and ranges for the different island sections and periods are shown in table 5. An increase in erosion rates during the 1987–2009 period compared to the 1947–2009 or 1947–1987 periods was weakly significant for the eastern section of Arey Island. Shoreline change rates did not vary significantly for Arey Island-west.

Arey Lagoon Shoreline Change Rates

The long-term (1947–2009) rate of change along the Arey Lagoon coast is slightly erosional (average -0.7±0.3 m/yr) (table 5; figs. 12 and 14). Rates are relatively uniform along the entire coast, except for three areas of relatively higher erosion

Table 5. Summary of Arey Island and Lagoon, Alaska, shoreline change rates.

[Uncertainty in shoreline position for each analysis period is included (±). Ranges of rates are in parentheses. m/yr, meter per year]

Location	Average change rate (range of change rate), in m/yr		
	1947–2009 (±0.3 m/yr)	1947–1987 (±0.6 m/yr)	1987–2009 (±0.9 m/yr)
Arey Island	−3.8 (−14.4 to 2.5)	−3.2 (−10.2 to 2.9)	–5.2 (−25.5 to 7.0)
Arey Island-West	−0.1 (−4.4 to 2.5)	−0.4 (−3.6 to 2.9)	0.4 (−7.1 to 7.0)
Arey Island-East	−7.7 (−14.4 to 1.0)	−6.0 (−10.2 to 1.4)	–11.3 (−25.5 to 4.3)
Arey Lagoon	−0.7 (−4.3 to 0.4)	−0.7 (−4.7 to 1.0)	–0.8 (−7.9 to 5.5)

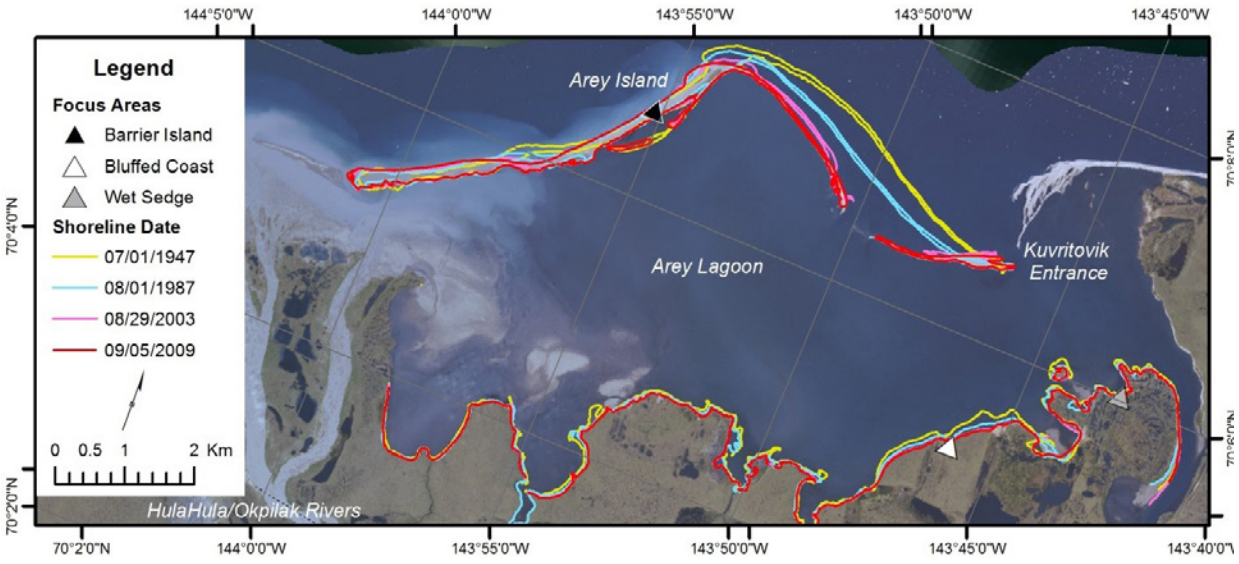

Figure 12. Map of Arey Island and Lagoon, Alaska, showing four historical shorelines. Base imagery from University of Alaska's Geographic Information Network of Alaska (http://www.gina.alaska.edu). km, kilometers.

rates at kilometers 6–9, kilometers 13–14, and kilometers 16–17 on fig. 10. The relative stability observed along the lagoon coast through time is likely due to the protection from incident wave energy provided by Arey Island. The higher erosion rates measured between kilometers 6 and 9 may be associated with the breach in eastern Arey Island, which would have reduced the protection from incident wave energy and increased the potential for higher waves to impact that section of coast. No significant variation in shoreline change rates through time were observed for the Arey Lagoon coast (table 5).

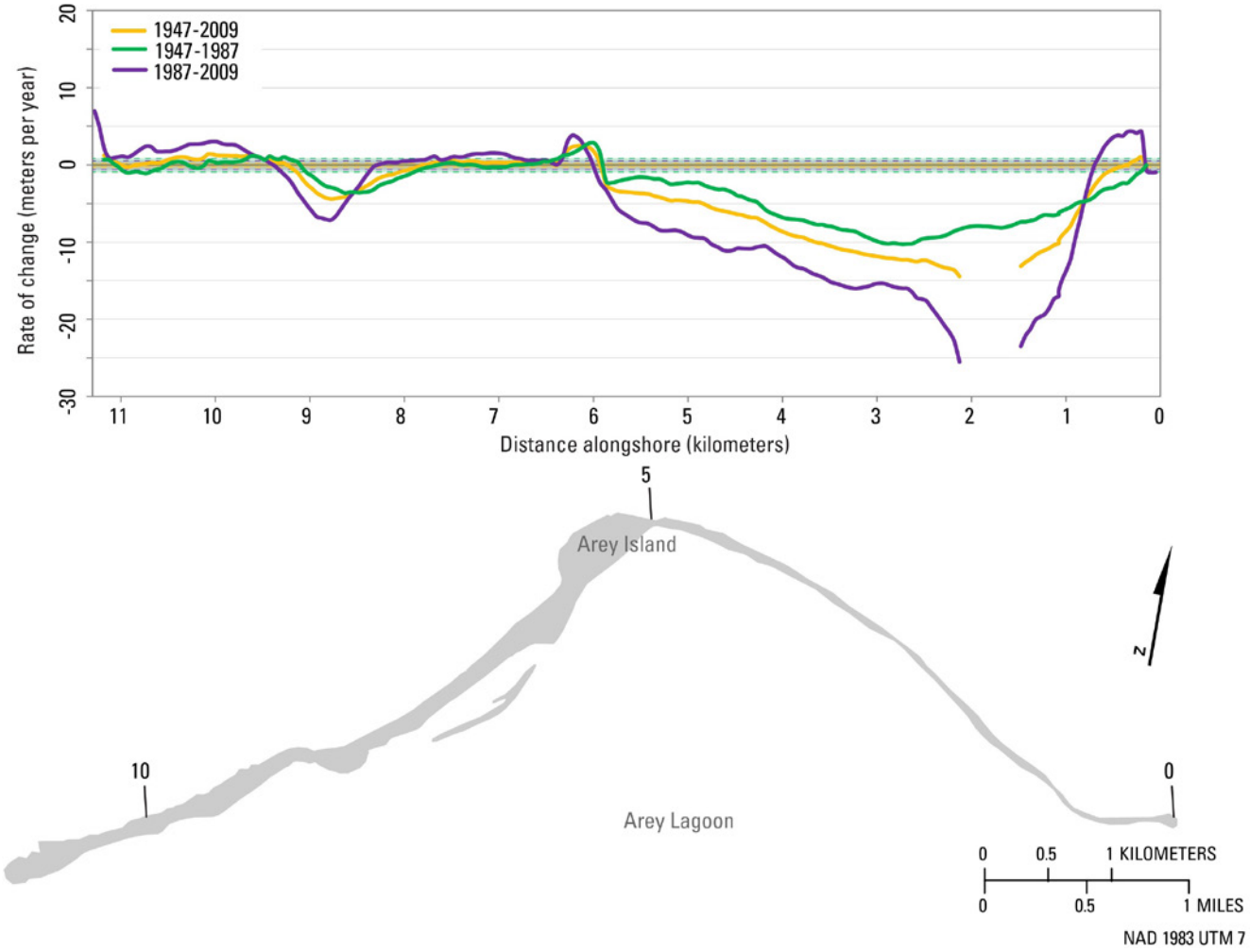

Figure 13. Graph and map showing shoreline change rates of Arey Island, Alaska, for the 1947–1987 and 1987–2009 periods and the entire 1947–2009 period. Colored bars and dashed lines indicate the annualized uncertainty in shoreline position for each period (from table 2). Breaks in solid lines represent breaches. The western part of the island has shown relative stability or accretion through time compared to very high erosion rates measured on the eastern part of Arey Island.

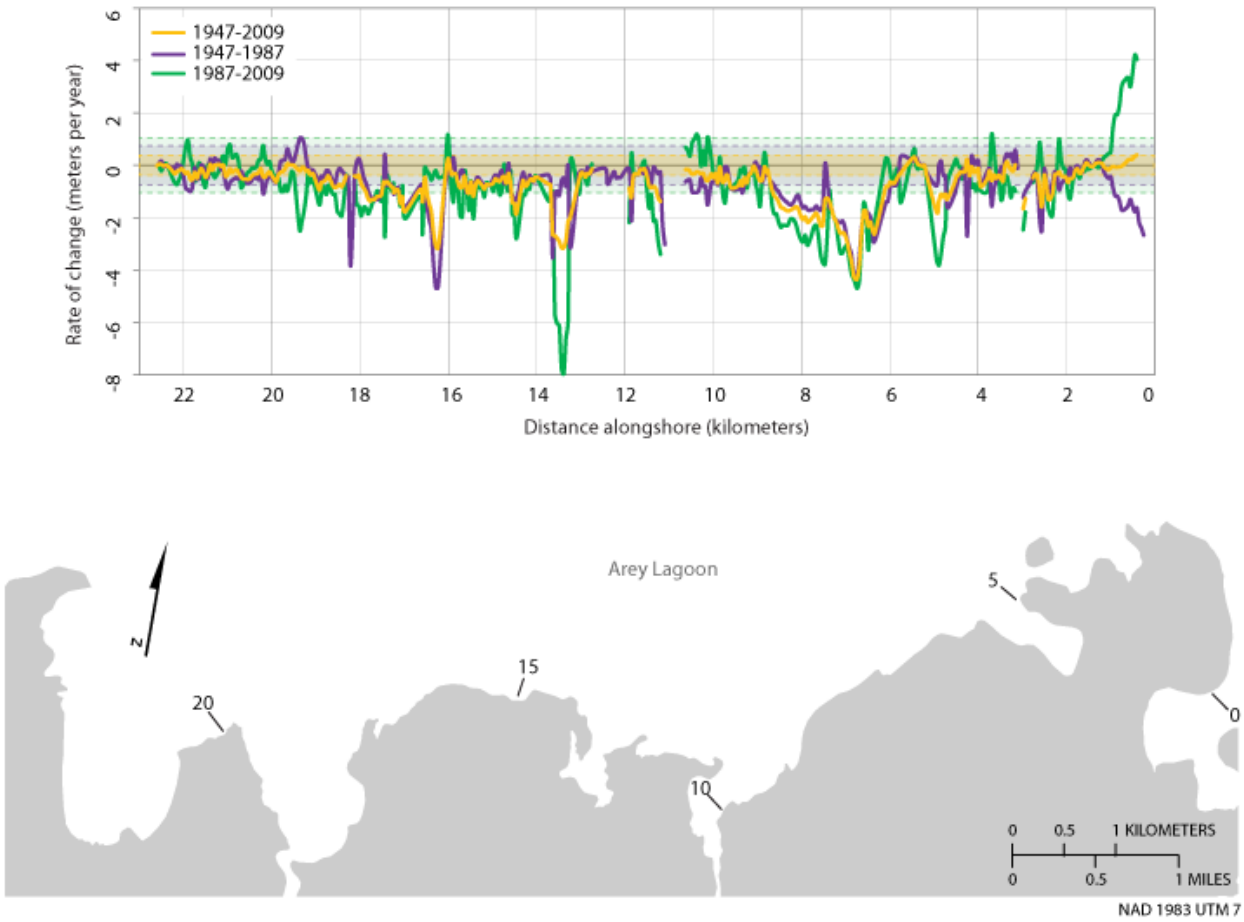

Figure 14. Graph and map showing shoreline change rates of the Arey Lagoon, Alaska, mainland coast for the 1947–1987 and 1987–2009 periods and the entire 1947–2009 period. Colored bars and dashed lines indicate the annualized uncertainty in shoreline position for each period (from table 2). Distance along shoreline is labeled in 5 km increments from east to west. Shoreline change rates along the protected lagoon coast are much lower compared to the open coast.

Hindcast and Projected Storms

The first and last days of the open-water season in the vicinity of Arey Lagoon were determined from weekly satellite data for the years 1981 through 2013 and from GCM RCP4.5 projections for the remainder of the 21st century (fig. 15). NARR reanalysis indicates that as recently as 2010–2013, the seasonal ice pack moves out and returns approximately 37 days earlier and later in the season compared to the early 1980s. Duration of the open-water season has more than doubled from ~50 days in the early 1980s to approximately 120 days in the 2010s. These values are comparable to those reported by Overeem and others (2011) for Drew Point, located approximately 390 km west of the study site on the Beaufort Sea coast. In that study, the open-water season more than doubled over approximately the same period (1979–2011).

Projected rates of change in pack-ice retreat and refreeze suggest that open-water durations will continue to increase but at a slower pace compared to the historical period (fitted line segments from 2012–2100, fig. 15). Inclusion of all the GCM models indicates that the onset and end of the open-water season will shift earlier and later by 20 days per decade and 40 days per decade, respectively, and that the end of the open-water season will extend well into November by the year 2100.

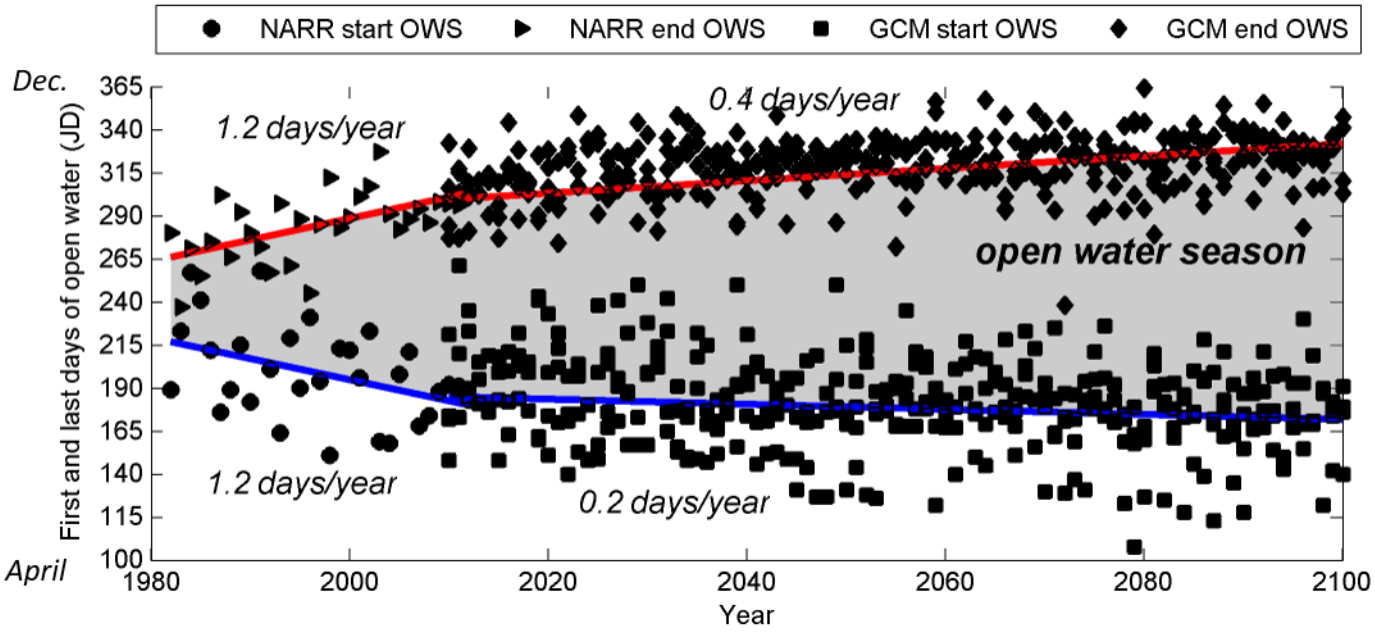

Figure 15. Plot showing the first and last day of the open-water season (OWS) near Arey Island, Alaska. Units are in Julian Days (JD). Blue and red lines are least-square best fits to the onset and end of the open-water season, respectively. Hindcast trends are derived from North American Regional Reanalysis (NARR) and projected trends are derived from all four global climate models (GCMs) listed in table 3.

Waves

Deepwater Wave Conditions

Deepwater significant wave heights computed with the WW3 model and forced by reanalysis and GCM projected winds for the open-water season from 1981 through 2100 show increasing extreme significant wave heights through time (fig. 16; table 6) that appear to be related to both increases in storm duration and wind magnitude. The mean of the five highest wave events over a 5-year period, along with the maximum and minimum during each 5-year bin, are plotted for the hindcast mid- and high-radiative forcing scenarios RCP4.5 and RCP8.5 in figures 16*A* and 16*B*, respectively. For the projected period from 2011 to 2100, results from four separate GCMs and both emission scenarios are shown. Note, however, that a complete time-series was only available for the MIROC5 RCP4.5 case at the time of this study. The MIROC5 projections typically fall within the midrange of the other GCMs, sug-gesting that the MIROC5 model provides reasonable estimates for periods when other models are not available.

Least-squares linear fits of averaged 5-year max significant wave heights were found to be statistically significant (p-value<0.05) for both the entire time-series (1981–2100) and the combined period of the hindcast and first half of the 21st century (1981–2050). Linear trends of the entire time series suggest an overall increase in significant wave heights of 0.14 and 0.18 m/decade for the RCP4.5 and RCP8.5 scenarios. When considering the hindcast and first half of the 21st century through 2045, rates of change are more than twice as great, at 0.35 and 0.49 m/decade for the RCP4.5 and RCP8.5 scenarios, respectively.

Peak wave periods are also projected to increase (fig. 17; table 6). Similar to significant wave heights, statistically significant increases in wave periods were obtained for the full time-series and combined hindcast and first half of the century periods under both climate scenarios. When considering the entire time-series, historical peak wave periods are projected to increase by approximately 0.1 s/decade for both climate scenarios; for the combined years of hindcast and first half of the century, the rates are greater at 0.4 and 0.3 s/decade for the RCP4.5 and RCP8.5 scenarios, respectively. Mean peak periods associated with extreme wave heights are anticipated to be on the order of 11.5 s with a maximum of 13 to 14 s, whereas the maximum hindcast peak wave period was 11 s. An increase in wave period has implications for wave run-up at the shore.

Peak wave directions are primarily from the northeast and less frequently from the northwest for both the hindcast and projected periods (fig. 18). Model hindcasts indicate that the

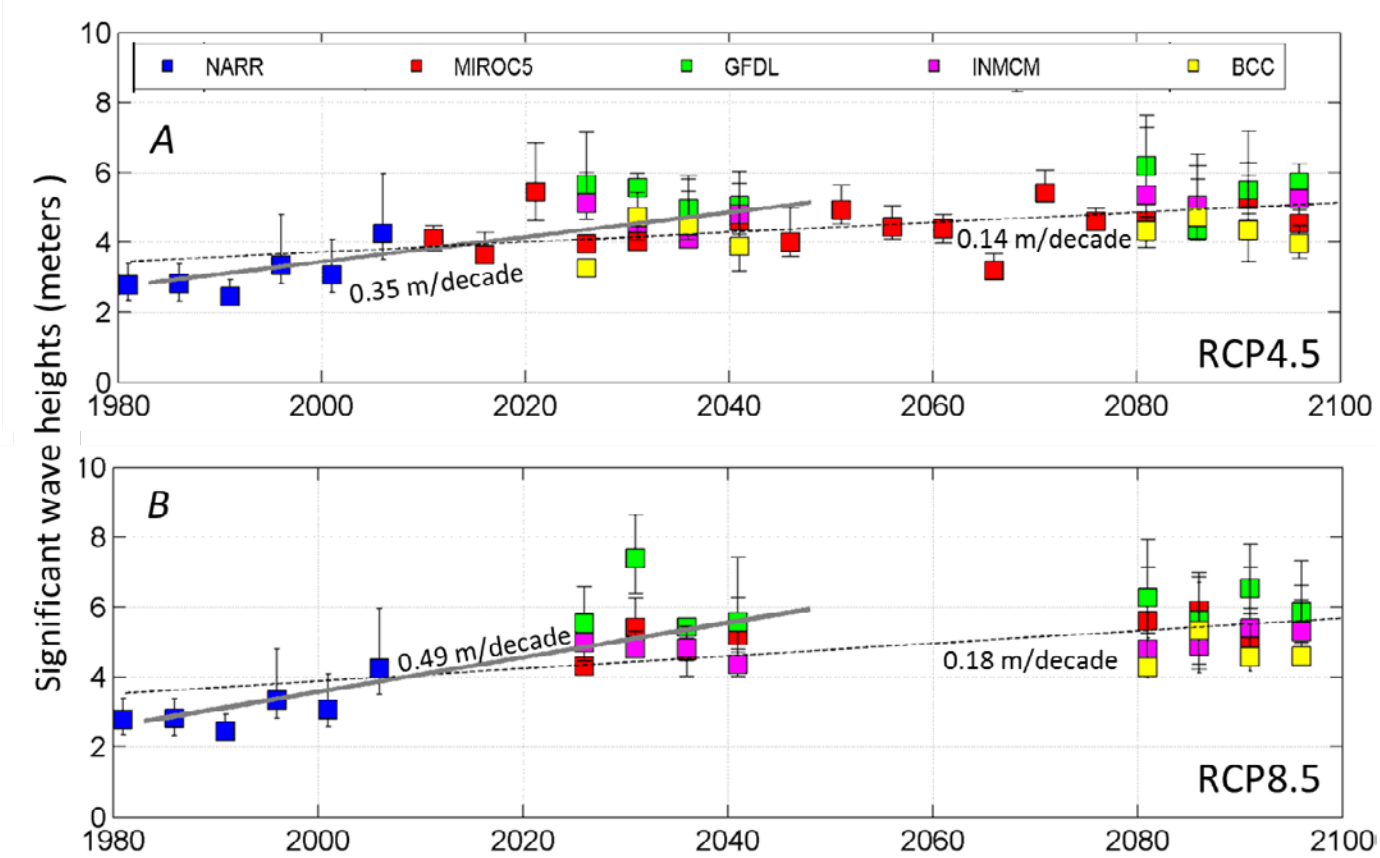

Figure 16. Plots showing extreme deepwater significant wave heights computed with the WaveWatch3 model for the open-water season of the hindcast (1981–2010) and projected (2011–2100) periods at the easternmost red circle in figure 7*A*. *A,* Projected significant wave heights for the midrange mitigation climate scenario RCP4.5. *B,* Projected significant wave heights for the high radiative forcing climate scenario RCP8.5. NARR, MIROC5, GFDL, INMCM, and BCC are acronyms for the model wind fields used in the simulations and are listed in table 3. Boxes represent the mean of the five highest wave events over a 5-year period and vertical bars represent the maximum and minimum of those top five events. Linear fits through 5-year-averaged extreme values are statistically significant at the *p*-value<0.05 level; solid lines are for the hindcast and first half of the 21st century (1981–2049); dashed lines are for the entire time-series.

Table 6. Least-square linear fits through time-series of model-simulated significant wave heights and associated peak wave periods at the easternmost deepwater location shown in figure 7*A*.

[r^2, coefficient of determination; m, meter; s, second]

Scenario	Period	Slope*	r^2
Significant wave height			
RCP4.5	1981–2049	0.35	0.53
RCP8.5	1981–2049	0.49	0.65
RCP4.5	1981–2100	0.14	0.32
RCP8.5	1981–2100	0.18	0.39
Peak wave period			
RCP4.5	1981–2049	0.4	0.68
RCP8.5	1981–2049	0.3	0.42
RCP4.5	1981–2100	0.1	0.35

*meters per decade and seconds per decade for significant wave heights and peak wave periods, respectively.

1980s and early 1990s were relatively quiescent with a storm count of less than two per year and from either the northeast or northwest (fig. 18*B*). This can, at least in part, be attributed to the shorter open-water season. A plot of storm counts versus length of the open-water season indicates an increase of about 0.5 storms per day of increased open-water season (fig. 18*D*, coefficient of determination, $r^2 = 0.60$ linear; $r^2 = 0.62$ exponential fit). Most (>98 percent) of these storms occur later in the open-water season (August or later).

During the latter half of the 1990s, northeast storm occurrence exceeded six per year on average (>30 for the 5-year period). For the remaining time-series through 2100, storm counts from the northeast vary between 2 and nearly 10 events per year. Storm counts from the northwest increase toward the mid-21st century and follow with fewer counts in the early 2050s to late 2060s. The greatest number of events with significant wave heights greater than 4 m and from the northwest is projected to occur during the latter half of the 2070s (light blue shading in fig. 18*B*, $N = 5$).

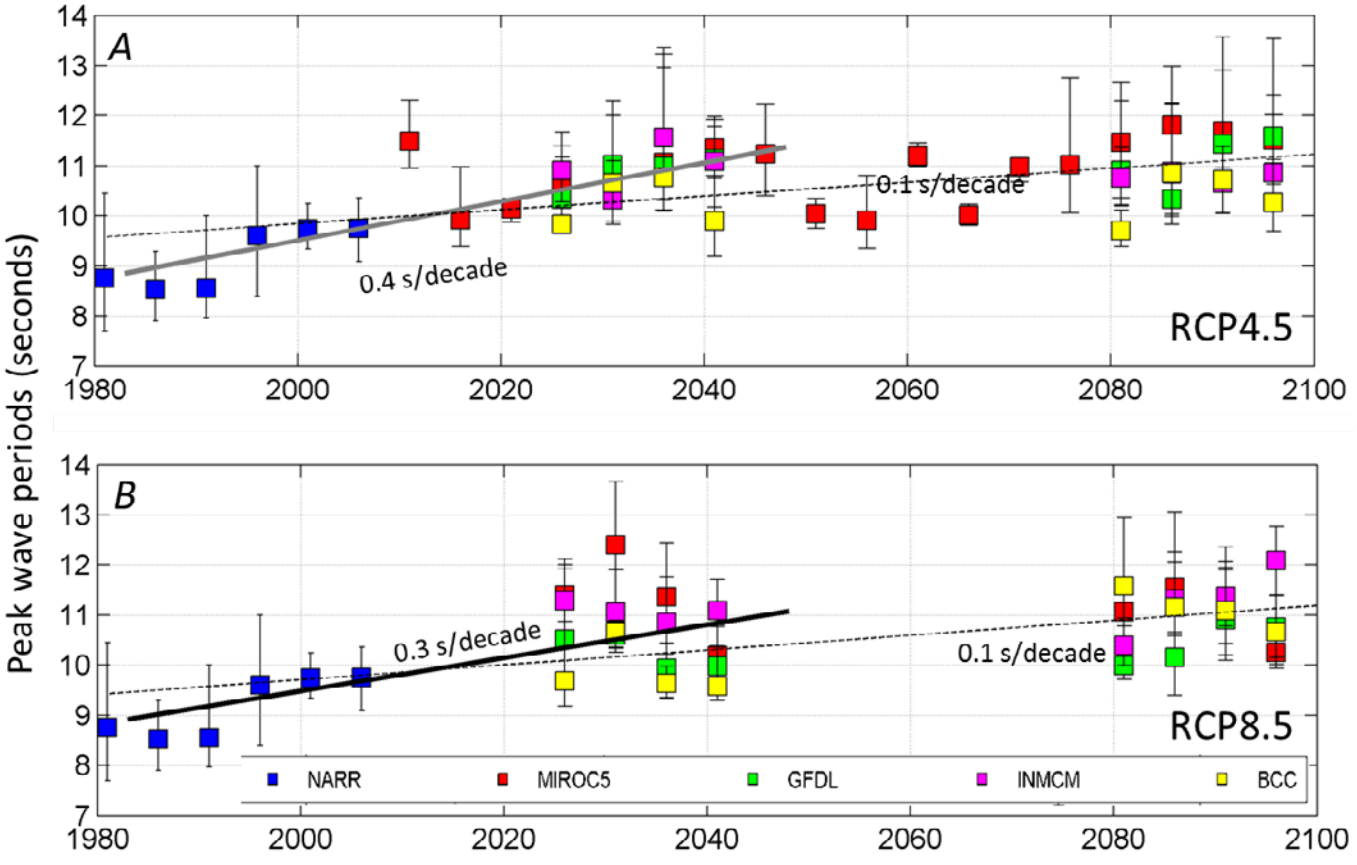

Figure 17. Plots showing extreme deepwater peak wave periods associated with the maximum wave heights in figure 12 for the open-water season of the hindcast (1981–2010) and projected (2011–2100) periods. Data are from the easternmost red circle in figure 7*A* computed with the WW3 model for the open-water season. *A*, Projected peak wave periods for the midrange mitigation climate scenario RCP4.5. *B*, Projected peak wave periods for the high radiative forcing climate scenario RCP8.5. NARR, MIROC5, GFDL, INMCM, and BCC are acronyms for the model wind fields used in the simulations and are listed in table 3. Boxes represent the mean wave period of the five highest wave events over a 5-year period and vertical bars represent the maximum and minimum of those top five events. Linear fits through 5-year-averaged extreme values are statistically significant at the *p*-value<0.05 level; solid lines are for the hindcast and first half of the 21st century (1981–2049); dashed lines are for the entire time-series.

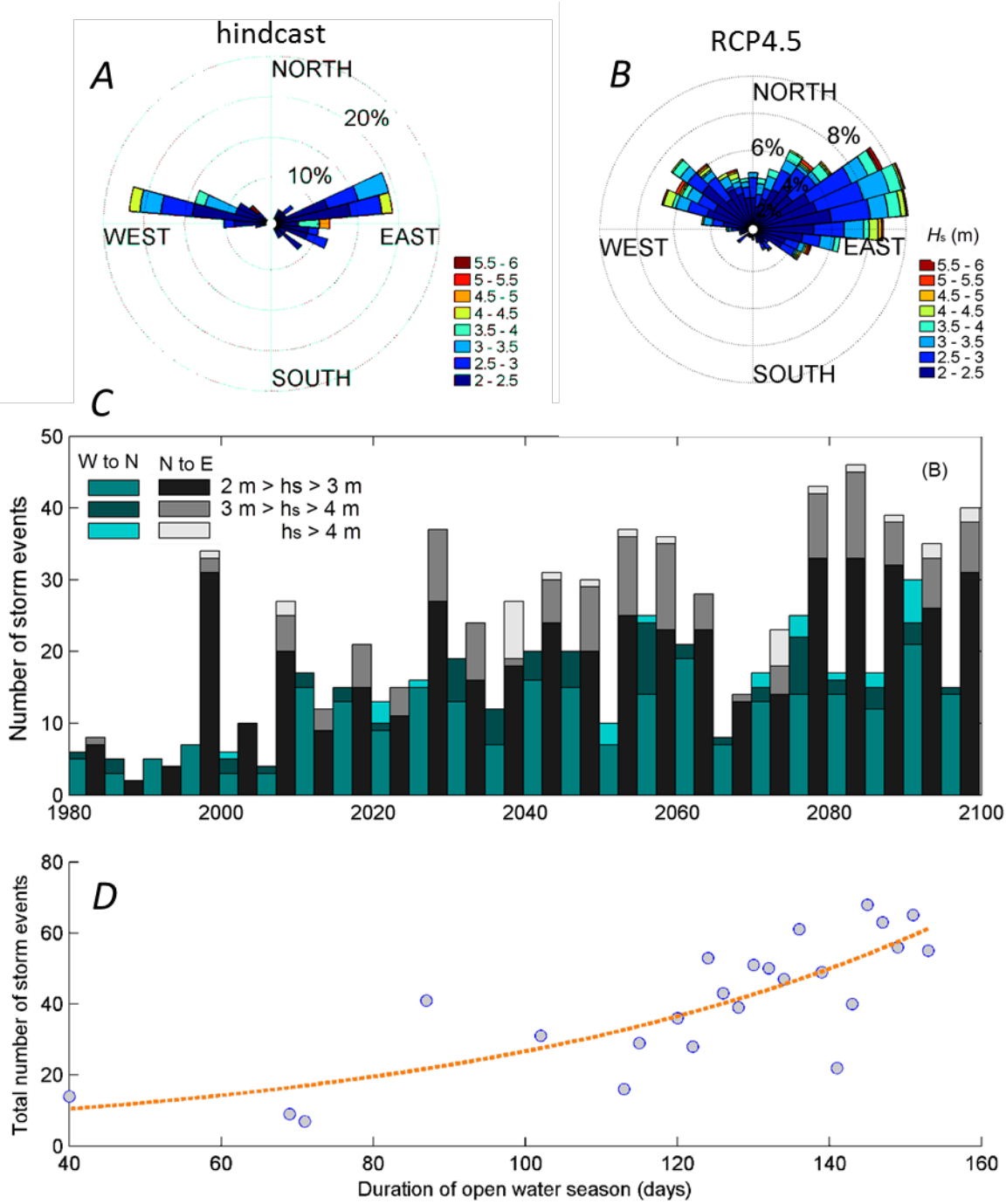

Figure 18. Frequency plots of deepwater waves greater than or equal to 2 meters. Data are from the easternmost red circle in figure 7*A* computed with the WW3 model for the open-water season. *A* and *B*, Wave roses showing the incident wave directions for the hindcast and projected RCP4.5 climate scenario. The wave roses illustrate the dominant northeast incident direction and less frequent but still dominant northwest incident direction. *C*, Time-series plot showing the number of storm events per 5-year period from the northwest and northeast with respect to time. *D,* Total number of storms compared to the duration of the open-water season. %, percent; H_S, significant wave height; m, meter.

Nearshore Waves at the 10-m Isobath

To account for wave energy loss across the continental shelf as well as local wave growth, storm waves simulated with the WW3 model were propagated to the shore and combined with locally wind-generated wave energy. This was accomplished with the SWAN model: deepwater storm waves from the WW3 model were applied at the offshore open boundaries of the SWAN grid and time-varying winds were applied across the entire SWAN domain. Storms were defined as events with peak significant wave height greater than or equal to 2 m, with the selected threshold based on World Maritime Organization sea state code for moderate seas. Because westerly storms produce elevated water levels (storm surges) whereas northeasterly storms generate a water-level set-down (see "Clarification of Terms" section), only storms from the west were simulated for detailed calculation of significant wave height along the 10-m isobaths immediately seaward of Arey Island.

Contrary to the deepwater WW3 simulation results, there is no apparent trend in the 10-m isobath time-series of significant wave height or peak wave period. This is likely a result of the broad continental shelf, enabling dissipation of wave energy as the waves propagate across the shelf and limit wave growth owing to shallow water depths. Although there is no apparent overall trend, maximum significant wave height is projected to exceed any previous events by 0.4 m around year 2022. Similar to deepwater conditions, peak wave period is expected to be higher and reach 12 s (fig. 16*B*).

Although there is no temporal trend in significant wave height or peak wave period, a near sinusoidal pattern is evident highlighting non-seasonal atmospheric patterns that play a role in the simulated wave climate (fig. 19). Previous work showed the dependence of hindcast Arctic waves to the Northern Annual Mode, a hemispheric-scale pattern of climate variability (Erikson and others, 2011).

To illustrate the pattern in figure 19*A*, starting with the NARR data in the early 1980s, significant wave height decreases and subsequently increases toward the end of the hindcast period up through 2010. Continuing along the MIROC5 timeline (red squares, fig. 19*A*), extreme significant wave height values peak in 2021–2025 and 2081–2085. This multi-decadal pattern is also evident in the storm surge results (next section) and deepwater wave simulations (fig. 17), albeit more difficult to discern.

Storm Surge Levels

Numerical model experiments were conducted to quantify storm surge levels near Arey Lagoon in response to constant winds from all possible directions in combination with varying sea-ice extents. Winds ranging in speed from 4 to 44 m/s at 10° direction bins were allowed to "blow" over the model domains for one day each. Steady state conditions (no further changes in water levels) were reached in approximately 12 hours for nearly all the runs.

Polar plots (fig. 20) illustrate the dependence of water levels on wind direction and magnitude and show that winds blowing from ~210° to 30° from true north cause the greatest increase in water levels at the shore. They also show that, because of the northwest facing orientation of the coastline, the wind-induced setup is larger than the lowering of the water level from equivalent wind magnitudes blowing from the opposite direction.

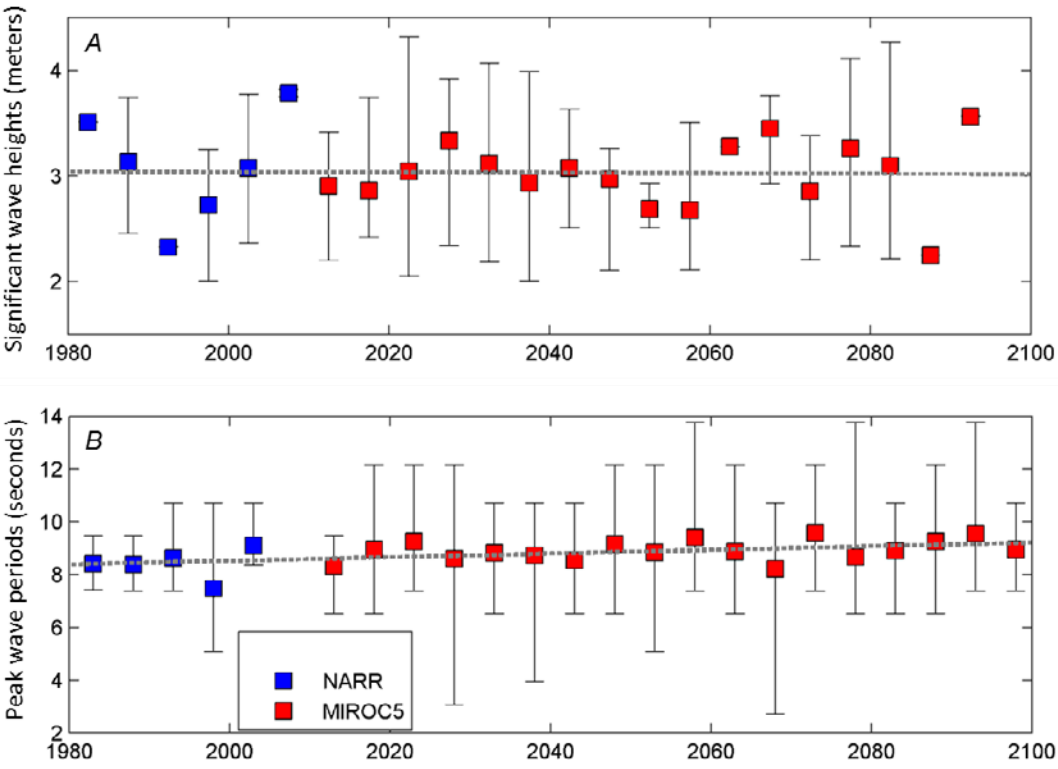

Figure 19. Time-series plots of modeled northwest incident waves at the 10-meter isobath offshore of Arey Island-east, Alaska. *A*, Significant wave heights. *B*, peak wave periods. Results were computed with the WaveWatch3 and SWAN models for the hindcast (blue) and projected (red) periods. NARR and MIROC5 are acronyms for the model wind fields used in the simulations and are listed in table 3. Only wave events that resulted in significant wave heights greater than 2 m at the 10-m isobath with incidence angle from the northwest were included in the plot. Boxes represent the mean of the five highest wave events over a 5-year period and vertical bars represent the maximum and minimum of those top five events. Dashed lines are least-square linear regressions, neither of which is statistically significant.

The sensitivity of wind-generated storm-surge levels to the presence of sea ice was tested by running the model under conditions of no sea ice compared to the presence of July, August, and October monthly 1979–2012 median extents (fig. 20*A*). The extreme event of 44 m/s sustained winds from the northwest (330°) resulted in a maximum water level of 2.25 m using the July median sea-ice extent and 3.05 m for all other simulations with the median August, September, October, and no sea-ice conditions. Because most storms typically occur during the latter part of the summer season and early fall (August and later) when the pack ice is far from shore, all subsequent storm simulations were done without regard to the position of the pack ice. This assumption of a seasonally ice-free Arctic is substantiated by a large number of CMIP5 models (Wang and Overland, 2015; Kay and others, 2011; Stroeve and others, 2012). Stroeve and others (2012) compiled sea-ice extent data from 56 RCP4.5 CMIP5 runs and concluded that nearly one-third of the realizations projected seasonal (not entire year) ice-free conditions by 2100, and possibly as early as 2020.

For more realistic representations, storm-surge levels were simulated using temporally and spatially varying hindcast and projected wind and pressure fields obtained from the NARR and MIROC5 models. Five-year binned extreme storm-surge events (fig. 21) range from 0.5 to 1.3 m and 1.0 to 2.0 m above MSL for the hindcast and projected time-periods, respectively. Linear least-square fits show statistically significant positive trends for the combined period of the hindcast and first half of the 21st century (1981 to 2050); trends are not statistically significant for the latter half of the century. Model results

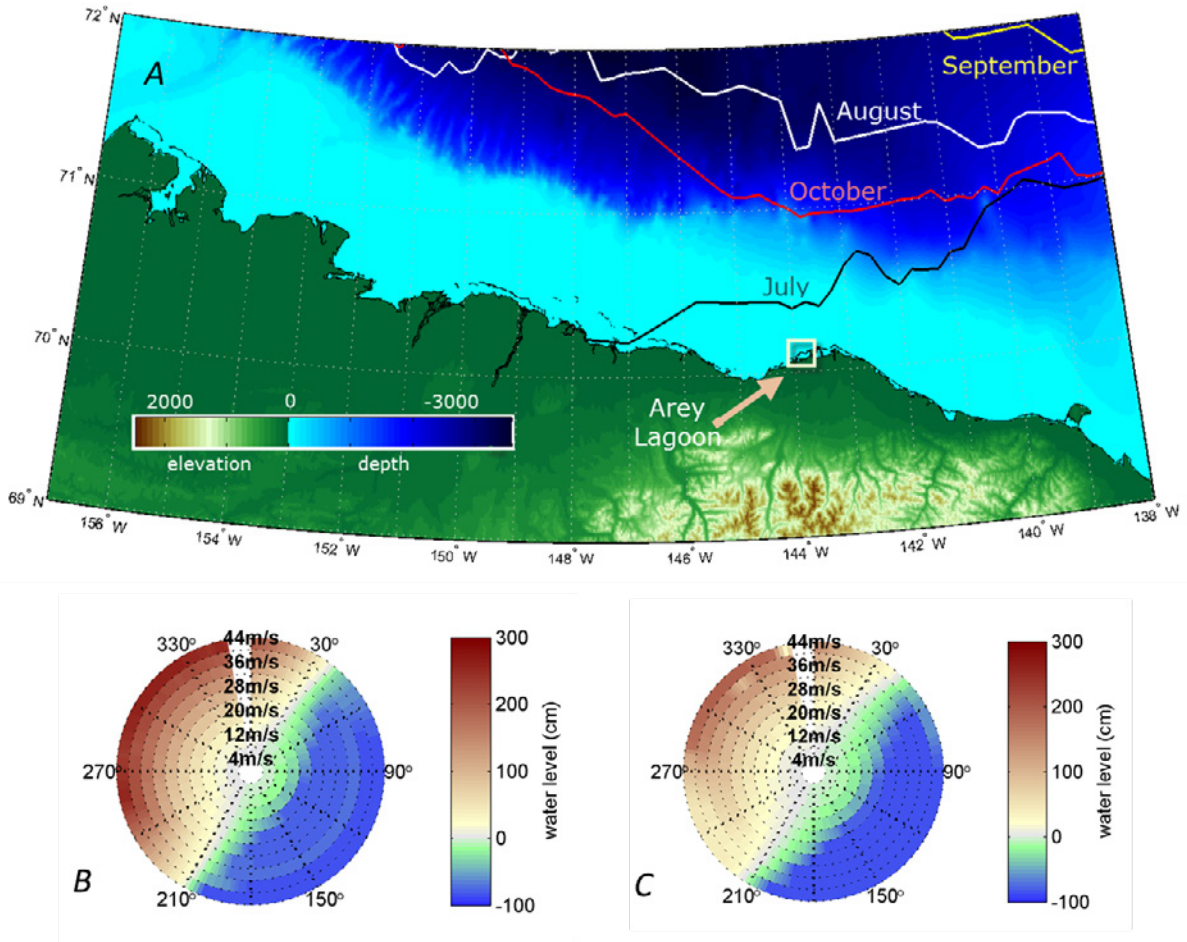

Figure 20. Map of measured monthly mean sea-ice extents along the Beaufort Sea coast, Alaska, and polar plots of modeled water levels in response to constant winds. *A*, Monthly mean sea-ice extents measured with satellite imagery (NOAA/OAR/ESRL PSD, 2013) from 1979 through 2012 show that the pack ice was north of the continental shelf for most open-water season months. *B*, Modeled surge levels (relative to mean sea level, MSL) assuming no sea ice. *C*, Modeled surge levels assuming sea-ice extents equivalent to the 1979–2012 July mean extent. Surge levels in *B* and *C* were extracted from a model grid point inside Arey Lagoon and represent results of constant winds blowing over the domain for a full day at 10° incremental directions and ranging in speed from 4 to 44 meters per second (m/s). Surge levels modeled with the August, September, and October monthly mean sea-ice extents are not shown but are nearly identical to the "no sea ice" case in *B*. m/s, meter per second; cm, centimeter.

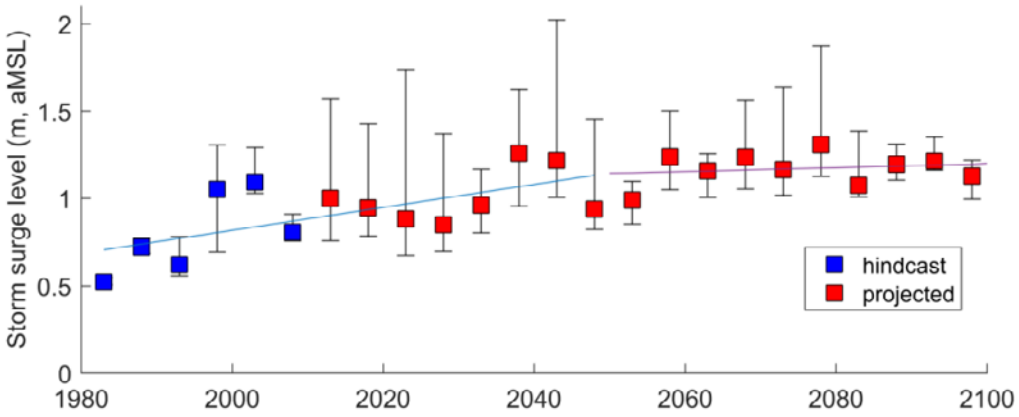

Figure 21. Time-series plot showing extreme storm surge levels and sea-level rise in Arey Lagoon, Alaska. Hindcast (NARR; 1981–2010) and projected (MIROC5, climate scenario RCP4.5; 2010–2100) water levels owing to sea level rise and storm surge at Arey Lagoon in response to spatially and temporally varying wind and sea-level pressure fields. Boxes represent the mean of the five highest events over a 5-year period and error bars represent the maximum and minimum of those top five events. Solid lines are least-square linear fits of the mean top five events. Linear fits are statistically significant at the *p*-value<0.05 level for the 1981–2050 period with an increase of 0.066 m/decade for the mean 5-year binned data and 0.15 m/decade for the 5-year binned extremes (fit line not shown). Linear fits through end of the century data (2050–2100) are not statistically significant indicating stabilizing conditions for the RCP4.5 scenario.

suggest an increase of 0.066 m/decade (~7 mm/yr; coefficient of determination, $r^2 = 0.42$; *p*-value <0.05) on average, with extremes increasing at about 0.15 m/decade for the years 1981–2050. Slightly more than half of the 5-year average storm surge trend can be attributed to the estimated value of sea-level rise, which was applied to all model runs by raising (for the projections) or lowering (for the hindcasts) the water level every year by 3.5 mm.

Modeled historical extremes at Arey Island were compared to available water-level observations from Prudhoe Bay and Tuktoyaktuk, the closest continuously operating gauges. The maximum event measured at Prudhoe Bay was ~1.2 m (~1.4 including astronomic tide) above MSL on August 11, 2000 (NOAA, 2016) (fig 20). This is comparable to hindcast water levels simulated at Arey Lagoon, which reached a maximum of 1.3 m above MSL. At Tuktoyaktuk, a maximum water level of 2.3 to 2.4 m above MSL has been inferred via identification of wrack (debris) lines. (Kowalik, 1984; Harper and others, 1988; Manson and Solomon, 2007), approximately 1 m higher than measured at Prudhoe Bay and that obtained with the numerical model for Arey Island. However, the dates of the maximum water levels at Tuktuoyaktuk precede the hindcast period simulated in this study. Additionally, Tuktuoyaktuk is located within a narrow strait, which increases the effect of storm surges as the flow of water is physically constrained. Overall, given limited opportunities for comparison, the storm surge levels simulated for Arey Island appear to be consistent with available data and previous modeling efforts in the region (Henry and Heaps, 1976; Reimnitz and Maurer, 1979; Harper and others, 1988).

Impact of Waves and Storm Surge on Arey Island Stability

Hindcast Period

Employing a significant wave height threshold value of greater than 2 m at the 10-m isobath and a positive storm surge, a total of 46 storm events were identified for the hindcast period, 1981–2010 (Appendix 1). Storm durations ranged from 1.5 to 10 days (average 3.5 days), but with the longer duration storms consisting of multiple peaks in both the storm surge and significant wave height time-series.

Total water elevations were estimated by adding maximum storm surge levels to wave runup for each of the identified storms. Wave runup was computed with the analytical model of Stockdon and others (2006) and an average beach slope of 0.05. Total water elevations for each of these storms are compared to Arey Island crest elevations in figure 22. For many of the storms, total water elevations exceed maximum crest heights, particularly along Arey Island-east and the approximate middle section of Arey Island-west, consistent with the overwash and breaching presented in the previous section on Shoreline Change.

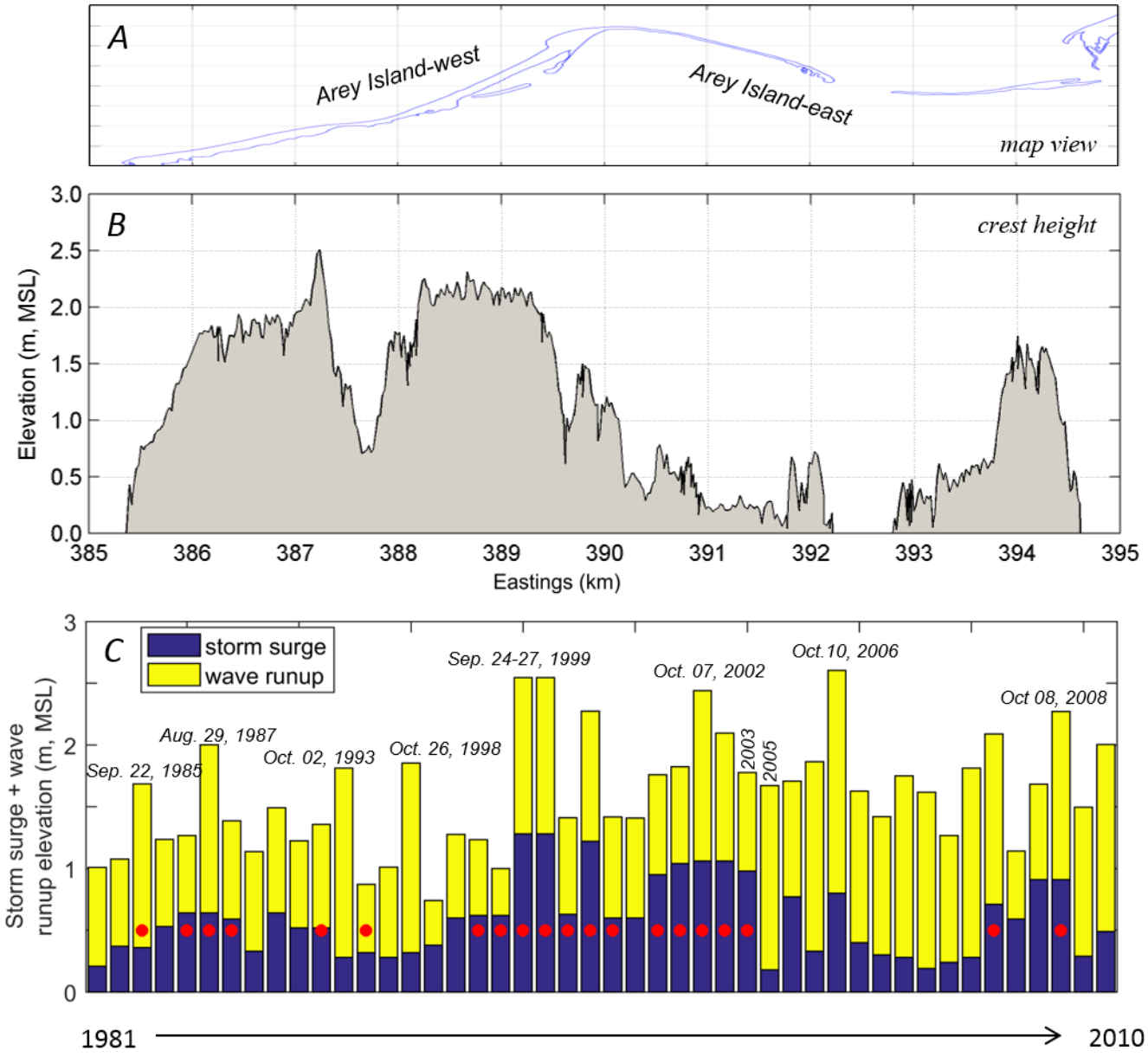

Figure 22. Plots comparing storm-generated total water elevations to topographic relief of Arey Island, Alaska. *A*, Map view of the shoreline, and *B*, crest height of Arey Island as measured with airborne lidar in 2009. *C*, Summation of storm surge and wave runup for 46 storm events identified with the hindcast model runs. Red circles indicate storm waves from northwest; other storms emanate from west to southwest. Note that total water elevations often exceed maximum crest heights, particularly along Arey Island-east and the approximate middle section of Arey Island-west, indicating that the Island is vulnerable to overwash and breaching. m, meter; MSL, mean sea level; km, kilometer.

Imagery in figure 11 shows multiple breaches of the eastern section in the periods 1979–1985 and 1992–1994 and in 1999; these correspond to several storms but most notably the higher storms of September 1985, October 1993, and September 1999. Two images taken just less than two months apart on August 5 and September 30, 1999 (upper two right panels in fig. 11), show breaching in the area of the present-day inlet (between kilometers 1 and 2, fig. 13). The short period between these two images coincides with the intense storms of September 24–27, 1999 (fig. 22*C*), suggesting that these storms were responsible for substantial changes in Arey Island-east. During the subsequent 5 years, through 2004, the inlet widened (fig. 11) and incident storm waves were predominantly from the north-northwest (filled red circles in fig. 22*C*). After 2004 and through 2010, accretion appears to have dominated causing the inlet to narrow while subject to storm waves from the west to southwest in all cases except two. The observed morphodynamics in combination with hindcast storm events suggest that Arey Island-east is most vulnerable to deterioration by northwest incident storms and that during other periods (west to southwesterly and easterly storms) sediment accretion, by way of aeolian processes and the convergence of longshore sediment transport, dominates the sediment transport signal.

Projected Period

Storm surge, significant wave height, peak wave period, and peak wave direction, derived from the D3D and WW3 models were used to simulate erosion, overwash, and migration of Arey Island for the near future term (2011 through 2035) using the XBEACH model (fig. 23). Forty-one percent of the storm waves modeled for this period are projected to be from the north-northwest.

Model results indicate that Arey Island-west will remain reasonably stable whereas Arey Island-east will continue to be subject to breaching and landward migration. For example, XBEACH simulations along profile 16, immediately west of the island's apex (fig. 23*B*), indicate that some foreshore will erode by the early 2030s, but otherwise this section of the island will remain stable. Along Arey Island-east, overwash and breaching is projected to occur immediately east of the island's apex (profile 24, fig. 23*E*), whereas farther east along profiles 22 and 28 (fig. 23*D*, *C*), the model projects vertical accretion and landward migration by as much as 120 m by the year 2035.

Although detailed XBEACH simulations were not completed for the remaining part of the 21st century, D3D model results of incident storm wave directions indicate that about

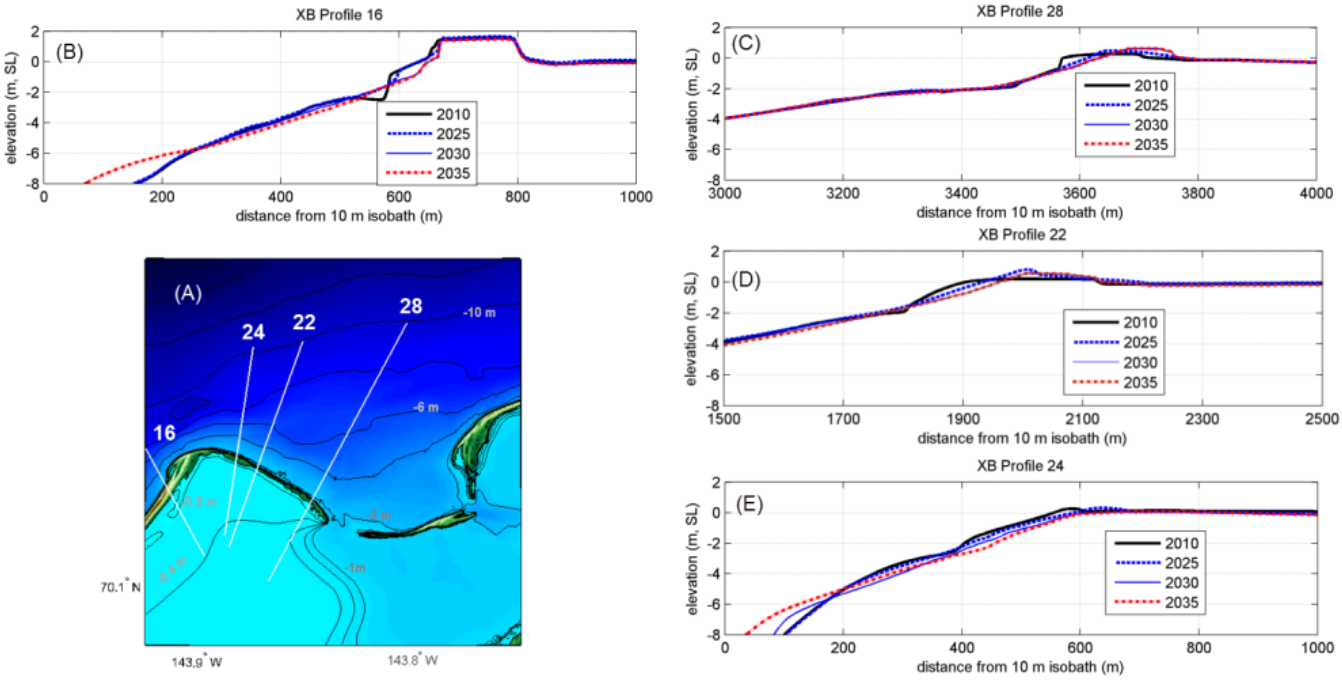

Figure 23. Plots showing examples of Arey Island, Alaska, profile changes as simulated with the XBEACH (XB) model until the year 2035. *A*, Overview map showing locations of XBEACH profiles. *B* through *E*, Profiles showing projected barrier island change (10x vertical exaggeration) as simulated with XBEACH model forced with storm conditions as derived with the Delft3D and SWAN models. m, meter; SL, sea level.

30 percent of the major storms between 2035 and 2100 will come from the northwest quadrant. Barring a lack of sediment supply, rapid sea-level rise, or other drastic changes in forcing conditions, it is not unreasonable to assume that Arey Island will continue to widen, shrink, breach, reform, and migrate but overall remain dynamically stable and continue to mitigate wave energy reaching the mainland shores of Arey Lagoon. Thus, the flood potential of Arey Lagoon mainland coast was quantified with a focus on sea-level rise and storm surge, excluding the effects of wave runup.

Inundation and Flood Potential of Arey Lagoon Mainland Coast

Assuming that the barrier island will remain dynamically stable and will continue to offer protection to the mainland lagoon coast from direct wave energy, the flood potential from sea-level rise and storm surge was quantified by applying water levels at the open boundary of a 5-m-resolution D3D model grid that was used to numerically simulate water flow across the study domain. Results are presented below for (1) permanent flooding caused by sea-level rise and (2) intermittent flooding caused by sea-level rise plus storm surge.

Projected Permanent Inundation

In the absence of storm surge, sea-level rise (0.35 cm/decade) is expected to permanently inundate 1.6 square kilometers (km^2) of Arey Lagoon mainland shores by 2100 (fig. 24). At a rate of 3.5 cm/decade, the total rise in sea level is estimated to be 31.5 cm by the year 2010 (fig. 9). Uncertainty of the elevation data is estimated to be ±15 cm owing to the lack of good vertical control in the region; this range of uncertainty is represented by the 16.5 and 46.5 cm inundation surfaces shown in figure 24, corresponding to 0.6 and 2.3 km^2 of permanently flooded area, respectively, relative to 2010.

Intermittent Flood Potential

Because vegetation is likely to be most vulnerable to saltwater contact early in the summer season when soils thaw to at least the root zone and growth begins, we first compared historical air temperatures with the onset of the open-water season to ascertain the importance in timing of storm events and vegetation growth. Most soil microbes are relatively inactive at temperatures below 5–10 °C (“biological zero”) (for example, Rabenhorst, 2005). Weijers and others (2013) showed that the growing degree-day (GDD) 5 parameter,

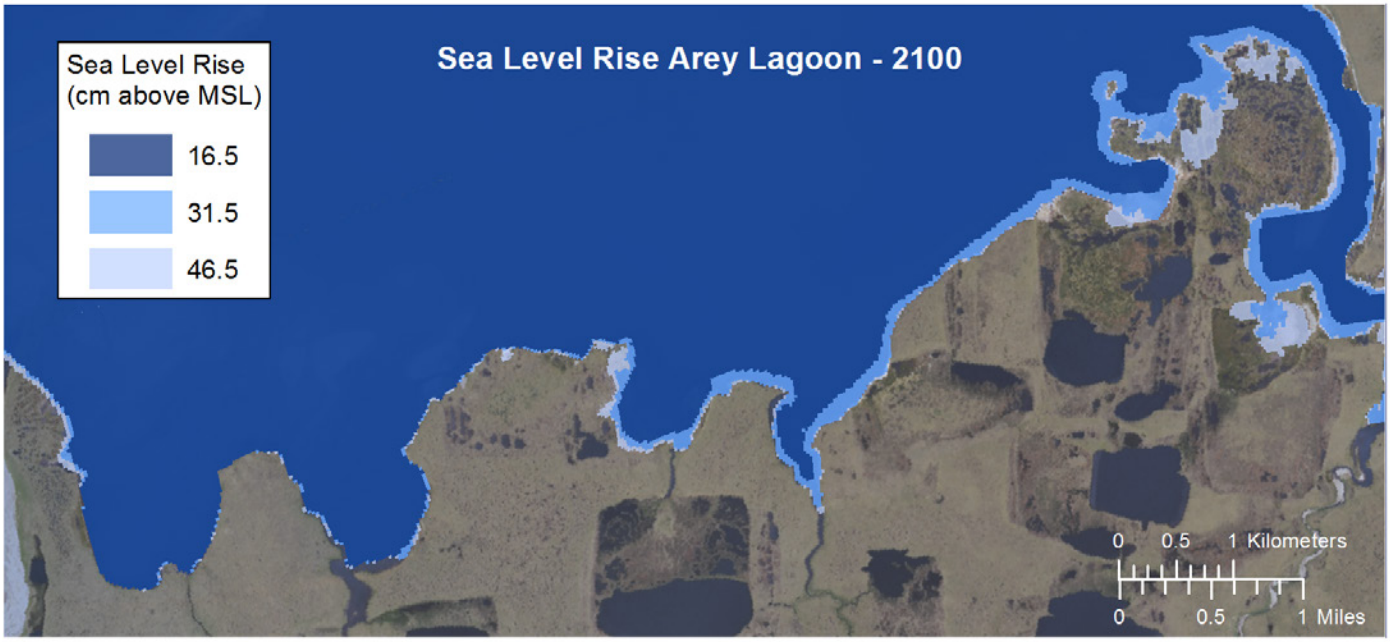

Background image courtesy UAF-GINA (http://alaskamapped.org/bdl); includes material © CNES 2011, Distribution Spot Image S.A., France, SICORP, USA, all rights reserved

Figure 24. Map showing inundation extent of Arey Lagoon, Alaska, mainland coast caused by 31.5 centimeters (cm) of sea-level rise. Lower and upper ranges (16.5 and 46.5 cm, respectively) are based on uncertainty of the elevation data relative to mean sea level (MSL).

defined as the cumulative daily mean temperature above 5 °C, well predicts the high Arctic growing season. Using this concept, GDD5 was calculated from daily mean air temperatures measured at Barter Island and plotted against the first day of the open-water season (= first day of possible saltwater flooding) for the hindcast period (fig. 25). Points above the 1:1 line (gray shaded area in fig. 25) indicate the possibility of saltwater flooding prior to inception of vegetation growth, whereas data points that fall below the 1:1 line indicate that vegetation growth precedes the open-water season. In more than 90 percent of the hindcast years, vegetation growth is estimated to have begun prior to the open-water season and thus might be considered more resilient to saltwater flooding. This chronology of root growth prior to open-water conditions was assumed to hold for all simulations of future conditions, thus eliminating the need to split the storm surge time-series into growing seasons.

Maps depicting flooding by sea-level rise plus storm surge were generated with two flood frequencies in mind: low-frequency extreme events that may kill non-saline tolerant vegetation, and monthly events that might provide intermittent salinization necessary for some halophytic coastal meadows.

Extreme flood extents are shown in figure 26 for the maximum and 25-year return period storm events of the first (2000–2049) and second (2050–2100) halves of the 21st century. Twenty-five-year return period storm surge levels were identified by sorting, ranking, and plotting individual storm-related water-level maxima on a probability scale and selecting the 25-year events for each period; a hybrid of the hindcast and projected water-level time-series (up through 2049) was used in determination of the 25-year event for the first half of the century. The 25-year storm surge level has a 1 in 25 (4 percent) chance of occurring in any one year, regardless of when the last such event was.

The 25-year and maximum storm surge levels for the first half of the century were found to be 1.70 and 1.95 m above MSL, respectively. Because of the generally low relief, this translates to more than 9 km^2 of flooded tundra, much of which consists of salt-intolerant vegetation (fig. 25). The 25-year and maximum events for the latter half of the century (2050–2100) are slightly lower at 1.60 and 1.80 m, respectively, and don't extend quite as far inland. The water level of the extreme event is projected to be about 20 cm higher than the 25-year event for the same period (1.80 m versus 1.60 m). However, because of the steepened tundra topography within the flooded areas, there is little difference in the extent of inland flooding between these two extreme water levels.

Monthly flood extents that might be expected to maintain halophytic vegetation were calculated by extracting the second highest maximum monthly water level of each open-water

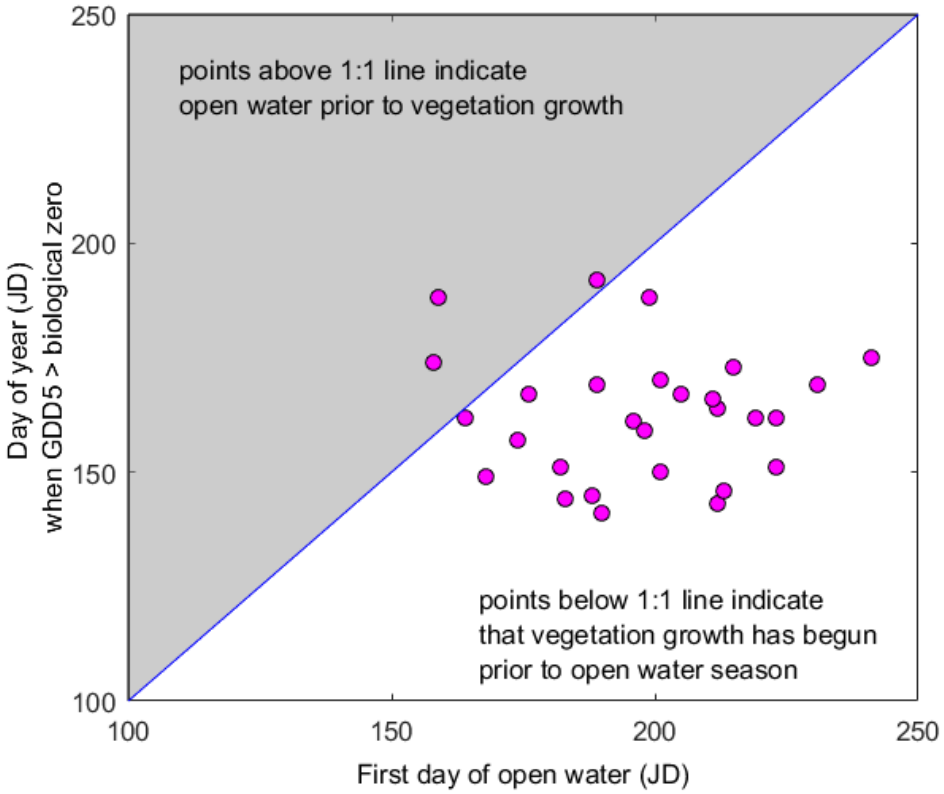

Figure 25. Scatter plot comparing the first day when growing degree-days (GDD) exceed "biologic zero" to the first day of possible saltwater flooding along Arey Lagoon, Alaska, shores. Points above the 1:1 line (gray shaded area) indicate the possibility of saltwater flooding prior to inception of vegetation growth. Data points that fall below the 1:1 line indicate that vegetation growth preceded the open-water season and that these plants were less susceptible to saltwater flooding as the roots had had a chance to establish. Vegetation growth is estimated to have begun prior to the open-water season for more than 90 percent of the 28 years analyzed. DOY, day of year.

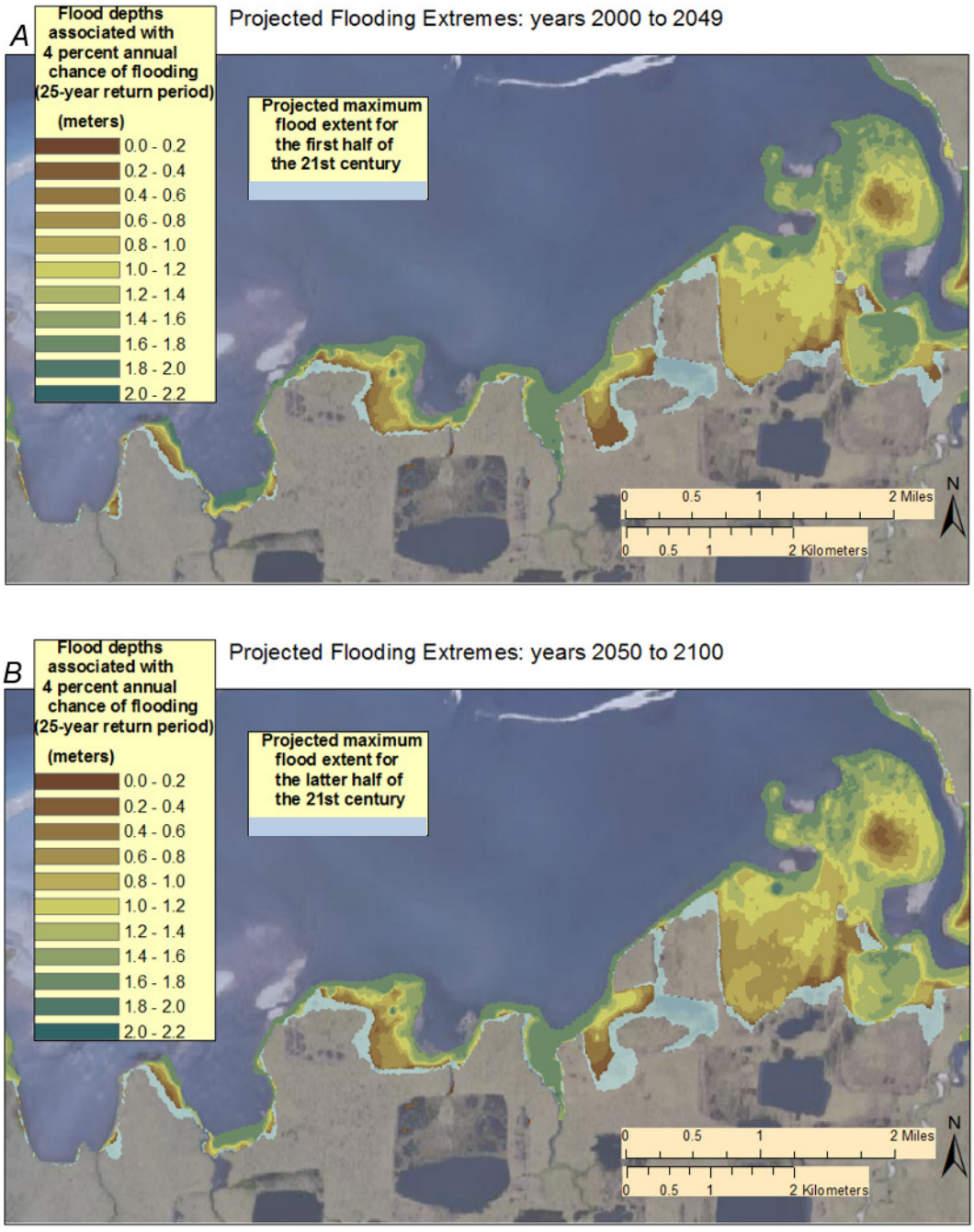

Figure 26. Maps showing projected maximum and depth of 4 percent annual chance of flooding along the mainland coast of Arey Lagoon, Alaska, during the first and latter halves of the 21st century. Flood extents represent contributions from storm surge and sea level rise. *A*, Projected flood depths (graded colors) resulting from the 25-year return period (4 percent annual chance) flood elevation and maximum flood extent (transparent blue color) associated with the projected maximum flood level for years 2000–2049. *B*, Same as in *A* for years 2050–2100.

month that had more than 21 days (~70 percent) of open water (between 3 and 5 months each year). Median values of decadal bimonthly water-level time-series (including sea-level rise) increase incrementally from 0.44 to 0.77 m, relative to mean sea level in 2010. The temporal trend is strongly linear (r^2 = 0.82; p-value<0.005) with an amplitude, or rate of change, nearly identical to the sea-level rise component. Modeled flood extents also show incremental increases through time (fig. 27). An exception is the last three decades, between 2071 through 2100, when the bimonthly flood extents are relatively similar (fig. 27*D*). At these water levels (70, 71, and 77 cm for the last three decades of the 21st century) saline floodwater reaches relatively steeper topographic terrain that inhibit farther landward flow. However, the model does not account for erosion or permafrost deflation, which could result in greater pattern variations and farther inland flood extents.

Whereas an underlying linear trend in bimonthly water levels exists, there is much variation about that trend as can be seen in figure 28 where annually averaged bimonthly flood extents (yellow line) are plotted against time. A 5-year running mean (black dashed line in fig. 28) shows that the areal extent of bimonthly flooding is projected to increase through the 21st century and cycles of non-seasonal variations (gray shaded areas in fig. 28) are superimposed on a linear trend (not shown). Similar to the hindcast and projected time-series of deepwater wave heights (figs. 16 and 17) and storm surge (fig. 21), the periodicity is about 30 to 40 years. The peaks indicate exceptionally large flood extents compared to the immediately preceding years. Best-fit lines through each peak and its preceding low point in the 5-year running mean yields the rate at which flood extents are expected to expand. The rates of expansion decrease from 0.33 km^2/yr between 1996 and 2014, to 0.15 km^2/yr between 2033 and 2038, and to 0.25 km^2/yr between 2060 and 2065. However, the latter two events are closely followed by similar rates as shown with the double peaks in figure 28 for years 2030–2050 and 2060–2082. Overall, the duration of each peak cycle is shown to increase from 18 years between 1996 and 2014 to 20 years and 22 years during the mid and latter parts of the 21st century, respectively.

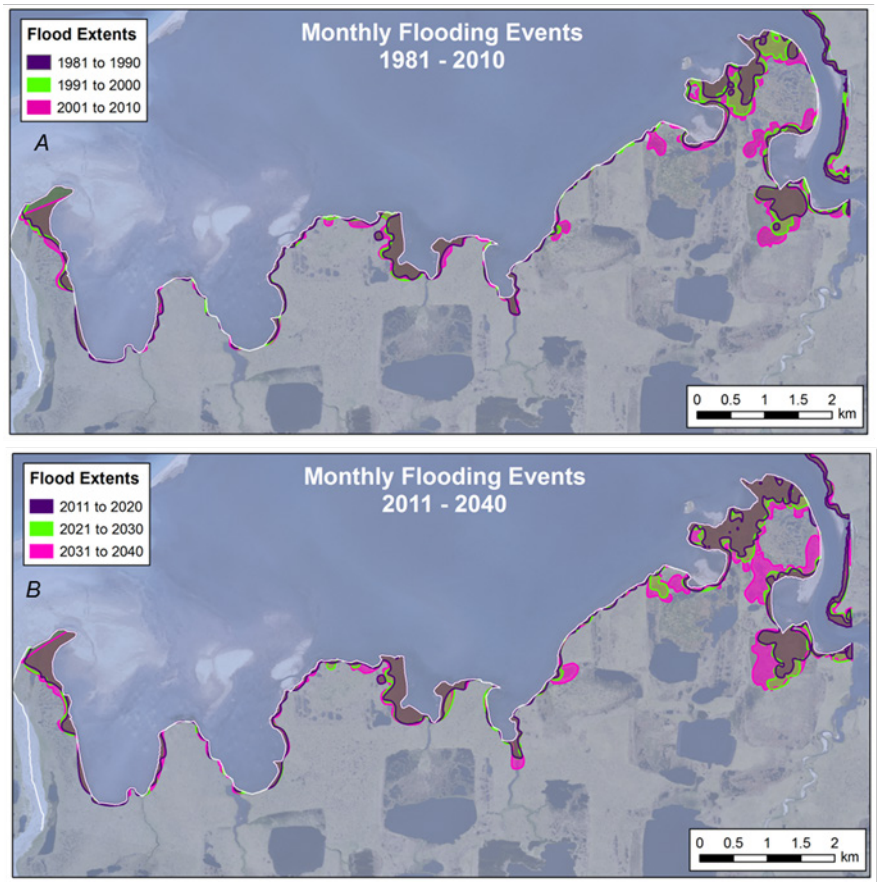

Figure 27 (pages 32–33). Maps showing decadal median bimonthly flood extents of Arey Lagoon, Alaska, mainland coast for *A*, the hindcast period (1981–2010) and (*B*–*C*) three projected 30-year time-slices (years 2011–2040, 2041–2070, and 2071–2100). Median monthly water levels (including sea-level rise and storm surge) range from 0.46 meters (m) (1981–1990 decade) to 0.91 m (2071–2080 decade) above approximate mean sea level in 2010. km, kilometers.

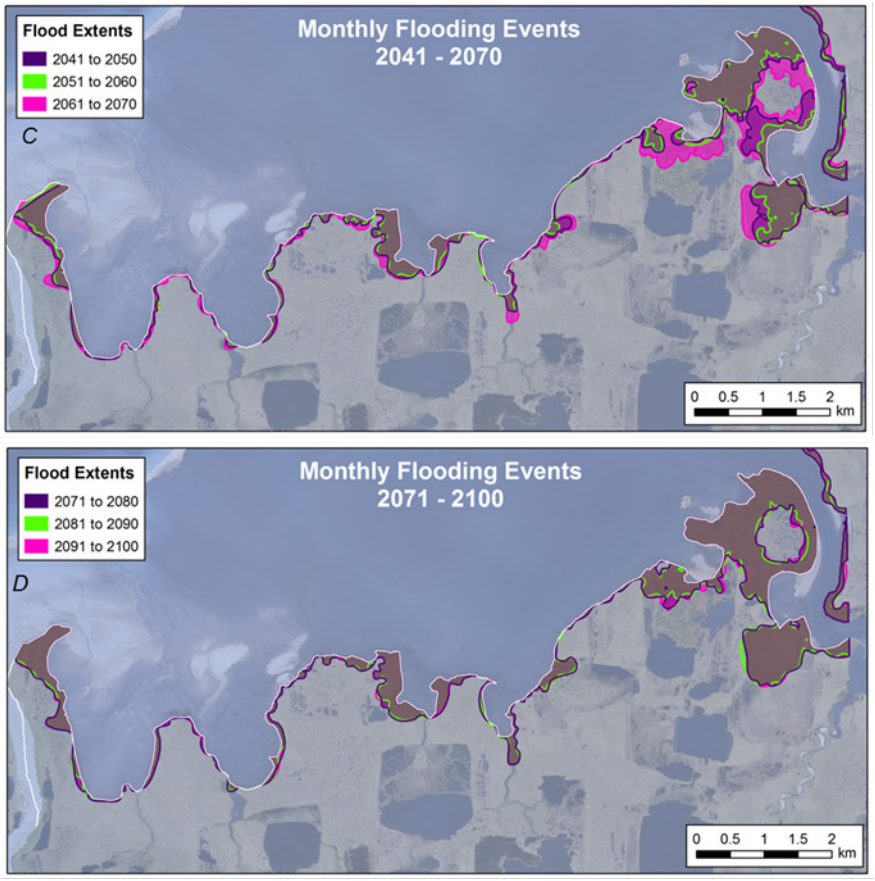

Figure 27 (pages 32–33).—Continued

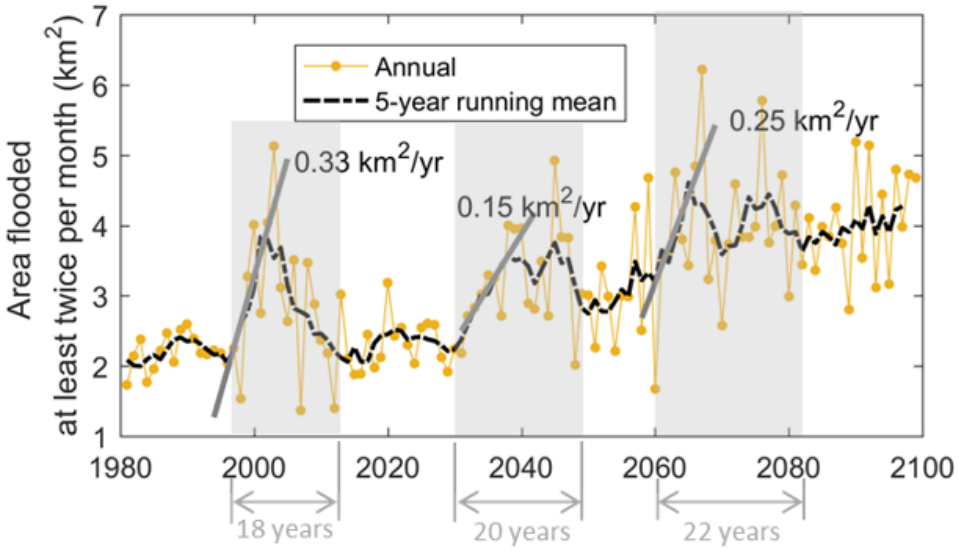

Figure 28. Graph showing twice-monthly flood extents surrounding Arey Lagoon, Alaska, for the hindcast (1981–2010) and projection years (2011–2100). A 5-year running mean (dashed black line) is plotted through averaged annual twice-monthly flood extents (from tides, storm surge, and relative sea-level rise). The number of months varied each year and was only included in the analysis if more than about 70 percent of the month (21 days) was open water. Exceptionally high rates of expanding flood extents were modeled for the 1996–2014, 2030–2050, and 2060–2082 periods (gray shaded areas). Note that the duration of each peak cycle increases with time. km^2, square kilometer; yr, year.

Summary of Findings and Conclusions

Historical Shoreline Change Rates of Arey Island and Arey Lagoon Mainland Shore

- Digitization and analysis of T-sheets, aerial imagery, and airborne lidar show that the western part of Arey Island has been relatively stable (average long-term rate of -0.1±0.3 m/yr) to slightly accretional, whereas the northwest-southeast trending eastern section migrated to the southwest (landward) by as much as 900 m between 1947 and 2009.
- Because of its relatively low relief, the eastern section of Arey Island is most susceptible to breaching and overwash. Reformation and near reattachment of island sections are common and appear to occur during periods when northwesterly storms are less frequent.
- The long-term (1947–2009) rate of change along the Arey Lagoon mainland coast is slightly erosional (average -0.7±0.3 m/yr) and relatively uniform along the entire shore, except for three areas that may have been exposed to incident wave energy passing through gaps in the barrier island chain during times of breaching. No significant variation in shoreline change rates through time were observed for the Arey Lagoon mainland coast.

Projected Ocean Storm Conditions and Changes with Respect to the Recent Past

- Numerically modeled deepwater extreme wave heights are projected to increase most rapidly during the first half the 21st century with rates of +0.35 m/decade and +0.49 m/decade through the year 2045 for Representative Concentration Pathways (RCP) 4.5 and RCP8.5, respectively. Rates of increase are less than half as high (+0.14 m/decade and +0.18 m/decade) when considering the entire modeled period (1981 and 2100).
- A temporal trend in extreme wave heights immediately offshore of Arey Island was not found. It is speculated that dissipation of wave energy and limited wave growth across the wide (~100 km) continental shelf are largely responsible for the mitigated wave heights modeled from deep water to the shore. Although an overall temporal trend was not found, maximum significant wave height (4.4 m) is projected to exceed any modeled historical event by ~0.4 m for the RCP4.5 climate scenario.
- Wind-induced storm surges are influenced by the high latitude of the study location (above lat. 70° N.) and the Coriolis force which causes water to deflect to the right in the northern hemisphere; thus, westerly winds yield a pile-up of water along the east-west trending Arctic coast, whereas easterly winds yield a set-down (lowering) along the coast. Because larger positive storm surges occur during westerly winds, only storms from the northwest quadrant are of relevance to breaching of Arey Island and flooding of the lagoon mainland coast.
- Elevated storm surges, modeled with temporally and spatially varying wind and pressure fields for the historical period and future RCP4.5 climate scenario, are projected to increase as much as 0.15 m/decade (binned 5-year extrema) between 1981 and 2050 and with no apparent trend thereafter. Hindcast (1981–2010) extreme surge levels range from 0.5 to 1.3 m and compare well with the Prudhoe Bay station (~175 km west of Arey Lagoon, measurements available between 1990 and 2016) which recorded a maximum water level of 1.4 m (1.2 m excluding astronomic tides) in 2011. Maximum projected water levels, excluding contributions from waves, are about 2.0 m above mean sea level (MSL) thus reflecting a maximum increase of 0.7 m over the 21st century. Slightly more than 20 percent of the projected increase is attributable to sea-level rise, which was estimated to be 3.5 mm/yr based on a literature review.
- Analysis of satellite-derived sea-ice extents shows that the duration of the open-water season has more than doubled from about 50 days in the early 1980s to approximately 120 days in the 2010s near Arey Lagoon. Results from four global climate models (GCMs) representing the RCP4.5 climate scenario indicate that open-water duration will continue to increase but at a slower pace compared to the historical period. Most importantly, the end of the open-water season is projected to extend to at least the end of November by the year 2100. Because more frequent and intense storms occur in August or later, the later refreeze is most critical to the barrier island lagoon system.
- Owing in part to the extended open-water season, the number of northwesterly storms affecting the region is expected to increase from less than 5 events per year prior to 2010 to as many as 30 events per year by the end of the century.

Future Stability of the Barrier Island Chain and its Capacity in Modulating Wave Energy Reaching Coastal Wet Sedge Areas within Arey Lagoon

- Morphodynamic simulations of Arey Island subjected to individual storms through the year 2035 suggest that the western part of the island will remain

reasonably stable whereas the eastern section will continue to be subject to breaching and landward migration. The extent to which migration might continue depends on availability of sediment for reformation and reattachment of island sections (as documented in historical imagery), whether or not currents are strong enough to transport available sediment, and available accommodation space within the lagoon. Model simulations indicate that currents are sufficiently strong to transport sediment presently available on the islands, but less is understood about future availability of sediment quantities and whether or not the migration rate will remain steady. Thus, indications are that Arey Island will remain dynamically stable (migrate, widen, shrink, breach, and reform) in the coming decades but with a large degree of uncertainty.

- The barrier island chain, in its form as measured with airborne lidar in 2009, is shown to substantially modulate wave energy reaching Arey Lagoon and fringing coastal wet sedge areas; wave energy is fully blocked from entering the western part of the Lagoon and only enters the Lagoon where openings exist along the eastern flank of Arey Island. Because the barrier island chain substantially reduces wave energy reaching the lagoon and Arey Island is projected to be relatively stable during at least the early parts of the 21st century, changes in the frequency and extent of flooding of lagoon shores (including highly valued coastal wet sedge areas) will largely be driven by changes in storm surge.

Effects of Sea-level rise and Changing Storm Conditions on the Frequency and Extent of Flooding

- The model shows that the wet sedge focus study site and the area of the drained thermokarst lake to the west will be under water for most of the open-water season by the end of the 21st century and that parts of the wet sedge peninsula will be inundated (permanently flooded) as early as the 2030s. Similarly, the low-lying eastern half of Arey Island will be underwater for most of the open-water season toward the end of the century.
- Flood maps were generated for the 25-year and maximum events of the first and latter halves of the 21st century. The 25-year (1.70 m, relative to MSL in 2010) and maximum (1.95 m) events are slightly higher (10 and 15 cm) for the first half of the century compared to the latter half. Because of the generally low relief, these extreme flood events translate to more than 9 km^2 of flooded tundra, much of which consists of salt-intolerant vegetation. Note that the maps represent flooding by sea-level rise and storm surge only; if there is insufficient sediment transport to support accretion and build-up of Arey Island-east, the coastal wet sedge and surrounding mainland lagoon coast will be exposed to open ocean waves that, superimposed on storm surge, will likely exacerbate erosion and cause farther inland flooding compared to flood extents resulting only from storm surge and sea-level rise.
- Bimonthly flood extents that might provide intermittent salinization necessary for some halophytic coastal meadows were projected to double by the end of the 21st century from ~2.2 km^2 in 1981–1990 to 4.4 km^2 in 2090–2100. Although the bimonthly water levels increase by nearly 10 cm between 2070 and 2100, flood extents remain approximately unchanged as they are limited by steep terrain at this water-level range. The flood depth is, however, expected to increase.
- Superimposed on the overall weak but statistically significant linear trend of annual increases in bimonthly flood extents (0.019 km^2/yr, $r = 0.41$) are peaks of exceptionally large flood extents every 30 to 40 years (fig. 27). Three periods of accelerating rates of bimonthly flooding are hindcast and projected: 0.33 km^2/yr between 1996 and 2014, 0.15 km^2/yr between 2033 and 2038, and 0.25 km^2/yr between 2060 and 2065. The number of years over which these greater flood expansion rates are hindcast and projected to occur appears to be increasing from 18 years starting in 1996, to 20 years starting in 2033, and to 22 years starting in 2060. The accelerating rates and increasing durations over which greater rates are hindcast and projected to occur likely reflect broad scale climate variations; this hypothesis is supported by previous studies that suggested increasing durations of, for example, the Northern Annual Mode using 75 different CMIP5 model simulations (Gillett and Fyfe, 2013).

Results of this study, such as the projected rates of permanent flooding owing to sea level rise, intermittent flood extents and depths owing to extreme storm events and sea-level rise, accelerating and decelerating rates of bimonthly flooding owing to sea-level rise, climatic cycles, and changing atmospheric patterns may be used in future work to assess impacts of changing Arctic oceanographic conditions on stability or potential for upland migration of coastal wet sedge colonies and overall habitat availability.

References Cited

Arnborg, L., Walker, H.J., and Peippo, J., 1966, Water discharge in the Colville River, 1962. Geografiska Annaler, v. 48, p. 195–210.

Arp, C., Jones, B., Schmutz, J., Urban, F., and Jorgenson, M.T., 2010, Two mechanisms of aquatic and terrestrial habitat change along an Alaskan Arctic coastline: Polar Biology, v. 33, no. 12, p. 1629–1640.

Atkinson, D.E., 2005, Observed storminess patterns and trends in the circum-Arctic coastal regime: Geo-Marine Letters, v. 25, p. 98–109, https://doi.org/10.1007/s00367-004-0191-0.

Barnard, P.L., Rubin, D.M., Harney, J., and Mustain, N., 2007, Field test comparison of an autocorrelation technique for determining grain size using a digital 'beachball' camera versus traditional methods: Sedimentary Geology, v. 201, p. 180–195.

Barnes, P.W., and Reimnitz, E., 1974, Sedimentary processes on Arctic Shelves off the northern coast of Alaska, *in* Reed, J.C., and Sater J.E., eds., The Coast and Shelf of the Beaufort Sea, Proceedings of the Beaufort Sea Coast and Shelf Research Symposium: Arlington, Va., Arctic Institute of North America, p. 439-476

Barnes, P.W., Reimnitz, E., and Rollyson, B.P., 1992, Map showing Beaufort Sea coastal erosion and accretion between Flaxman Island and the Canadian border, northeastern Alaska: U.S. Geological Survey Miscellaneous Investigations Series, Map I–1182–H, scale 1:82,000, 22 p.

Barnes, P.W., and Rollyson, B.P., 1991, Erosion and accretion along the Arctic coast of Alaska—The influence of ice and climate, *in* Kraus, N.C., Gingerich, K.J., and Kriebel, D.L., Coastal Sediments '91—Specialty Conference on Quantitative Approaches to Coastal Sediment Processes, Seattle, Wash., 1991, Proceedings: New York, American Society of Civil Engineers, p. 1518–1531.

Barnes, P.W., Schell, D.M., Reimnitz, E., eds., 1984, The Alaskan Beaufort Sea—Ecosystems and Environments: Orlando, Fla., Academic Press, 466 p.

Bengtsson, L., Hodges, K.I. and Roeckner, E., 2006, Storm Tracks and Climate Change: Journal of Climate, v. 19, p. 3518–3543.

Black, R.F., 1964, Gubik Formation of Quaternary age in Northern Alaska, chap. C *of* Exploration of Naval Petroleum Resrve No. 4 and adjacent areas, northern Alaska, 1944–53; Part. 2, Regional Studies: U.S. Geological Survey Professional Paper 302, p. 59–91.

Booij, N., Ris, R.C., and Holthuijsen, L.H., 1999, A third-generation wave model for coastal regions Model description and validation, Journal of Geophysical Research, v. 104, C4, p. 7649–7666.

Brodzik, M.J., and Armstrong, R., 2013, Northern Hemisphere EASE-Grid 2.0 weekly snow cover and sea ice extent, version 4: Boulder, Colo., National Snow and Ice Data Center dataset, accessed October 1, 2013, at https://doi.org/10.5067/P7O0HGJLYUQU.

Brown, J., and Sellman, P.V., 1973, Permafrost and coastal plain history of arctic Alaska, *in* Britton, M.E., ed., Alaskan arctic tundra: Arctic Institute of North America Technical Paper 25, p. 31–47.

Buscombe, D., Rubin, D.M., and Warrick, J.A., 2010, A universal approximation of grain size from images of noncohesive sediment: Journal of Geophysical Research, v. 115, no. F02, 17 p., https://doi.org/10.1029/2009JF001477.

Campeau, S., Hequette, A., and Pienitz, R., 2000, Late Holocene diatom biostratigraphy and sea-level changes in the southeastern Beaufort Sea: Canadian Journal of Earth Sciences, v. 37, p. 63–80.

Craig, P.C., and Haldorson, L.J., 1981, Fish, pt. 4 *in* Johnson, S.R., and Richardson, J.W., eds., Beaufort Sea barrier island-lagoon ecological process studies—Final report, Simpson Lagoon: Boulder, Colo., National Oceanic and Atmospheric Administration, Environmental Assessment of the Alaskan Continental Shelf—Final Reports, v. 7, Biological Studies, p. 384–649.

Danielson, S., Johnson, M., Solomon, S., and Perrie, W., 2008, Gridded Bathymetric Dataset Based on Ship Soundings—A research tool for the waters of eastern Russia, Alaska & western Canada [abs.] Alaska Marine Science Symposium 2008, Anchorage, Alaska. [Data available at http://mather.sfos.uaf.edu/~seth/bathy/.]

Deltares, 2010, Delft3D-FLOW; Simulation of multi-dimensional hydrodynamic flows and transport phenomena, including sediments—User Manual (ver. 3.14, revision 11214): Delft, Netherlands, Deltares.

Derksen, D., Eldridge, W., and Weler, M., 1982, Habitat ecology of Pacific Black Brant and other geese moulting near Teshekpuk Lake, Alaska: Wildfowl, v. 33, p. 39–57.

Donnelly, C., Kraus, N.C., and Larson, M., 2004, Coastal overwash—Part 1, Overview of processes: Vicksburg, Miss., U.S. Army Corp of Engineering, Engineer Research and Development Center, Coastal and Hydraulics Laboratory, Coastal and Hydraulics Engineering Technical Note ERDC/CHL CHETN-XIV-13, 17 p., available at http://hdl.handle.net/11681/4992.

Dunton, K.H., Weingartner, T., and Carmack, E.C., 2006, The nearshore western Beaufort Sea ecosystem—Circulation and importance of terrestrial carbon in arctic coastal food webs: Progress in Oceanography, v. 71, p. 362–378.

Erikson, L.H., Gibbs, A.E., Richmond, B.M., Jones, B.M., Storlazzi, C.D., and Ohman, K.A., 2020, Modeled 21st century storm surge, waves, and coastal flood hazards, and supporting oceanographic and geological field data (2010 and 2011) for Arey and Barter Islands, Alaska and vicinity: U.S. Geological Survey data release, https://doi.org/10.5066/P9LGYO2Q.

Erikson, L.H., Hegermiller, C.E., Barnard, P.L., and Storlazzi, C.D., 2016, Wave Projections for United States Mainland Coasts: U.S. Geological Survey summary of methods to accompany data release, https://doi.org/10.5066/F7D798GR.

Erikson, L.H., Storlazzi, C.D., and Jensen, R.E., 2011, Wave climate and trends along the eastern Chuckchi Arctic Alaska coast, *in* Wallendorf, L.A., Jones, C., Ewing, L., Battalio, B., eds., Solutions to Costal Disasters Conference, Anchorage, Alaska, 2011, Proceedings: Reston, Va., American Society of Civil Engineers, p. 273–285, https://doi.org/10.1061/41185(417)25.

Garrison, 1996, Oceanography—An Invitation to Marine Science (2d ed.): Belmont, Calif., Wadsworth Publishing Company, 592 p.

Gibbs, A.E., Harden, E.L., Richmond, B.M., and Erikson L.H., 2011, Regional shoreline change and coastal erosion hazards in Arctic Alaska, *in* Wallendorf, L.A, Jones, C., Ewing, L., and Battalio, B., eds., Solutions to Costal Disasters Conference, Anchorage, Alaska, 2011, Proceedings: Reston, Va., American Society of Civil Engineers, p. 258–272, https://doi.org/10.1061/41185(417)24.

Gibbs, A.E., and Richmond, B.M., 2009, Oblique aerial photography of the Arctic coast of Alaska, Nulavik to Demarcation Point, August 7-10, 2006: U.S. Geological Survey Data Series 436, 6 p., 4 databases [http://pubs.usgs.gov/ds/436/]

Gibbs, A.E., and Richmond, B.M., 2015, National assessment of shoreline change—Historical shoreline change along the north coast of Alaska, U.S.–Canadian border to Icy Cape: U.S. Geological Survey Open-File Report 2015–1048, 96 p., https://doi.org/10.3133/ofr20151048.

Gillett, N.P., and Fyfe, J.C., 2013, Annular mode changes in the CMIP5 simulations: Geophysical Research Letters, v. 40, p. 1189–1193, https://doi.org/10.1002/grl.50249.

Graham, N.E., Cayan, D.R., Bromirski, P.D., and Flick, R.E., 2012, Multi-model projections of twenty-first century North Pacific winter wave climate under the IPCC A2 scenario: Climate Dynamics, v. 40, p. 1335–1360, https://doi.org/10.1007/s00382-012-1435-8.

Griffiths, W.B., and Dillinger, R.E., 1981, Invertebrates, pt. 5, *in* Johnson, S.R., and Richardson, J.W., eds., Beaufort Sea barrier island-lagoon ecological process studies—Final report, Simpson Lagoon: Boulder, Colo., National Oceanic and Atmospheric Administration, Environmental Assessment of the Alaskan Continental Shelf—Final Reports, v. 8, Biological Studies, p. 1–198.

Hapke, C.J., Reid, D., Richmond, B.M., Ruggiero, P., and List, J., 2006, National assessment of shoreline change—Part 3, Historical shoreline changes and associated coastal land loss along the sandy shorelines of the California coast: U.S. Geological Survey Open-File Report 2006–1219, 72 p., accessed March 15, 2013, at https://pubs.usgs.gov/of/2006/1219/.

Harper, J.R., Henry, R.F., and Stewart, G.G., 1988, Maximum storm surge elevations in the Tuktoyaktuk Region of the Canadian Beaufort Sea: Arctic, v. 41, no. 1, p. 48–52.

Henry, R.F., and Heaps, N.S., 1976, Storm surge in the southern Beaufort Sea: Journal of the Fisheries Research Board of Canada, v. 33, no. 10, p. 2362–2376.

Hequette, A., and Ruz, M.-H., 1991, Spit and barrier island migration in the southeastern Canadian Beaufort Sea: Journal of Coastal Research, v. 7, no. 3, p. 677–698.

Hinzman, L.D., Bettez, N.D., Bolton, W.R., Chapin, F.S., Dyurgerov, M.B., Fastie, C.L., Griffith, B., Hollister, R.D., Hope, A., Huntington, H.P., Jensen, A.M., Jia, G.J., Jorgenson, T., Kane, D.L., Klein, D.R., Kofinas, G., Lynch, A.H., Lloyd, A.H., McGuire, A.D., Nelson, F.E., Oechel, W.C., Osterkamp, T.E., Racine, C.H., Romanovsky, V.E., Stone, R.S., Stow, D.A., Sturm, M., Tweedie, C.E., Vourlitis, G.L., Walker, M.D., Walker, D.A., Webber, P.J., Welker, J.M., Winker, K.S., and Yoshikawa, K., 2005, Evidence and implications of recent climate change in northern Alaska and other Arctic regions: Climatic Change, v. 72, no. 3, p. 251-298, https://doi.org/10.1007/s10584-005-5352-2.

Hopkins, D.M., and Hartz, R.W., 1978, Coastal morphology, coastal erosion, and barrier islands of the Beaufort Sea, Alaska: U.S. Geological Survey Open-file Report 78–1063, 54 p.

Hume, J.D., and Schalk, M., 1967, Shoreline processes near Barrow, Alaska; a comparison of the normal and the catastrophic: Arctic, v. 20, no. 2, p. 86–103.

Hunt, I.A., Jr., 1959, Design of seawalls and breakwaters: Journal of the Waterways and Harbors Division, American Society of Civil Engineers, v. 85, no. 3, p. 123–152.

Intergovernmental Panel on Climate Change, 2007, Climate change 2007—The physical science basis, *in* Solomon, S., Qin, D., Manning, M., Chen, Z., Marquis, M., Averyt,K.B., Tignor M., and, Miller, H.L., eds.,Contribution of Working Group I to the Fourth Assessment Report of the Intergovernmental Panel on Climate Change: Cambridge University Press, 996 p.

Johnson, S.R., and Richardson, W.J., 1981, Birds, pt. 3 *in* Johnson, S.R., and Richardson, J.W., eds., Beaufort Sea barrier island-lagoon ecological process studies—Final report, Simpson Lagoon: Boulder, Colo., National Oceanic and Atmospheric Administration, Environmental Assessment of the Alaskan Continental Shelf—Final Reports, v. 7, Biological Studies, p. 109–383.

Jorgenson, M.T., and Brown, J., 2005, Classification of the Alaskan Beaufort Sea coast and estimation of carbon and sediment inputs from coastal erosion: Geo-Marine Letters, v. 25, p. 69–80.

Jorgenson, J.C., Joria, P.C., and Douglas, D.C., 2002, Land cover, section 2 in Douglas, D.C., Reynolds, P.E., Rhode, E.B., eds., Arctic Refuge coastal plain terrestrial wildlife research summaries: U.S. Geological Survey, Biological Resources Division, Biological Science Report 2002-0001, p. 4–7, available at https://pubs.er.usgs.gov/publication/bsr20020001.

Jorgenson, T., Marcot, B., 2012, Predicting future habitat changes and habitat use in northwest Alaska: U.S. Geological Survey, Alaska Science Center, presentation for Wildcast Project.

Jorgenson, M.T., Roth, J.E., Pullman, E.R., Burgess, R.M., Raynolds, M.K., Stickney, A.A., Smith, M.D., and Zimmer, T.M., 1996, An ecological land survey for the Colville River Delta, Alaska—Final Report: Fairbanks, Alaska, ABR, Inc., prepared for ARCO Alaska, Inc., and Kuukpik Unit Owners, 160 p.

Kay, J.E., Holland, M.M., and Jahn, A., 2011, Inter-annual to multi-decadal Arctic sea ice extent trends in a warming world: Geophysical Research Letters, v. 38, 6 p., https://doi.org/10.1029/2011GL048008.

Kendall, S.J., 2005, Surveys of breeding birds on Arctic National Wildlife Refuge Beaufort Sea islands, 2003–2004: Fairbanks, Alaska, U.S. Fish and Wildlife Service, Arctic National Wildlife Refuge, 48 p.

Kobayashi, N., Vidrine, J.C,, Nairn, R.B., and Solomon, S.M., 1999, Erosion of frozen cliffs due to storm surge on Beaufort Sea coast: Journal of Coastal Research, v.15, p. 332–344.

Kowalik, Z., 1984, Storm surges in the Beaufort and Chukchi Seas: Journal of Geophysical Research, v.89, C6, p. 10570-10578.

Kraft, J.C., Biggs, R., and Halsey, S., 1973, Morphology and vertical sedimentary sequence models in Holocene transgressive barrier systems, *in* Coates, D.R., ed., Coastal geomorphology: Binghamton, N.Y., State University of New York, p. 321–354.

Kraus, N.C., Millitello, A., and Todoroff, G., 2002, Barrier breaching processes and barrier spit breach, Stone Lagoon, California: Shore and Beach, v. 70, no. 4, p. 21–28.

Kraus, N.C., and Walmsley, T.V., 2003, Coastal barrier breaching—Part 1, Overview of breaching processes: Vicksburg, Miss., U.S. Army Corp of Engineering, Engineer Research and Development Center, Coastal and Hydraulics Laboratory, Coastal and Hydraulics Engineering Technical Note ERDC/CHL CHETN-IV-56, 14 p., available at http://hdl.handle.net/11681/1964.

Large, W.G., and Pond, S., 1981, Open ocean momentum flux measurements in moderate to strong winds: Journal of Physical Oceanography, v. 11, p. 324–336.

Longuet-Higgins, M.S., and Stewart, R.W., 1964, Radiation stresses in water waves; a physical discussion, with applications: Deep-Sea Research, v. 11, p. 529–562.

Lynch, A. H., Clayton, V., Brunner, R.D., 2005, An integrated assessment of the impacts of extreme events on the coastal zone in a small Alaskan community [abs.]: American Meteorological Society Forum, Living in the coastal zone, January 2005.

Lynch, A.H., Lestak, L.R., Uotila, P., Cassano, E.N., and Xie, L., 2007, A factorial analysis of storm surge flooding in Barrow, Alaska: Monthly Weather Review, v. 136, p. 888–912.

Manson, G.K., and Solomon, S.M., 2007, Past and future forcing of Beaufort Sea coastal change: Atmosphere-Ocean, v. 45, p. 107–122, https://doi.org/10.3137/ao.450204.

Marsh, P., Schmidt, T., 1993, Influence of Beaufort Sea storm surge on channel levels in the Mackenzie Delta: Arctic, v. 46, no. 1, p. 35–41.

Martin, P.D., Jenkins, J.L., Adams, F.J., Jorgenson, M.T., Matz, A.C., Payer, D.C., Reynolds, P.E., Tidwell, A.C., and Zelenak, J.R., 2009, Wildlife Response to Environmental Arctic Change—Predicting Future Habitats of Arctic Alaska, Report of the Wildlife Response to Environmental Arctic Change (WildREACH): U.S. Fish and Wildlife Service, Predicting Future Habitats of Arctic Alaska Workshop, Fairbanks, Alaska, November 17–18, 2008, 138 p.

Meehl, G.A., and Hibbard, K., 2007, A strategy for climate change stabilization experiments with AOGCMs and ESMs: Geneva, Switzerland, World Climate Research Programme Informal Report No. 3/2007, ICPO Publication No. 112, IGBP Report No. 57, 36 p.

Mesinger, F., DiMego, G., Kalnay, E., Mitchell, K., Shafran, P.C. , Ebisuzaki, W., Jović, D. , Woollen, J. Rogers, E., Berbery, E.H., Ek, M.B. , Fan, Y., Grumbine, R., Higgins, W., Li, H. , Lin, Y., Manikin, G., Parrish, D., and Shi, W., 2006, North American Regional Reanalysis: Bulletin of the American Meteorological Society, v. 87, p. 343–360.

Milne, G.A., Gehrels, W.R., Hughes, C.W., and Tamisiea, M.E., 2009, Identifying the causes of sea-level change: Nature Geoscience, v. 2, p. 471–478, https://doi.org/10.1038/ngeo544.

Morton, R.A., and Sallenger, A.H., Jr., 2003, Morphological impacts of extreme storms on sandy beaches and barriers: Journal of Coastal Research, v. 19, no. 3, p. 560–573.

Moss, R.H., Edmonds, J.A., Hibbard, K.A., Manning, M.R., Rose, S.K., van Vuuren, D.P., Carter, T.R., Emori, S., Kainuma, M., Kram, T., Meehl, G.A., Mitchell, J.F.B., Nakicenovic, N., Riahi, K., Smith, S.J., Stouffer, R.J., Thomson, A.M., Weyant, J.P., and Wilbanks, T.J., 2010, The next generation of scenarios for climate change research and assessment: Nature, v. 463, p. 747–756.

National Climatic Data Center, 2013, Local Climatological Data (LCD): Tides and Currents web page, accessed January 2013 at http://www.ncdc.noaa.gov/data-access/land-based-station-data/land-based-datasets/quality-controlled-local-climatological-data-qclcd.

National Oceanic and Atmospheric Administration, 2008, Tides and currents: National Oceanic and Atmospheric Administration web page, accessed April 2008 at http://tidesandcurrents.noaa.gov. [Data has since been removed.]

National Oceanic and Atmospheric Administration, 2010, Bathymetry: National Geophysical Data Center web page, accessed June 2010 at http://www.ngdc.noaa.gov/mgg/bathymetry/.

National Oceanic and Atmospheric Administration, 2012, Bathymetry, National Geophysical Data Center database, accessed September 2012 at https://maps.ngdc.noaa.gov/viewers/bathymetry/.

National Oceanic and Atmospheric Administration, 2016, Prudhoe Bay, AK—Station ID 9497645: Tides and currents database, accessed April 2016 at http://tidesandcurrents.noaa.gov/geo.shtml?location=9497645.

National Oceanic and Atmospheric Administration, Earth System Research Laboratory, Physical Sciences Division [now Physical Sciences Laboratory] (NOAA/OAR/ESRL PSD), 2013, NOAA Optimum Interpolation (OI) Sea Surface Temperature (SST) V2: Boulder, Colo., National Oceanic and Atmospheric Administration web page, accessed August 1, 2012 at https://www.esrl.noaa.gov/psd/data/gridded/data.noaa.oisst.v2.html. [Web page moved by time of publication; accessed October 21, 2020 at https://psl.noaa.gov/data/gridded/data.noaa.oisst.v2.html.]

Overeem, I., Anderson, R.S., Cameron, C.W., Clow, G.D., Urban, F.E., and Matell, N., 2011, Sea ice loss enhances wave action at the Arctic coast: Geophysical Research Letters, v. 38, 6 p.

Rabenhorst, M.C., 2005, Biological zero—A soil temperature concept: Wetlands, v. 25, no. 3, p. 616–621.

Rawlinson, S.E., 1993, Surficial geology and morphology of the Alaskan central Arctic Coastal Plain: Fairbanks, Alaska, Alaska Division of Geological and Geophysical Surveys, Report of Investigations 93–1, 72 p.

Rearic, D.M., Barnes, P.W., and Reimnitz, E., 1990, Bulldozing and resuspension of shallow-shelf sediment by ice keels—Implications for Arctic sediment transport trajectories: Marine Geology, v. 91, p. 133–147.

Reimnitz, E., 2000, Interaction of river discharge with sea ice in proximity of Arctic deltas—A review: Polarforschung, v. 70, p. 123–134.

Reimnitz, E., Graves, S.M., and Barnes, P.W., 1988, Beaufort Sea coastal erosion, sediment flux, shoreline evolution, and the erosional shelf profile: U.S. Geological Survey Miscellaneous Investigations Series, Report I-1182-G, 22 p., 1 sheet.

Reimnitz, E., and Kempema, E.W., 1984, Pack ice interaction with Stamukhi Shoal, Beaufort Sea, Alaska, *in* Barnes, P.W., Schell, D.M., and Reimnitz, E., eds., The Alaskan Beaufort Sea—Ecosystems and Environments: Orlando, Fla., Academic Press, p. 159–183.

Reimnitz, E., and Maurer, D.K., 1979, Effects of Storm Surges on the Beaufort Sea Coast, Northern Alaska: Arctic, v. 32, no. 4, p. 329–344.

Roelvink, D., Reniers, A., van Dongeren, A., van Thiel de Vries, J., McCall, R., and Lescinski, J., 2009, Modelling storm impacts on beaches, dunes and barrier islands: Coastal Engineering, v. 56, no. 11, p. 1133–1152.

Shuttleworth, W.J., 1993, Putting the 'vap' into evaporation: Hydrology and Earth System Sciences, v. 11, no. 1, p. 210–244,

Soulsby, R., 1997, Dynamics of Marine Sands: London, Thomas Telford Publications, 245 p.

Stockdon, H.F., Holman, R.A., Howd, P.A., and Sallenger, A.H., Jr., 2006, Empirical parameterization of setup, swash, and runup: Coastal Engineering, v. 53, no. 7, p. 573–588.

Stroeve, J., Holland, M.M., Meier, W., Scambos, T., and Serreze, M., 2007, Arctic sea ice decline—Faster than forecast: Geophysical Research Letters, v. 34, 5 p.

Stroeve, J.C., Kattsov, V., Barrett, A., Serreze, M., Pavlova, T., Holland, M., and Meier, W.N., 2012, Trends in Arctic sea ice extent from CMIP5, CMIP3 and observations: Geophysical Research Letters, v. 39, 7 p.

Stutz, M.L., and Pilkey, O.H., 2011, Open-ocean barrier islands—Global influence of climatic, oceanographic, and depositional settings: Journal of Coastal Research, v. 27, no. 2, p. 207–222.

Sultan, N.J., Braun, K.W., and Thieman, D.S., 2011, North slope trends in sea level, storm frequency, duration and intensity: Ice Tech Conference, Prudhoe Bay, Alaska, Paper No. ICETECH10-155-R0, 6 p.

Swail, V.R., Cardone, V.J., Callahan, B., Ferguson, M., Gummer, D.J., and Cox, A.T., 2007, The MSC Beaufort wind and wave reanalysis, in International Workshop on Wave Hindcasting and Forecasting and Coastal Hazard Symposium, 10th, North Shore, Oahu, Hawaii, 2007, Proceedings: Wave Workshop, 22 p.

Tape, K.D., Flint, P.L., Meixell, B.W., and Gagliooti, B.V., 2013, Inundation, sedimentation, and subsidence creates goose habitat along the Arctic coast of Alaska: Environmental Research Letters, v. 8, no. 4, 9 p.

Taylor, K.E., Stouffer, R.J., and Meehl, G.A., 2012, An overview of CMIP5 and the experiment design: Bulletin of the American Meteorological Society, v. 93, no. 4, p. 485–498.

Thieler, E.R., Himmelstoss, E.A., Zichichi, J.L., and Ergul, A., 2009, Digital Shoreline Analysis System (DSAS) version 4.0—An ArcGIS extension for calculating shoreline change: U.S. Geological Survey Open-File Report 2008–1278, accessed March 15, 2013, at https://pubs.er.usgs.gov/publication/ofr20081278.

Tolman, H.L., 1999, User manual and system documentation of WAVEWATCH III (ver. 1.18): Washington, D.C., National Oceanic and Atmospheric Administration, National Centers for Environmental Prediction, 112 p.

Truett, J.C., 1984, Environmental characterization and biological use of lagoons in the eastern Beaufort Sea, Final Report: Outer Continental Shelf Environmental Assessment Program, p. 1–20.

U.S. Fish and Wildlife Service, 2012, Endangered Species: U.S. Fish and Wildlife Service Endangered Species Program web page, accessed March 15, 2013 at http://www.fws.gov/endangered/.

van Vuuren, D.P., Edmonds, J., Kainuma, M., Riahi, K., Thomson, A., Hibbard, K., Hurtt, G.C., Kram, T., Krey, V., Lamarque, J.-F., Masui, T., Meinshausen, M., Nakicenovic, N., Smith, S.J., and Rose, S.K., 2011, The representative concentration pathways—An overview: Climatic Change, v. 109, p. 5–31.

Viereck, L.A., Dyrness, C.T., Batten, A.R., and Wenzlick, K.J., 1992, The Alaska vegetation classification: US Department of Agriculture, Forest Service, General Technical Report PNW-GTR-286.

Wang, M., and Overland, J.E., 2015, Projected future duration of the sea-ice-free season in the Alaskan Arctic: Progress in Oceanography, v. 136, p. 50–59.

Weijers, S., Wagner-Cremer, F., Sass-Klaassen, U., Broekman, R., and Rozema, J., 2013, Reconstructing high arctic growing season intensity from shoot length growth of a dwarf shrub: The Holocene, v. 23, no. 5, p. 721–731.

Wilby, F.B., Young, G.R., Cunningham, C.H., Lieber, A.C., Jr., Hale, R.K., Saville, T., and O'Brien, M.P., 1939, Inspection of beaches in path of the hurricane of 21 September 1938: Shore and Beach, v. 7, p. 43–47.

Williams, J., Higginson, J.J., Rohrbough, J.D., 1973, Sea and air—The marine environment (2d ed.): Annapolis, Md., Naval Institute Press, 338 p.

Wise, J.L., Comiskey, A.L., and Becker, R., 1981, Storm surge climatology and forecasting in Alaska: Anchorage, Alaska, University of Alaska, Arctic Environmental Information and Data Center.

Wiseman, W.J., Jr., Coleman, J.M., Gregory, A., Hsu, S.A., Short, A.D., Suhayda, J.N., Walters, C.D., Jr., and Wright, L.D., 1973, Alaskan Arctic coastal processes and morphology: Baton Rouge, La., Louisiana State University, Coastal Studies Institute Technical Report No. 149, 171 p.

World Climate Research Programme, 2011, CMIP5–Coupled Model Intercomparison Project Phase 5, Overview: Lawrence Livermore National Laboratory web page, accessed December 2011, at http://cmip-pcmdi.llnl.gov/cmip5/.

Yin, J., 2012, Century to multi-century sea-level rise projections from CMIP5 models: Geophysical Research Letters, v. 39, no. 17, 7 p. https://doi.org/10.1029/2012GL052947.

Appendix 1. Documented historical and model hind-cast storm events in the vicinity of Arey Island and Lagoon

Table 1.1. Documented historical storm events in the vicinity of Arey Island and Lagoon.

[m, meter; m/s, meter per second; km/h, kilometer per hour; s, second; TWL, total water level; MSL, mean sea level]

Dates	Location	Impact	Source	Comments
1905	Mackenzie Delta	-	Reimnitz and Maurer, 1979	
1928/1929	Simpson Lagoon and Mackenzie Delta	-	Reimnitz and Maurer, 1979	Two dates found, probably same event
Sep. 09, 1940/1944	Beaufort Sea and Mackenzie Delta	-	Reimnitz and Maurer, 1979	Two dates found, probably same event
Sep. 1944 and 1970	Tuktoyaktuk	3 m TWL at Tuktoyaktuk	Henry and Heaps, 1976	First account of storm surge at this location
Oct. 3–4, 1963	Barrow and Tuktoyaktuk (Canada)	3 m TWL in Barrow	Kowalik, 1984	Largest storm surge observed in Barrow (as of 1984), tracked eastward
Fall 1970	Across Beaufort Sea coast - including Harrison Bay to Mackenzie Bay	3 m TWL in Tuktoyaktuk	Reimnitz and Maurer, 1979	Tracked driftwood debris in Tuktoyaktuk, winds up to 40–50 m/s, surge observed everywhere except vicinity to Barrow
Aug. 30–Sep 3, 1972	Pelly Island, Atkinson Pt, Cape Delhousie, Cape Bathurst	-	Henry and Heaps, 1976	Recorded on temporary tide gages, more modest than 1970 storm
Nov. 9–14, 1973	Canada - Tuktoyaktuk and Herschel Island	0.8 m TWL Herschel, 1 m TWL Tuktoyaktuk	Henry and Heaps, 1976	Recorded on temporary tide gages
Jan. 4–8, 1974	Canada - Tuktoyaktuk and Herschel Island	1 m TWL Herschel, 1 m TWL Tuktoyaktuk	Henry and Heaps, 1976	Recorded on temporary tide gages
Aug. 30–Sep. 1, 1981	Eastern Beaufort Sea	0.6 m TWL Canada, mixed in W. Beaufort Sea	Kowalik, 1984	Low-pressure system moving south along Canadian Islands from high latitudes, strong NW winds up to 40 knots
Sep. 15–18, 1985	Tuktoyaktuk	1.73 m TWL with 1.38 m surge Tuktoyaktuk	Marsh and Schmidt, 1993	Based on tide record from Tuktoyaktuk, 180° shift in wind direction and 56 km/h peak wind
Aug, 1986	Tuktoyaktuk	1.6 m surge Tuktoyaktuk, 1.4 N and W of Tuktoyaktuk	Harper and others, 1988	Measured from tide gages
Sep, 1986	Barter Island	Submerged Barter airport runway	Stankiewicz, North Slope Borough Risk Management Division, oral commun.	Runway sees annual flooding as a result of storms
Sep. 1993	Tuktoyaktuk	2 m surge at Tuktoyaktuk	Kobayashi and others, 1999	Cliff retreat at North Head and Tuktoyaktuk, duration 100 hours, wave height 1 m, spectral peak period 7 s
Sep. 30, 1993	Prudhoe Bay	1.00 m above MSL	NOAA tide gauge time-series data (tidesandcurrents.noaa.gov/pub.html)	Top 10 events recorded by Prudhoe Bay tide gage, 1993–2017

Table 1.1.—Continued

Dates	Location	Impact	Source	Comments
Aug. 10–11, 2000	Barrow, Prudhoe Bay	1.47 m storm surge Prudhoe Bay	Lynch and others, 2005, 2007	Storm tracked eastward from off the coast of the Siberian Peninsula, dissipated before reaching the Canadian Archipelago
Aug. 11, 2000	Prudhoe Bay	1.37 m above MSL	NOAA tide gauge time-series data (tidesandcurrents.noaa.gov/pub.html)	Top 10 events recorded by Prudhoe Bay tide gage, 1993–2017
Aug. 15, 2002	Prudhoe Bay	1.12 m above MSL	NOAA tide gauge time-series data (tidesandcurrents.noaa.gov/pub.html)	Top 10 events recorded by Prudhoe Bay tide gage, 1993–2017
Oct. 09, 2002	Prudhoe Bay	1.15 m above MSL	NOAA tide gauge time-series data (tidesandcurrents.noaa.gov/pub.html)	Top 10 events recorded by Prudhoe Bay tide gage, 1993–2017
Jul. 30, 2003	Prudhoe Bay	1.26 m above MSL	NOAA tide gauge time-series data (tidesandcurrents.noaa.gov/pub.html)	Top 10 events recorded by Prudhoe Bay tide gage, 1993–2017
Aug. 05, 2003	Prudhoe Bay	1.04 m above MSL	NOAA tide gauge time-series data (tidesandcurrents.noaa.gov/pub.html)	Top 10 events recorded by Prudhoe Bay tide gage, 1993–2017
Jul. 31, 2008	Prudhoe Bay	1.12 m above MSL	NOAA tide gauge time-series data (tidesandcurrents.noaa.gov/pub.html)	Top 10 events recorded by Prudhoe Bay tide gage, 1993–2017
Feb. 26, 2011	Prudhoe Bay	1.05 m above MSL	NOAA tide gauge time-series data (tidesandcurrents.noaa.gov/pub.html)	Top 10 events recorded by Prudhoe Bay tide gage, 1993–2017
Nov. 11, 2013	Prudhoe Bay	1.00 m above MSL	NOAA tide gauge time-series data (tidesandcurrents.noaa.gov/pub.html)	Top 10 events recorded by Prudhoe Bay tide gage, 1993–2017
Jul. 18, 2016	Prudhoe Bay	1.02 m above MSL	NOAA tide gauge time-series data (tidesandcurrents.noaa.gov/pub.html)	Top 10 events recorded by Prudhoe Bay tide gage, 1993–2017

Table 1.2. Model hindcast storm events (1981–2010) in Arey Lagoon.

[UTC, coordinated universal time; H_s, significant wave height; D_p, peak direction; T_p, peak period; m, meter; deg, degree; s, second]

Store date (UTC)	H_s (m)	D_p (deg)	T_p (s)	Storm surge (m)
August 30, 1981	2.1	235	7.4	0.21
September 18, 1985	1.3	215	8.3	0.37
September 22, 1985	3.5	305	9.5	0.36
September 22, 1986	1.3	215	8.3	0.53
August 26, 1987	2.5	315	7.4	0.64
August 29, 1987	3.7	295	9.5	0.64
September 1, 1987	3.2	305	8.3	0.59
October 16, 1987	1.7	225	8.3	0.33
September 16, 1993	1.9	225	8.3	0.64
September 24, 1993	1.3	215	8.3	0.52
September 28, 1993	2.3	325	7.4	0.52
October 2, 1993	3.7	235	10.7	0.28
September 23, 1998	1.3	325	6.5	0.32
October 19, 1998	1.4	245	8.3	0.28
October 26, 1998	3.7	235	10.7	0.32
August 8, 1999	0.9	215	5.1	0.38
August 25, 1999	1.5	225	7.4	0.60
September 2, 1999	1.6	325	6.5	0.62
September 7, 1999	0.8	325	5.7	0.62
September 24, 1999	3.2	305	9.5	1.28
September 27, 1999	3.2	305	9.5	1.28
September 29, 1999	2.0	315	7.4	0.63
August 13, 2000	2.9	315	8.3	1.22
September 20, 2000	2.2	325	7.4	0.60
September 28, 2001	3.3	235	8.3	0.60
August 16, 2002	3.3	305	8.3	0.95
October 5, 2002	3.1	315	8.3	1.04
October 7, 2002	3.8	305	9.5	1.06
October 11, 2002	2.8	305	8.3	1.06
September 28, 2003	3.2	315	8.3	0.98
September 22, 2005	3.5	235	10.7	0.18
September 16, 2006	2.3	225	8.3	0.77
September 27, 2006	3.7	235	10.7	0.33
October 10, 2006	4.0	235	12.1	0.80
October 18, 2006	3.0	235	9.5	0.40
September 9, 2007	2.5	225	9.5	0.30
September 14, 2007	3.4	235	10.7	0.28
September 23, 2007	3.2	235	10.7	0.19
October 20, 2007	2.1	235	9.5	0.24
November 1, 2007	3.7	235	10.7	0.28
August 1, 2008	3.8	305	9.5	0.71
September 20, 2008	1.3	215	6.5	0.59
October 5, 2008	3.0	235	8.3	0.91
October 8, 2008	3.7	305	9.5	0.91
August 19, 2010	2.9	225	9.5	0.29
October 6, 2010	3.6	235	10.7	0.49

References Cited

Harper, J.R., Henry, R.F., and Stewart, G.G., 1988, Maximum storm surge elevations in the Tuktoyaktuk Region of the Canadian Beaufort Sea: Arctic, v. 41, no. 1, p. 48–52.

Henry, R.F., and Heaps, N.S., 1976, Storm surge in the southern Beaufort Sea: Journal of the Fisheries Research Board of Canada, v. 33, no. 10, p. 2362–2376.

Kobayashi, N., Vidrine, J.C., Nairn, R.B., and Solomon, S.M., 1999, Erosion of frozen cliffs due to storm surge on Beaufort Sea coast: Journal of Coastal Research, v.15, p. 332–344.

Kowalik, Z., 1984, Storm surges in the Beaufort and Chukchi Seas: Journal of Geophysical Research, v.89, C6, p. 10,570-10,578.

Lynch, A. H., Clayton, V., Brunner, R.D., 2005, An integrated assessment of the impacts of extreme events on the coastal zone in a small Alaskan community [abs.]: American Meteorological Society Forum, Living in the coastal zone, January 2005.

Lynch, A.H., Lestak, L.R., Uotila, P., Cassano, E.N., and Xie, L., 2007, A factorial analysis of storm surge flooding in Barrow, Alaska: Monthly Weather Review, v. 136, p. 888–912.

Marsh, P., Schmidt, T., 1993, Influence of Beaufort Sea storm surge on channel levels in the Mackenzie Delta: Arctic, v. 46, no. 1, p. 35–41.

Reimnitz, E., and Maurer, D.K., 1979, Effects of Storm Surges on the Beaufort Sea Coast, Northern Alaska: Arctic, v. 32, no. 4, p. 329–344.

Appendix 2. Model Settings

Delft3D Settings

```
[SedimentFileInformation]
   FileCreatedBy    = Delft3D FLOW-GUI, Version: 3.42.00.17790
   FileCreationDate = Wed Feb 13 2013, 15:43:59
   FileVersion      = 02.00
[SedimentOverall]
   Cref             =  1.6000000e+003      [kg/m3]  CSoil Reference density for hindered settling calculations
   IopSus           = 0                             If Iopsus = 1: susp. sediment size depends on local flow and wave conditions
[Sediment]
   Name             = #Sediment1#                   Name of sediment fraction
   SedTyp           = sand                          Must be "sand", "mud" or "bedload"
   RhoSol           =  2.6500000e+003      [kg/m3]  Specific density
   SedDia           =  3.0000000e-004      [m]      Median sediment diameter (D50)
   CDryB            =  1.6000000e+003      [kg/m3]  Dry bed density
   IniSedThick      =  5.0000000e+000      [m]      Initial sediment layer thickness at bed (uniform value or filename)
   FacDSS           =  1.0000000e+000      [-]      FacDss * SedDia = Initial suspended sediment diameter. Range [0.6 - 1.0]
```

```
[MorphologyFileInformation]
   FileCreatedBy    = Delft3D FLOW-GUI, Version: 3.42.00.17790
   FileCreationDate = Wed Feb 13 2013, 15:40:49
   FileVersion      = 02.00
[Morphology]
   EpsPar           = false                         Vertical mixing distribution according to van Rijn (overrules k-epsilon model)
   IopKCW           = 1                             Flag for determining Rc and Rw
   RDC              = 0.01                 [m]      Current related roughness height (only used if IopKCW <> 1)
   RDW              = 0.02                 [m]      Wave related roughness height (only used if IopKCW <> 1)
   MorFac           =  1.0000000e+002      [-]      Morphological scale factor
   MorStt           =  6.0000000e+001      [min]    Spin-up interval from TStart till start of morphological changes
   Thresh           =  5.0000001e-002      [m]      Threshold sediment thickness for transport and erosion reduction
   MorUpd           = true                          Update bathymetry during FLOW simulation
   EqmBc            = true                          Equilibrium sand concentration profile at inflow boundaries
   DensIn           = false                         Include effect of sediment concentration on fluid density
   AksFac           =  1.0000000e+000      [-]      van Rijn's reference height = AKSFAC * KS
   RWave            =  2.0000000e+000      [-]      Wave related roughness = RWAVE * estimated ripple height. Van Rijn Recommends rang
   AlfaBs           =  1.0000000e+000      [-]      Streamwise bed gradient factor for bed load transport
   AlfaBn           =  1.5000000e+000      [-]      Transverse bed gradient factor for bed load transport
   Sus              =  1.0000000e+000      [-]      Multiplication factor for suspended sediment reference concentration
   Bed              =  1.0000000e+000      [-]      Multiplication factor for bed-load transport vector magnitude
   SusW             =  1.0000000e+000      [-]      Wave-related suspended sed. transport factor
   BedW             =  1.0000000e+000      [-]      Wave-related bed-load sed. transport factor
   SedThr           =  1.0000000e-001      [m]      Minimum water depth for sediment computations
   ThetSD           =  0.0000000e+000      [-]      Factor for erosion of adjacent dry cells
   HMaxTH           =  1.5000000e+000      [m]      Max depth for variable THETSD. Set < SEDTHR to use global value only
   FWFac            =  1.0000000e+000      [-]      Vertical mixing distribution according to van Rijn (overrules k-epsilon model)
```

```
Ag     =  9.8300000e+000
Rhow   =  1.0250000e+003
Tempw  =  1.5000000e+001
Salw   =  3.1000000e+001
Wstres =  2.8000000e-003
Rhoa   =  1.0000000e+000
Betac  =  5.0000000e-001
Equili = #N#
Ktemp  = 0
Fclou  =  0.0000000e+000
Sarea  =  0.0000000e+000
Temint = #Y#
Commnt =
Roumet = #C#
Ccofu  =  6.5000000e+001
Ccofv  =  6.5000000e+001
Xlo    =  0.0000000e+000
Vicouv =  1.0000000e+000
Dicouv =  1.0000000e+001
Htur2d = #N#
Irov   = 0
```

```
Commnt =
Iter   =      2
Dryflp = #YES#
Dpsopt = #MAX#
Dpuopt = #MEAN#
Dryflc =  1.0000000e-001
Dco    = -9.9900000e+002
Tlfsmo =  6.0000000e+001
ThetQH =  0.0000000e+000
Forfuv = #Y#
Forfww = #N#
Sigcor = #N#
Trasol = #Cyclic-method#
```

SWAN / WAVE settings

```
[Constants]
   WaterLevelCorrection =  0.0000000e+000
   Gravity              =  9.8299999e+000
   WaterDensity         =  1.0250000e+003
   NorthDir             =  9.0000000e+001
   MinimumDepth         =  5.0000001e-002
[Processes]
   GenModePhys          = 3
   Breaking             = true
   BreakAlpha           =  1.0000000e+000
   BreakGamma           =  7.3000002e-001
   Triads               = false
   TriadsAlpha          =  1.0000000e-001
   TriadsBeta           =  2.2000000e+000
   WaveSetup            = true
   BedFriction          = jonswap
   BedFricCoef          =  6.7000002e-002
   Diffraction          = false
   DiffracCoef          =  2.0000000e-001
   DiffracSteps         = 5
   DiffracProp          = true
   WindGrowth           = false
   WhiteCapping         = Komen
   Quadruplets          = false
   Refraction           = true
   FreqShift            = true
   WaveForces           = radiation stresses
[Numerics]
   DirSpaceCDD          =  5.0000000e-001
   FreqSpaceCSS         =  5.0000000e-001
   RChHsTm01            =  2.0000000e-002
   RChMeanHs            =  2.0000000e-002
   RChMeanTm01          =  2.0000000e-002
   PercWet              =  9.8000000e+001
   MaxIter              = 15
```

```
[Domain]
   Grid                 = swan2.grd
   BedLevel             = swan2.dep
   DirSpace             = circle
   NDir                 = 36
   StartDir             =  0.0000000e+000
   EndDir               =  0.0000000e+000
   FreqMin              =  5.0000001e-002
   FreqMax              =  1.0000000e+000
   NFreq                = 24
   NestedInDomain       = 1
   Output               = true
[Boundary]
   Name                 = west
   Definition           = orientation
   Orientation          = west
   SpectrumSpec         = parametric
   SpShapeType          = jonswap
   PeriodType           = peak
   DirSpreadType        = power
   PeakEnhanceFac       =  3.3000000e+000
   GaussSpread          =  9.9999998e-003
   WaveHeight           =  3.0000000e+000
   Period               =  9.0000000e+000
   Direction            =  6.1000000e+001
   DirSpreading         =  4.0000000e+000
```

WW3 Settings

Grid name: NWW3 global 1x1.25 degr.

Spectral discretization:

Number of directions : 24
Directional increment (deg.): 15.0
First direction (deg.): 0.0
Number of frequencies : 25
Frequency range (Hz) : 0.0418-0.4114
Increment factor : 1.100

XBEACH Settings

```
Grid input

nx       = 654
ny       = 0
xfile    = x.grd
yfile    = y.grd
xori     = 391045.27
yori     = 7783666.2
alfa     = 258.6987
depfile  = transect22.dep
posdwn    = -1
thetanaut = 0
thetamin  = -90
thetamax  = 90
dtheta    = 10
vardx     = 1
-----------------------------------
Numerics input
CFL      = 0.9
eps      = 0.01
-----------------------------------
Time input
tstart   = 0.
tstop    = 197400
taper    = 100
tintg    = 3600
tintm    = 3600
tintp    = 60
-----------------------------------
General constants
rho      = 1025
g        = 9.83
-----------------------------------
Boundary condition options
zs0file  = tide.txt
tideloc  = 1
instat   = 41
tidelen = 330
-----------------------------------
```

```
-----------------------------------
Wave calculation options
break    = 3
bcfile   = jonswap1.txt
-----------------------------------
Flow calculation options
order    = 2
C        = 65.
nuh      = 0.01
nuhfac   = 1.0
lat    = 70.5


-----------------------------------------
Sediment transport calculation options
form     = 1
D50      = 0.0004
lws      = 0
turb     = 2
ne_layer = sedlayer.dep
-----------------------------------------
Morphological calculation options
morfac   = 10
struct   = 1
-----------------------------------------
```

Appendix 3. Field Data

Field Data

This appendix describes the methods used in the collection of field data and presents data collected from July 7 through September 27, 2011 (U.S. Geological Survey [USGS] Coastal and Marine Geology Infobank FACS IDs: I-D4-11-AR and I-R4-11-AR) and bathymetric data and samples collected in summer of 2010 (USGS FACS ID: L-6-10-AK). Data are available for download via USGS data release (Erikson and others, 2020, https://doi.org/10.5066/P9LGYO2Q). Physical measurements and sampling were made throughout the Arey Lagoon study area to characterize the environment and support modeling efforts. In addition to meeting the needs of this project, the measurements provide basic physical background and baseline data in this area where such information is very sparse or entirely lacking. Two on-land focus sites (fig. 3.1) were established: one on Arey Barrier Island (Arey Island) and a second one consisting of a wet sedge habitat on the mainland coast. Both sites were equipped with time-lapse cameras, thermistor arrays, and instruments to measure conductivity, temperature, and depth (CTDs). Two monitoring sites with seabed mounted instrument packages were also established to measure lagoon and oceanographic conditions.

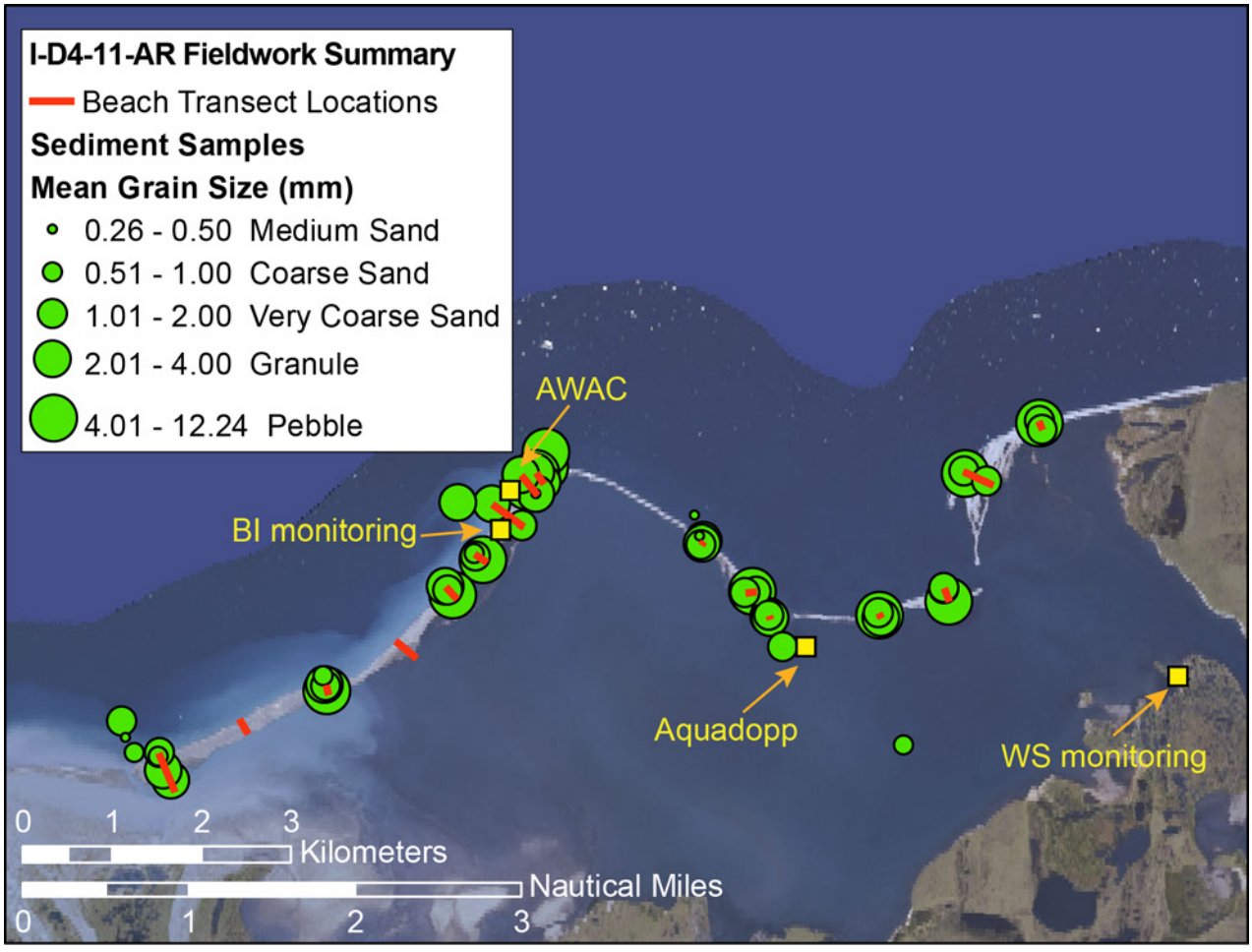

Background image courtesy UAF-GINA (http://alaskamapped.org/bdl); includes material © CNES 2011, Distribution Spot Image S.A., France, SICORP, USA, all rights reserved

Figure 3.1. Map showing locations of instrument deployments, cross-shore transects, focus site monitoring stations, and sediment samples collected in July 2011 around Arey Island and Lagoon, Alaska. Instrument packages were placed on the seabed at the AWAC and Aquadopp sites. The barrier island (BI) and wet sedge (WS) monitoring sites were equipped with time-lapse cameras, thermistor arrays, and a CTD (conductivity, temperature, and depth) monitor. Circles represent sediment sample locations showing approximate mean grain size with values ranging from medium sand (0.26 millimeters [mm]) to pebbles (12.24 mm).

Methods

The field data can be classified as two types: individual time-stamp point measurements and time-series observations. Methods and specifics of sampling protocols are summarized below. All reported times are UTC (Alaska Standard time plus 9 hours).

Point Measurements

Point measurements include bathymetric and terrestrial elevation measurements, surface sediment grab samples, and salinity measurements within the wet sedge focus study site and nearby ponds. Bathymetry was measured within the lagoon and on the seaward side of the barrier islands and on western Barter Island (fig. 3.2) using one of three systems: a Hummingbird 898 SI fishfinder with integrated GPS, an Ohmex Sonarmite BT integrated with a Trimble GeoHX series GPS, or a Garmin Sounder with integrated GPS. Each system collected single-beam water depth with accuracies better than 4 meters (m) horizontal and 25 centimeters (cm) vertical. Depth data were recorded at 1 Hz and referenced to approximate mean sea level (aMSL) using three months of water-level measurements obtained with the Aquadopp and AWAC instruments (see next section). For shallow areas within the lagoon, a small dinghy with a draft of <0.5 m was equipped with the Ohmex Sonarmite; however, even with this low draft, measurements were not possible in the western part of Arey Lagoon owing to the very shallow water depths. Because the substrate was composed primarily of silt, making it unsafe for walking across, it was not possible to obtain depth measurements in this area.

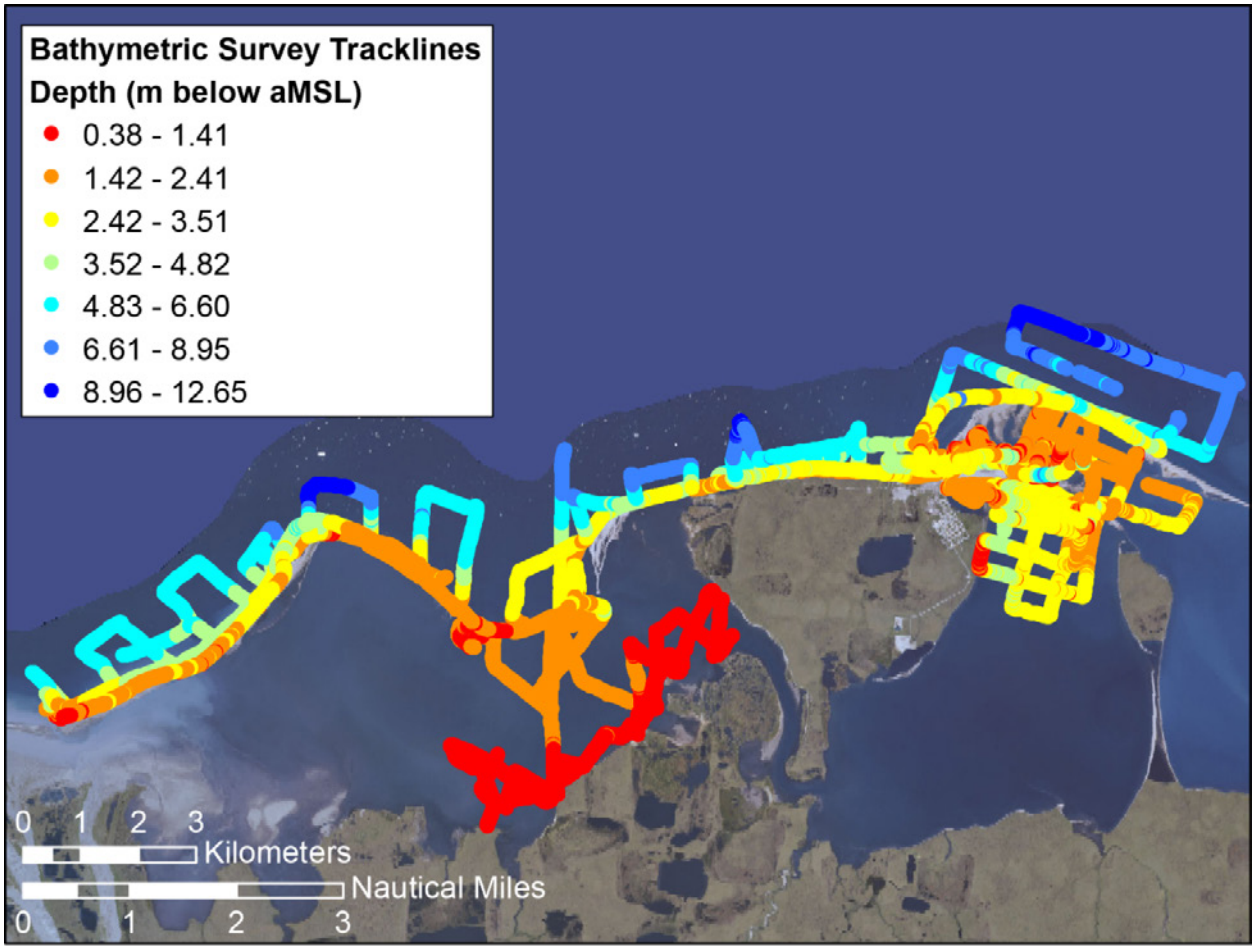

Figure 3.2. Map of Arey Lagoon, Barter Island, and vicinity, Alaska, showing bathymetric tracklines and color-coded water depths for data collected in 2010 and 2011. m, meter; aMSL, approximate mean sea level.

Terrestrial elevation surveys (topography) were obtained with two Ashtech® ZXtreme roving global positioning system (GPS) units in a backpack configuration. A base station using a third ZXtreme was established on Barter Island for the duration of the field campaign. Rover data were corrected to within 0.20 m accuracy using post-processed measurements from the base station. Shoreline position (wet-dry line along beach) and elevations along shore-normal transects across Arey Island (fig. 3.3) were mapped using the backpack GPS system. High-resolution (nominal 2-m point density, interpolated to a 4-m spatial grid) elevation data, obtained with the airborne light detection and ranging (lidar) and collected as part of the USGS National Shoreline Assessment Project (Gibbs and Richmond, 2015), were merged with the bathymetry obtained as part of this study to derive a complete digital topo-bathy elevation model (DEM) of the study area.

A total of 43 terrestrial sediment grab samples were collected for grain size analysis on the barrier island (Arey Island east and west) separating the Beaufort Sea and Arey Lagoon (fig. 3.1). Samples were collected at the water lines of the Beaufort Sea and Arey Lagoon shorelines as well as at the crest or berm of the barrier along 14 shore-normal transects across Arey Island and 2 transects from the western end of the barrier spit that extends westward from Barter Island. Of the 43 surface sediment samples, 6 were collected on the western spit of Barter Island, 9 were collected from Arey Island east, and 28 were collected from Arey Island west. In addition, 11 seabed samples were collected using a small pipe dredge in the vicinity of oceanographic instrument package deployments and on the ocean side of Arey Island. Two grab samples were sieved and analyzed for grain size distributions. Mean grain sizes of remaining samples were determined from referenced photographs of collected samples taken in the lab (Barnard and others, 2007) using two-dimensional spectral decomposition of sediment images (Buscombe and others, 2010). Results of sieved samples were used for verification of mean grain size values obtained with the image processing algorithm.

Pond temperatures and salinity (conductivity) were measured along two transects traversing the wet sedge study area. A hand-held YSI 556 MPS (±0.5 percent accuracy) with a cable-attached instrument probe was placed in 10–15 cm of water within 1 m of each of the pond edges and allowed to equilibrate, and readings were recorded manually. In all, 35 ponds were sampled over a distance of ~1.5 km.

Time-series Measurements

Nearly three months of time-series measurements were obtained at two locations during the latter part (12 July to 26 September) of the 2011 open-water season. Wave height and period, current speed and direction, pressure (water level), conductivity (salinity), and temperature were measured on both the open-ocean and lagoon sides of Arey Island (fig. 3.1; table 3.1). The instrument package at the lagoon site was deployed in a mean water depth of 1.2 m and consisted of a 1 MHz Nortek Aquadopp and a Solinst Levelogger Model 3001 attached to a weighted galvanized cross-frame. A Hobo pendant and surface floats were tethered to the frame to allow for upper water column temperature measurements. A similar

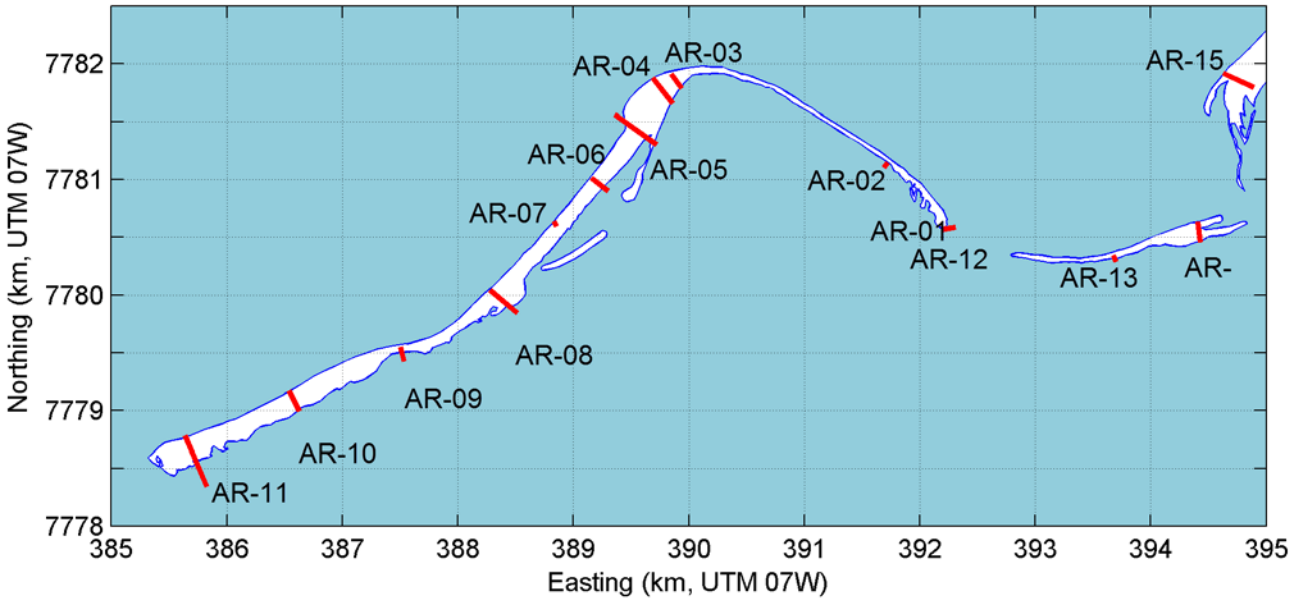

Figure 3.3. Map of Arey Island, Alaska, showing transects where elevation data were measured with a backpack Global Positioning System (GPS). km, kilometer; UTM 07W, universal transverse Mercator.

instrument package, using instead a 1 MHz Nortek AWAC, was placed on the seabed in about 5-m water depth on the open-ocean side of Arey Island to measure waves and currents. For wave measurements, an AWAC is superior to the Aquadopp in that it records two-dimensional wave spectra, allowing for robust determination of incident wave direction.

Time-series of active layer ground temperatures were measured at the wet sedge and barrier island focus study sites (table 3.2). Two types of thermistor arrays were used. A total of 12 nickel-sized Embedded Data System iButton Thermocron (Model DS1921G-F5#) temperature data loggers were placed in 3-cm-diameter PVC pipes and separated with native sediment at intervals of 10 to 20 cm. The PVC pipes, with embedded thermocron arrays, were inserted vertically into the ground at the ocean and lagoon sides of the barrier island along transect AR-05. The Thermocrons have a reported manufacture range of 40 to 85 °C and resolution of 0.5 °C. The iButton Thermocrons offer a low-cost simple method for collecting temperatures, but they can only be used until their memory reaches capacity.

Table 3.1. Time-series measurements by oceanographic instrument deployment.

[UTC, coordinated universal time; AST, acoustic surface tracking; puv, pressure and velocity; m, meter; Hz, hertz; MHz, megahertz; min, minute; s, second; avg, average. Locations are lat./long. in decimal degrees]

Parameter	Instrumentation	Settings & comments
Open ocean deployment		
Location: 70.11687° N. / 143.92597° W.	Mean depth:4.7 m	Dates (UTC): 7/12/2011–9/26/2011
Currents	Nortek 1.2 MHz AWAC	1 Hz; 30 min avg; 0.25 m bins
Waves	ditto	AST; 2D spectral wave
Pressure (water level)	AWAC & Solinst	30 min
Near-seabed water temperatures	AWAC & Solinst	30 min
Surface water temperatures	Hobo pendant	30 min
Near-seabed conductivity	Solinst Levelogger 3001	10 s
Lagoon deployment		
Location: 70.10413° N. / 143.82839° W.	Mean depth: 1.2 m	Dates (UTC): 7/12/2011–9/26/2011
Currents	Nortek 1MHz Aquadopp	1 Hz; 30 min avg; 0.25 m bins
Waves	Nortek 1MHz Aquadopp	puv method
Pressure (water level)	Aquadopp & Solinst	30 min
Near-seabed water temperatures	Aquadopp & Solinst	30 min
Surface water temperatures	Hobo pendant	30 min
Near-seabed salinity	Solinst Levelogger 3001	10 s

Table 3.2. Time-series measurements at the barrier island and wet sedge focus study sites surrounding Arey Lagoon, Alaska.

[h, hour]

Parameter	Instrumentation	Location (lat./long. in decimal degrees)	Settings
	Barrier island focus site	Dates: 7/16/2011–7/20/2011	
Time-lapse camera	Moultrie game camera	70.10060° N./ 143.71501° W.	1 photo/h
Ground temp. array—ocean side	iButton thermocrons	70.11190° N./ 143.92030° W.	1 sample/h
Ground temp. array—lagoon side	iButton thermocrons	70.11128° N./ 143.91774° W.	1 sample/h
	Wet sedge focus site	Dates: 7/9/2011–7/21/2011	
Time-lapse camera	Moultrie game camera	70.10060° N./ 143.71501° W.	1 photo/h
Ground temp. array—swash	EDS thermocrons	70.10072° N./ 143.71484° W.	
Near-seabed water temps	Solinst Levelogger M3100	70.10068° N./ 143.71477° W.	
Near-seabed salinity	ditto	ditto	
Pressure (water level)	ditto	ditto	

Low-cost autonomous time-lapse cameras (Moultrie Game Cameras) were installed at focus study sites, and still images were taken every hour. The cameras were installed with the intent of providing visual evidence of nearshore processes including any potential overwash of the barrier island or marsh flooding. The cameras at the barrier island and wet sedge bluff study sites offered limited data as the barrier island camera toppled over and the marsh camera ceased working in mid-August.

Summary of Data Observations

Bathymetric and Topographic Mapping

Bathymetric and topographic measurements, combined with airborne lidar elevation data (Gibbs and Richmond, 2015), were used to generate a complete digital elevation model (DEM) of the study area (fig. 3.4*A*). The DEM was used to model storm surge and wave propagation from the

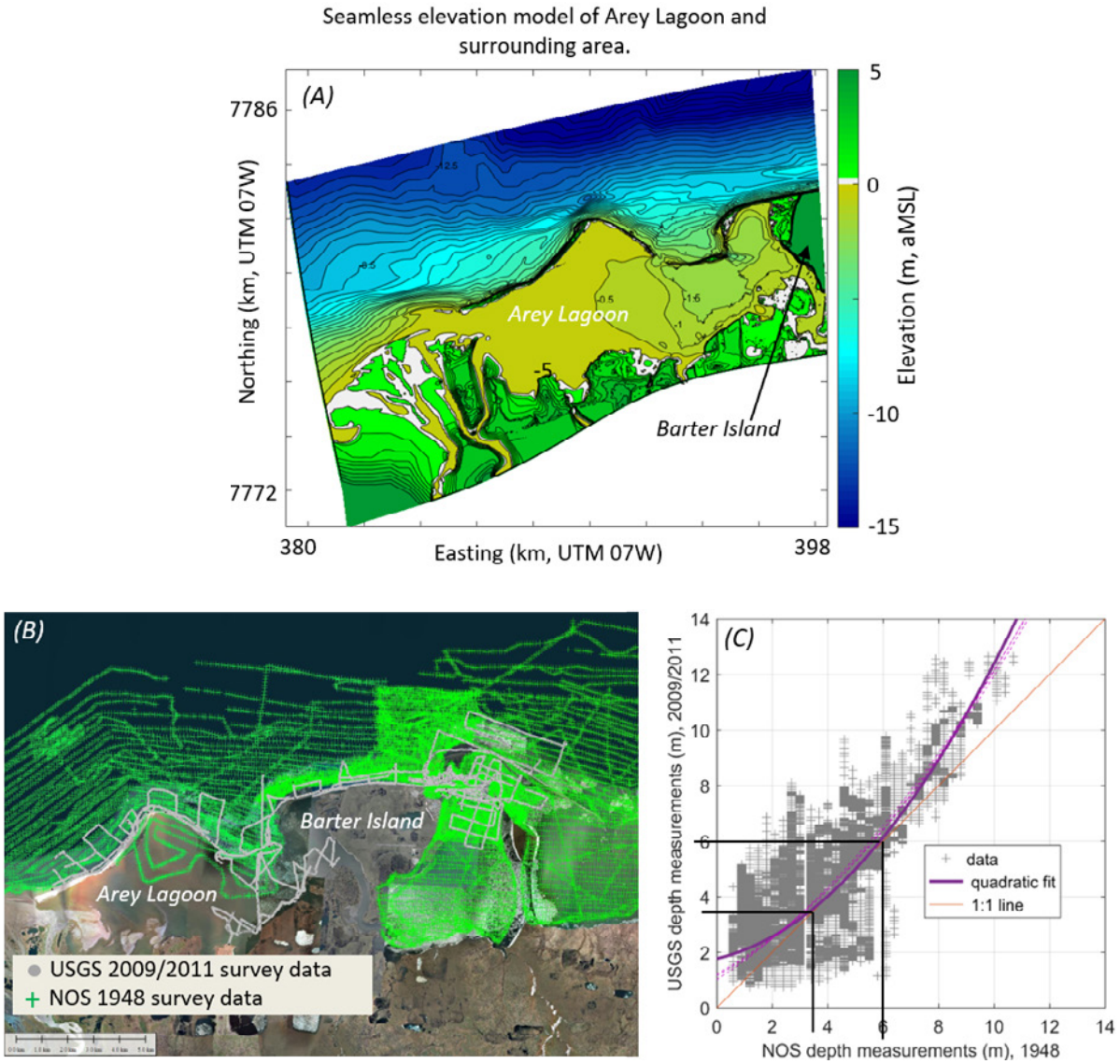

Figure 3.4. Maps and plots showing the elevation model of Arey Lagoon, Alaska, and surrounding area and hydrographic survey data used to generate the elevation model. *A*, Map of the seamless digital elevation model used in the high-resolution numerical model grids. *B*, Map showing individual sounding locations collected by National Oceanic Survey (NOS) circa 1948 and U.S. Geological Survey (USGS) in 2009 and 2011. *C*, Scatter plot comparing USGS surveyed depths to the nearest NOS-surveyed value within 300 meters. The solid purple line is a quadratic fit between the NOS and USGS survey data within 300 meters. Dashed purple lines are quadratic fits but with limited search radii of 100, 50, and 20 meters. The orange line depicts a perfect fit. Solid black lines highlight the range in which little change has occurred. km, kilometer; m, meter; aMSL, approximate mean sea level.

continental shelf to the local study area. The DEM shows a shallow lagoon and gently sloping nearshore area separated by the barrier island, which is broken by a few shallow channels (fig. 3.4). A shallow water canyon and adjacent ridge is evident on the seafloor to the west and north of the apex of Arey Island (at ~E386km, N7783km, UTM zone 07W). The canyon and ridge, among relatively shore-parallel bathymetric contours, provide a conduit for focusing of wave energy near the midpoint of the western section of Arey Island. West of Arey Island is an area of relatively steep nearshore topography.

USGS hydrographic survey data collected for this study were used to populate the shallower regions within the approximate 10–12-m depth contour as this depth range is most important for modeling nearshore wave transformation. Remaining regions were filled in with National Ocean Service (NOS) soundings (https://maps.ngdc.noaa.gov) collected in 1948 (the latest available data). NOS and USGS sounding locations are shown in figure 3*B*. NOS soundings are spaced approximately 100 and 300 m apart in the along-shore and cross-shore directions, respectively. USGS soundings are more tightly spaced but cover less area. Figure 3*C* compares measured USGS depths (shown as positive values) to the nearest NOS measurement within 300 m. The purple solid line shows a least-squares quadratic best-fit between the data. The quadratic fitted line in combination with the 1:1 "perfect fit line" indicates that, overall, the region has deepened except in the 3.5 to 6 m depth range where little change has occurred over the 1948 to 2009/2011 period. The purple dashed lines are best quadratic fits using collocated USGS/NOS data limited to 100, 50, and 20 m search radii. Because the purple solid and dashed lines are fairly similar, it is concluded that the comparison is robust and insensitive to the choice of search radii less than 300 m (cross-shore sampling distance of NOS survey data).

Arey Island topography is highlighted with the lidar-derived DEM in figure 3.5. Note the low-lying spits that border the eastern channel, the recurved spits at the island extremes and northern apex, and the elevation variation along the crest. Figure 3.6 is a plot of approximate maximum island crest elevation derived from the DEM along the length of the island. The northwest facing western part of the island contains the highest parts of the island, presumably the result of storm wave and wind deposition from storms approaching from the northwest. Maximum crest height is fairly uniform along most of the western section of the island (fig. 3.6) with the exception of an alongshore depression (<1 m height) in the vicinity of transect AR-09 near kilometer 388. The beach here is composed mostly of sand and gravel. Although there was no debris along the transect itself, debris was dispersed both east and west of the transect across the island, evidence of previous overwash events. Along the eastern section of the island, crest elevation decreases rapidly from the northern point to a breach in the approximate center. This is followed by a gradual elevation increase, with a maximum height of 1.7 m at the eastern terminus of the island.

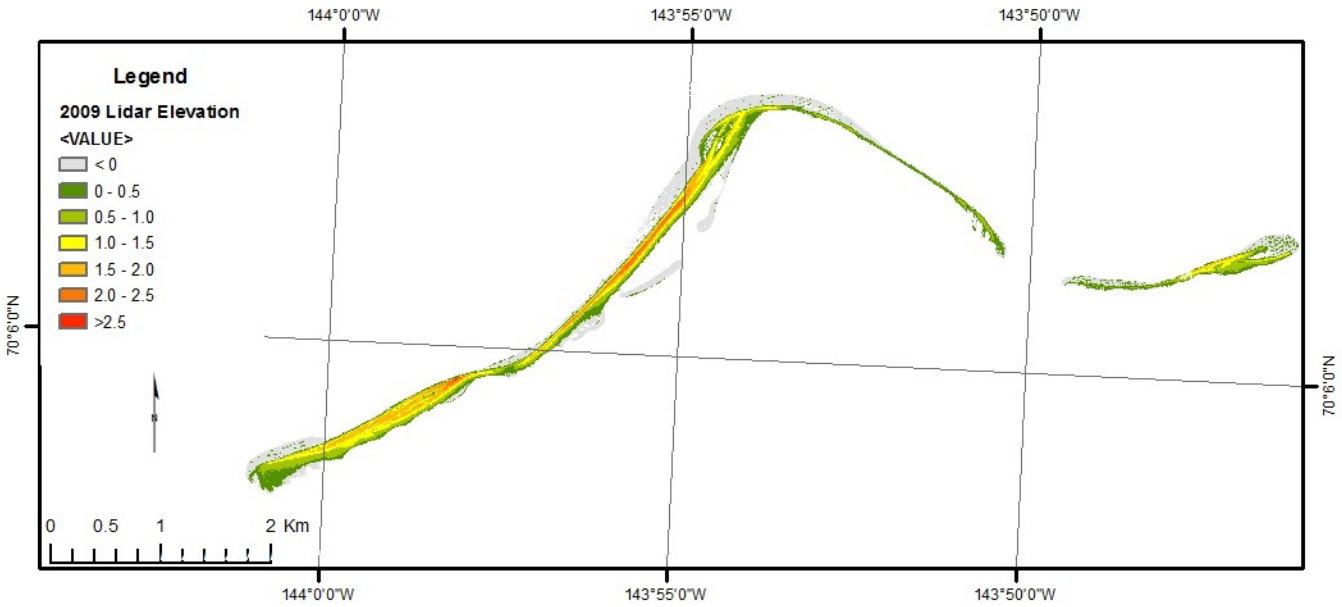

Figure 3.5. Map showing 2009 airborne lidar digital elevation model (DEM) of Arey Island, Alaska.

Detailed elevation data across Arey Island and western Barter Island spit transects (see fig. 3.3) are summarized in figure 3.7. Topographic transects across the western section of Arey Island on the Beaufort Sea side typically show a steep foreshore (4–7°; 7–12 percent grade) and beach face rising to the crest of the island with a gently lagoonward-sloping backbeach (1–3°; 2–5 percent grade). The southernmost profile at AR-11 (fig. 3.7*A*) shows a steep and well-developed seaward-facing beach face and crest that gradually descends uniformly to the lagoon shore. Evidence of seaward overwash extends over the crest to about 200 m inland. Near the apex of the island, at AR-04 (fig. 3.7B), two well-defined ridges are separated by a pond. The ridges have steep slopes toward the Beaufort Sea and mild slopes toward the lagoon side. Several

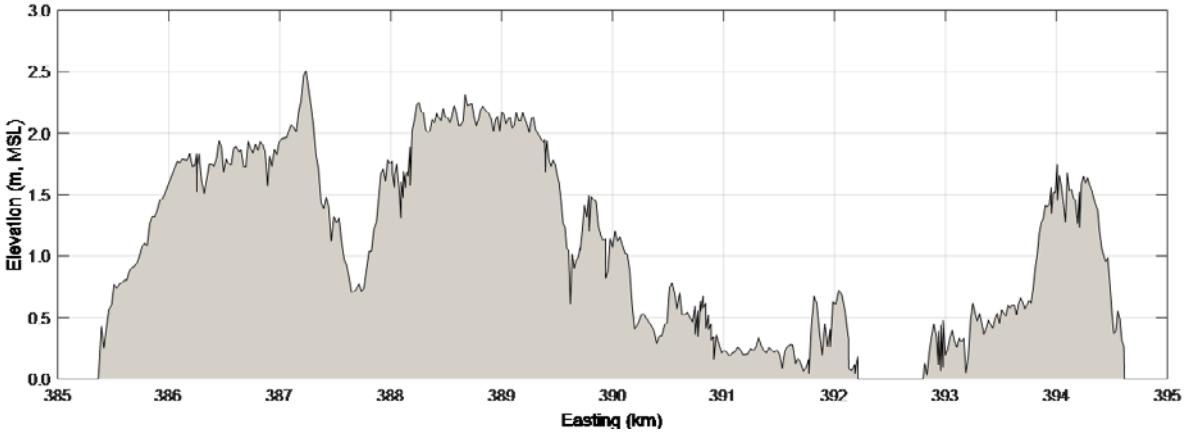

Figure 3.6. Plot of crest height along Arey Island, Alaska, derived from 2009 airborne lidar survey. m, meter; MSL, mean sea level.

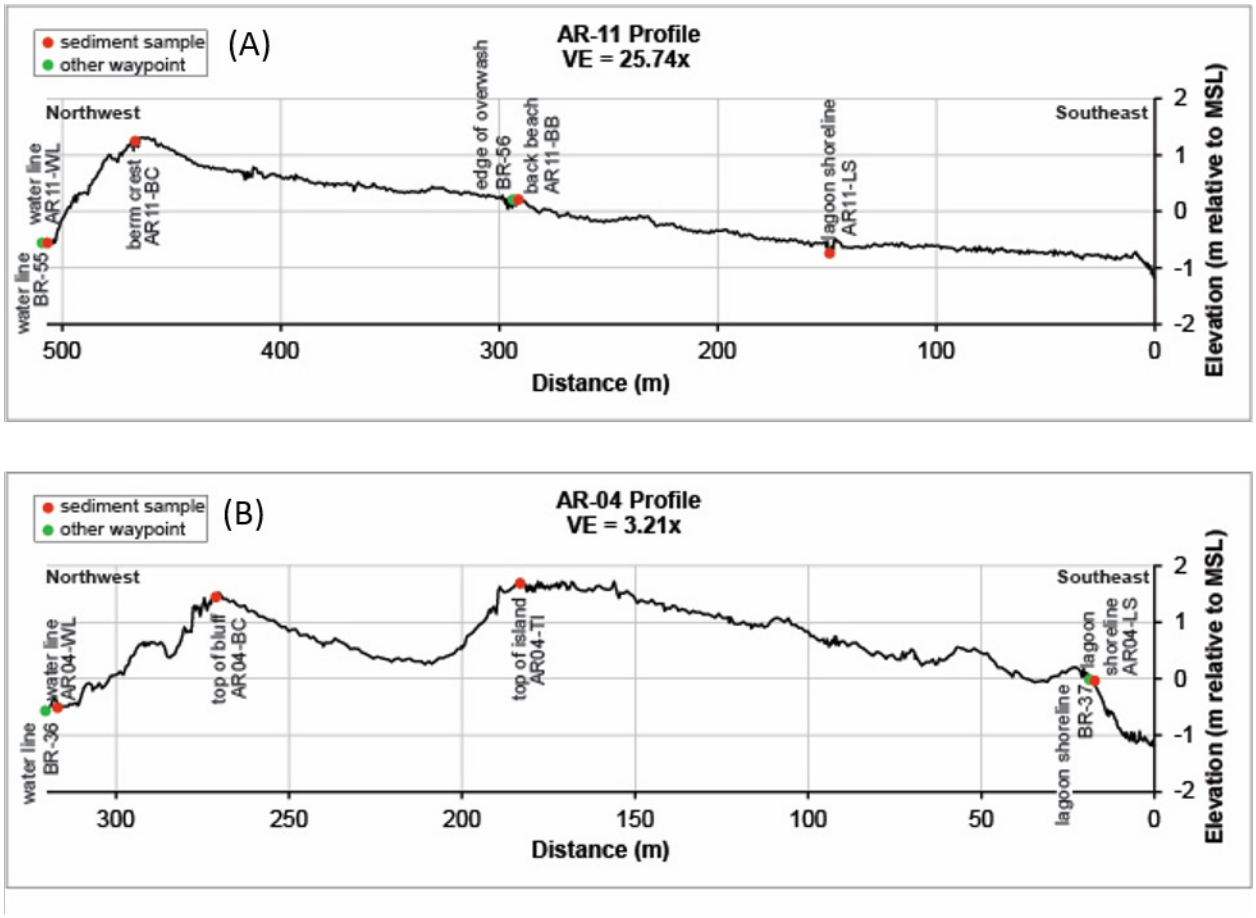

Figure 3.7 (pages 54–55). Selected cross-shore profiles at transects AR-11, AR-04, AR-03, and AR-02 along Arey Island and AR-15 at the west end spit of Barter Island, Alaska. See fig. 3.3 for profile locations. VE, vertical exaggeration; m, meter; MSL, mean sea level.

low-relief ridges are apparent on the foreshore of the most seaward crest as well on the lagoon shore.

Sparse to extensive vegetation mats were observed along the entire western section of the island and were primarily located on the lagoon side of the highest ridge. Much less vegetation was observed on the eastern section of Arey Island, and it extended as far east as transect AR-02 (fig. 3.7*D*). Debris wrack lines formed during overwash events were observed along most transects. Only at AR-07 and AR-08 and possibly AR-04, where the woody debris has been reworked by humans, were the wrack lines limited to the ocean side of the transect. All other transects indicate debris transport from both the lagoon side and from the seaward side. Cross-shore profiles on the eastern half of Arey Island tend to be relatively flat and without a steep foreshore as was seen on the western half (compare fig. 3.7*A*, *B* with *C*, *D*). The low relief, lack of vegetation, and irregular dispersal of debris indicate extensive flooding and overwash in this area where breaches have occurred in the past.

The eastern terminus of Arey Island appears to be very dynamic undergoing extensive overwash, erosion, and areas of accretion. Accretion of sediment in this area is likely the result

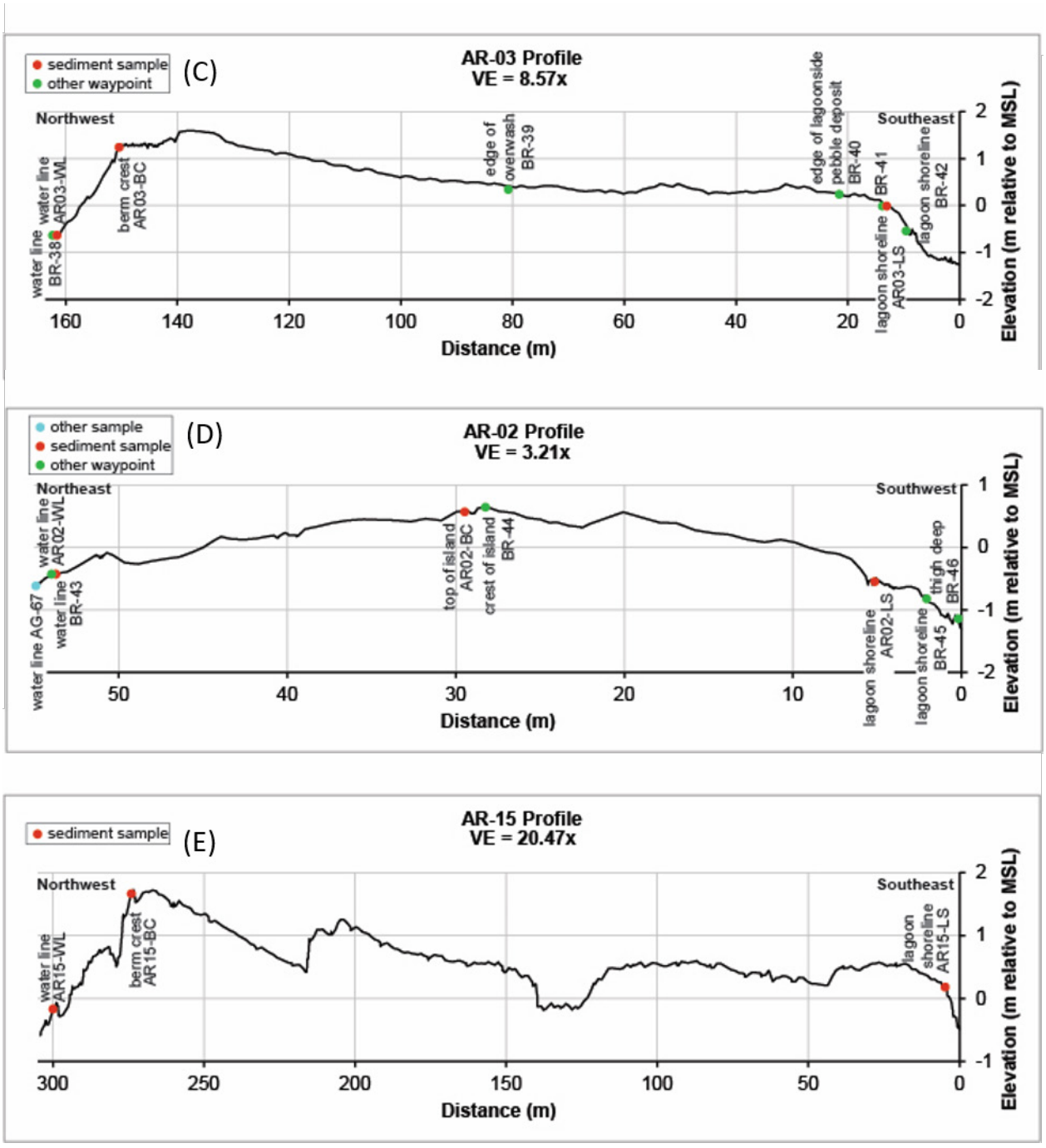

Figure 3.7 (pages 54–55).—Continued

of longshore sediment transport from the east (predominant wind and wave direction) that bypasses the claw-like western terminus of the sand spit attached to Barter Island. The cross-shore profile at AR-15 (fig. 3.7*E*) shows a low-relief, flat-lying section on the lagoon side and multiple ridges with steep faces on the seaward side. Claw-like recurved accretionary formations are ubiquitous at the western end of barrier islands and spits throughout the Alaskan Beaufort Sea coast. Hopkins and Hartz (1978) suggested that these features are formed by successions of storms that extend the western terminus of an island group westward past previously formed spits, protecting the older spit from further erosion by westerly storms. The succession of these accretionary spits result in a claw-like spur on the lagoon side.

Sediment Samples

Sediment samples collected within the lagoon, in the nearshore area of Arey Island, on Arey Island, and on the western Barter Island spit exhibited a wide array of class sizes ranging from clay and silt to gravel material (fig. 3.8*A*, *B*, and *C*). Coarse sediment ranged in size from 0.26 millimeters (mm) (medium sand) to greater than 12 mm (pebble). Table 3.3 summarizes the range and mean of the collected samples mean grain size. Table 3.4 presents sample and grain size information for each sample and table 3.5 presents results of two sieved samples.

Fine silt and clay were observed within the lagoon near the Aquadopp measurement site. Fine to medium sand (<0.5 mm) was found in the Beaufort Sea off the west end of Arey Island, near the delta, and off the east end of the northeast-facing section of Arey Island. Granule (>2 mm) to medium pebble-size (>8.0 mm) sediments were sampled in the near- and offshore areas at the apex of the barrier island (in other words, just northeast of the AWAC location shown in figure 3.1).

On Arey Island, samples were collected at the Beaufort Sea water line, the berm/island crest, and the shoreline on the lagoon side along each transect in figure 3.3. Overall, Arey Island consisted of fine and medium sand intermixed with lenses of pebbles and gravel (fig. 3.8). Medium-sized sand dominated near the termini with a fining toward the apex along the outer coast of Arey Island. The opposite pattern was observed on the lagoon side of the island, where the coarser material prevailed near the midpoint of the Island and a fining of material toward the east and west ends was observed. An exception to this general trend was the area in the vicinity of transect AR-10 where gravels were ubiquitous. The trend in fine and coarse material across the island is indicative of its dynamic nature, with the most active areas being those near the termini; the cause for the massive amounts of pebbles and gravels near the west end at AR-10 is unclear at this time but may be related to steeper offshore slopes which may allow large storm waves to focus energy in this area.

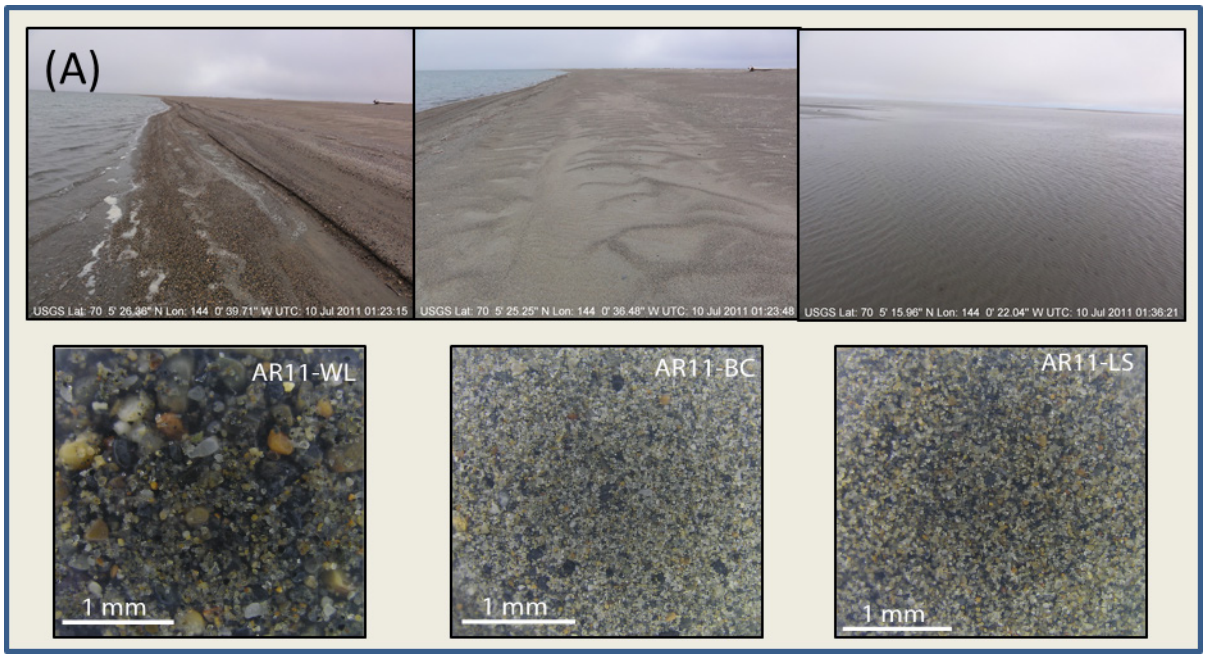

Figure 3.8 (pages 56—57). Photographs of views and sediment at three locations on Arey Island, Alaska: *A*, west end; *B*, apex; and *C*, east end. mm, millimeter

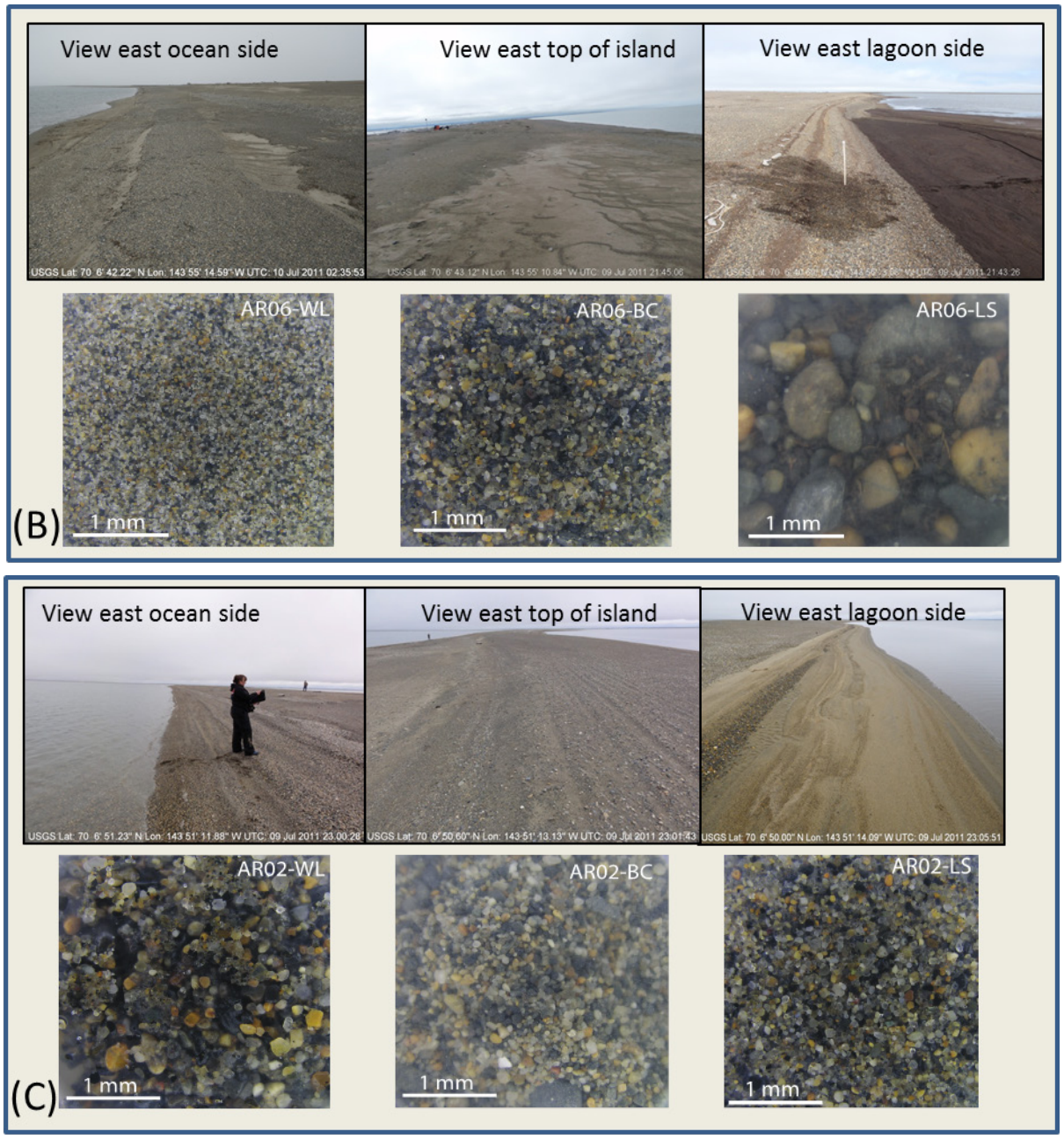

Figure 3.8 (pages 56—57).—Continued

Table 3.3. Summary of mean sediment grain sizes on Arey Barrier Island and nearshore region of Barter Island and Arey Lagoon, Alaska.

[mm, millimeter; BI, barrier island]

Location	Min (mm)	Max (mm)	Mean (mm)	Number of samples)
Overall	0.26	12.24	3.04	54
Marine	0.26	12.24	3.43	8
BI Beaufort Sea shore	0.79	3.70	2.10	14
BI berm crest	0.58	9.91	3.62	15
BI lagoon shore	1.15	9.47	3.50	13

Table 3.4. Description of sediment samples collected in the vicinity of Arey Lagoon and Arey Island, Alaska.

[See figs. 3.1 and 3.3 for locations. mm, millimeter. Latitude and longitude in decimal degrees (NAD83)]

Sample ID	Transect	Feature	Sample collection time	Latitude (N)	Longitude (W)	Mean grain size (mm)	Standard dev (mm)	Comments
				Barrier				
AR01-WL	AR01	Water line	2011-Jul-09 23:20:13	70.10946	143.83713	1.93	1.29	Poorly sorted
AR01-LS	AR01	Lagoon shoreline	2011-Jul-09 23:27:00	70.10926	143.84021	1.20	0.33	Mostly sands
AR01-BC	AR01	Top of island	2011-Jul-09 23:32:16	70.10943	143.83825	9.91	2.01	Coarse-grained mostly gravels
AR02-BC	AR02	Top of island/ berm crest	2011-Jul-09 23:07:19	70.11403	143.85362	2.46	0.24	Sands with larger pebbles
AR02-LS	AR02	Lagoon shoreline	2011-Jul-09 23:03:37	70.11388	143.85394	1.46	0.04	Coarse sands
AR02-WL	AR02	Water line	2011-Jul-09 22:57:05	70.11426	143.85333	2.77	0.10	Coarse sands
AR03-BC	AR03	Berm crest	2011-Jul-09 22:32:00	70.12018	143.90343	4.43	0.62	Poorly sorted sands to pebbles, sub-rounded grains
AR03-LS	AR03	Lagoon shore	2011-Jul-09 22:35:00	70.11924	143.90124	2.96	0.19	Sands
AR03-WL	AR03	Water line	2011-Jul-09 22:26:14	70.12026	143.90343	2.40	0.22	Coarse sands
AR04-TI	AR04	Top of island	2011-Jul-09 22:09:13	70.11888	143.90597	6.41	0.74	Very poorly sorted, large gravels
AR04-BC	AR04	Berm crest	2011-Jul-09 21:57:13	70.11961	143.90693	2.77	1.35	Sands to small gravels
AR04-WL	AR04	Water line	2011-Jul-09 21:53:36	70.11987	143.90762	2.01	0.24	Sands
AR05-BC	AR05	Top of island/ berm crest	2011-Jul-10 00:45:53	70.11806	143.90310	2.12	0.20	Sands, poorly sorted, some gravels
AR05-LS	AR05	Lagoon shoreline	2011-Jul-11 0:43:25	70.11487	143.90664	1.15	0.85	Fine-grained, clumpy
AR05-WL	AR05	Water line	2011-Jul-10-00:25:04	70.11693	143.91598	3.70	0.34	Poorly sorted
AR06-LS	AR06	Lagoon shoreline	2011-Jul-09 22:26:04	70.11125	143.91782	9.47	2.41	Coarse-grained with larger gravels and pebbles, some organics
AR06-WL*	AR06	Water line	2011-Jul-09 22:21:04	70.11188	143.92050	0.79	0.03	Well-sorted sands
AR06-BC	AR06	Berm crest	2011-Jul-09 22:23:05	70.11170	143.91993	1.77	0.40	Sands, some larger pebbles
AR07-WL	AR07	Water line	2011-Jul-09 23:14:00	70.10842	143.92862	2.01	0.17	Some larger grains
AR07-LS	AR07	Lagoon shoreline	2011-Jul-09 23:21:01	70.10763	143.92592	8.38	0.63	Coarse-grained, 100 percent gravels
AR07-BC	AR07	Berm crest	2011-Jul-09 23:19:03	70.10817	143.92773	1.43	0.02	Poorly sorted
AR09-LS	AR09	Lagoon shoreline	2011-Jul-10 01:01:35	70.09740	143.96177	5.22	1.20	Coarser, subangular grains
AR09-BC	AR09	Berm crest	2011-Jul-10 00:59:51	70.09790	143.96232	1.55	0.19	Sample moist

Table 3.4.—Continued

Sample ID	Transect	Feature	Sample collection time	Latitude (N)	Longitude (W)	Mean grain size (mm)	Standard dev (mm)	Comments
				Barrier—Continued				
AR09-WL	AR09	Water line	2011-Jul-10 00:58:22	70.09808	143.96245	3.07	0.20	Very coarse grains, mostly pebbles with some sands
AR11-BC	AR11	Berm crest	2011-Jul-10 01:41:53	70.09005	144.01030	0.58	0.07	Fine-grained
AR11-BB	AR11	Back beach	2011-Jul-10 01:56:16	70.08869	144.00878	2.15	0.58	Clumpy
AR11-LS	AR11	Lagoon shoreline	2011-Jul-10 01:56:17	70.08775	144.00620	2.66	0.17	Sample very moist
AR11-WL	AR11	Water line	2011-Jul-10 01:24:34	70.09041	144.01016	1.77	0.21	Coarse sands
AR12-BC	AR12	Berm crest	2011-Jul-10 21:06:02	70.10703	143.83298	2.87	0.10	Larger gravels and pebbles in sample
AR12-LS	AR12	Lagoon shoreline	2011-Jul-10 21:07:03	70.10682	143.83268	2.02	0.17	Sample moist
AR12-WL	AR12	Water line	2011-Jul-10 21:02:05	70.10713	143.83307	1.90	0.04	Coarse sands
AR13-BC	AR13	Berm crest	2011-Jul-10 21:38:02	70.10767	143.80050	6.42	1.31	Very poorly sorted, lots of medium to coarse gravels and pebbles
AR13-LS	AR13	Lagoon shoreline	2011-Jul-10 21:39:03	70.10743	143.80007	2.15	0.48	Poorly sorted sands to large gravels
AR13-WL	AR13	Water line	2011-Jul-10 21:34:01	70.10783	143.80072	1.54	0.17	Sands
AR14-WL	AR14	Water line	2011-Jul-10 21:58:04	70.11068	143.78200	1.85	0.44	Sample moist
AR14-LS	AR14	Lagoon shoreline	2011-Jul-10 22:06:03	70.10937	143.78013	6.18	0.40	Coarser, subangular grains
AR14-BC	AR14	Berm crest	2011-Jul-10 22:03:01	70.11053	143.78188	1.90	0.39	Sands with large gravels and pebbles
AR15-WL	AR15	Water line	2011-Jul-10 23:40:04	70.12232	143.77747	1.69	0.40	Coarse sands
AR15-LS	AR15	Lagoon shoreline	2011-Jul-10 23:58:01	70.12142	143.77075	1.27	0.09	Coarse grains
AR15-BC	AR15	Berm crest	2011-Jul-10 23:48:03	70.12217	143.77707	5.15	1.72	Largest grains excluded from photos
AR16-BC	AR16	Berm crest	2011-Jul-11 00:40:48	70.12755	143.75580	4.55	1.96	Sands, poorly sorted, some gravels
AR16-WL	AR16	Water line	2011-Jul-11 00:34:58	70.12778	143.75607	1.90	0.05	Sands
AR16-LS	AR16	Lagoon shoreline	2011-Jul-11 00:42:36	70.12695	143.75505	1.45	0.19	Coarse sands
LAGOON	AR28	Central lagoon	2011-Jul-10 23:48:47	70.09473	143.79155	0.72	0.56	Fine-grained, clumpy
				Marine				
WP 21*	AR02	Nearshore sediment sample near AR02 off of Arey Island	2011-Jul-06 07:36:26	70.11476	143.85437	0.35	0.10	Mostly silt to sand

Table 3.4.—Continued

Sample ID	Transect	Feature	Sample collection time	Latitude (N)	Longitude (W)	Mean grain size (mm)	Standard dev (mm)	Comments
Marine—Continued								
WP 5	AR03	Offshore sample near AR03 off apex of Arey Island	2011-Jul-06 05:05:35	70.12231	143.90062	8.21	0.71	Poorly sorted, larger gravels and pebbles
WP 4	AR03	Nearshore sample near AR03 off apex of Arey Island	2011-Jul-06 04:54:30	70.12081	143.90092	12.24	6.28	Poorly sorted, sands to pebbles
WP 15	AR09	Offshore sediment sample near AR09 off of Arey Island	2011-Jul-06 06:50:36	70.09896	143.96325	0.98	0.47	Silt, clumpy
WP 17	AR09	Nearshore sediment sample near AR09 off of Arey Island	2011-Jul-06 06:55:04	70.09812	143.96263	3.47	2.33	Poorly sorted, sands and large pebbles
WP 14	AR11	Far Offshore sediment sample near AR11 off west end of Arey Island	2011-Jul-06 06:24:44	70.09345	144.02151	1.08	1.23	Muds, clumpy
WP 12	AR11	Offshore sediment sample near AR11 off west end of Arey Island	2011-Jul-06 06:19:57	70.09179	144.02005	0.26	0.00	Muds, clumpy
WP 10	AR11	Nearshore sample near AR11 off west end Arey Island	2011-Jul-06 06:10:17	70.09029	144.01757	0.99	0.19	Fine-grained, well-sorted
Oceanographic instrument package sites								
Aquadopp		Aquadopp site	2011-Jul-11 00:12:54	70.10401	143.82829	1.68	0.73	Very fine grained, clay
AWAC		AWAC site	2011-Jul-07 06:50:41	70.11687	143.92597	2.71	1.65	Large clumps, muds

*Sieved samples.

Table 3.5. Properties of sieved sediment samples at two representative sites on Arey Island, Alaska.

[See fig. 3.3 for locations. Cum., cumulative; g, gram; mm, millimeter]

Sieve size	Phi	Sieve size (mm)	Weight retained (g)	Cum. weight retained (g)	Cum. percent
AR02-NS	Sample Weight (g): 233.0				
10	-1	2.000	31.0	31.0	13.3
18	0	1.000	3.3	34.3	14.8
35	1	0.500	9.0	43.3	18.6
60	2	0.250	34.7	78.0	33.6
120	3	0.125	99.2	177.2	76.2
Pan	5		55.2	232.4	100.0
Error			99.7		
Est. Mean	2.226	0.213			
AR06-WL	Sample Weight (g): 399.4				
10	-1	2.000	0.1	0.1	0.0
18	0	1.000	0.6	0.7	0.2
35	1	0.500	15.9	16.6	4.2
60	2	0.250	328.0	344.6	86.5
120	3	0.125	53.4	398.0	99.9
Pan	5		0.5	398.5	100.0
Error			99.8		
Est. Mean	1.553	0.340			

Hydrodynamic Observations

Hydrodynamic wave and current measurements obtained offshore of Arey Island and within the lagoon (AWAC and Aquadopp sites, respectively, fig. 3.1) show that it was a relatively low-energy environment during the 2011 open-water season. A maximum significant wave height of 0.98 m with a peak period of 7.7 s was measured on September 20, 2011 (fig. 3.9), at the AWAC site, located 500 m offshore of Arey Island. The largest waves measured were predominantly from the northwest to north with peak periods in the range of 4 to 8 s.

Wave heights within the lagoon were less than 0.10 m with no dominant direction (data not shown). The maximum fetch within the lagoon to the measurement site is on the order of 6.3 km. This relatively short distance hinders the development of substantial wave heights and lengths, generally limiting waves to chop within the lagoon, which was not captured with the measurement instruments.

Maximum near-seabed current speeds reached 69 and 38 cm/s at the offshore and lagoon sites, respectively (fig. 3.9*B*). At the offshore (AWAC) site, current directions were modified by the local bathymetry and barrier island geometry, resulting in on- and alongshore flow to the southwest in the upper water column and south-southwest near the seabed. Measured bottom currents indicate that the dominant alongshore transport direction is toward the southwest (fig. 3.10). The maximum current speeds reached during the deployment at the AWAC site were theoretically (employing, for example relationships developed by Soulsby, 1997) capable of entraining (picking up sediment off the seabed and initiating motion) and transporting pebbles and medium sized gravels, such as those observed on Arey Island. Directions associated with the maximum currents measured at the AWAC site were also toward the SSW. Maximum current speeds measured near the seabed at the Aquadopp site inside the lagoon were only slightly more than half the magnitude measured offshore. Although these currents are not of the critical velocities required to entrain and transport larger sediment fractions, they are capable of transporting medium to coarse sands.

Water-level deviations ranged from a minimum of -0.36 to +0.46 m from the mean at the AWAC site. Very similar water-level fluctuations were measured at the Aquadopp site (fig. 3.11*A*). A low-pass filter was applied to the lagoon Aquadopp data to separate the tide signal from non-tidal residuals

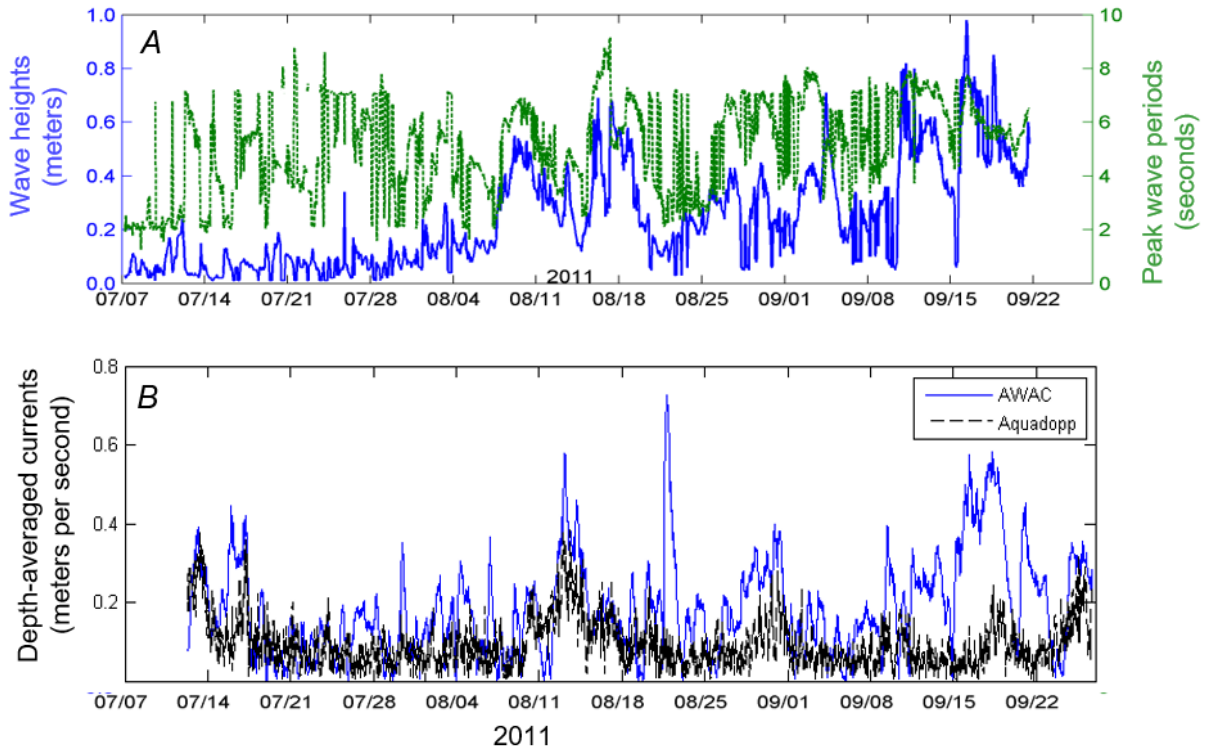

Figure 3.9. Time-series plots of measured wave parameters and currents, July 7 through September 22, 2011. A, Significant wave height and peak period as measured with the AWAC deployed on the Beaufort Sea side of Arey Island, Alaska. B, Depth averaged currents at the AWAC (Beaufort Sea side of Arey Island) and Aquadopp (within Arey Lagoon) sites.

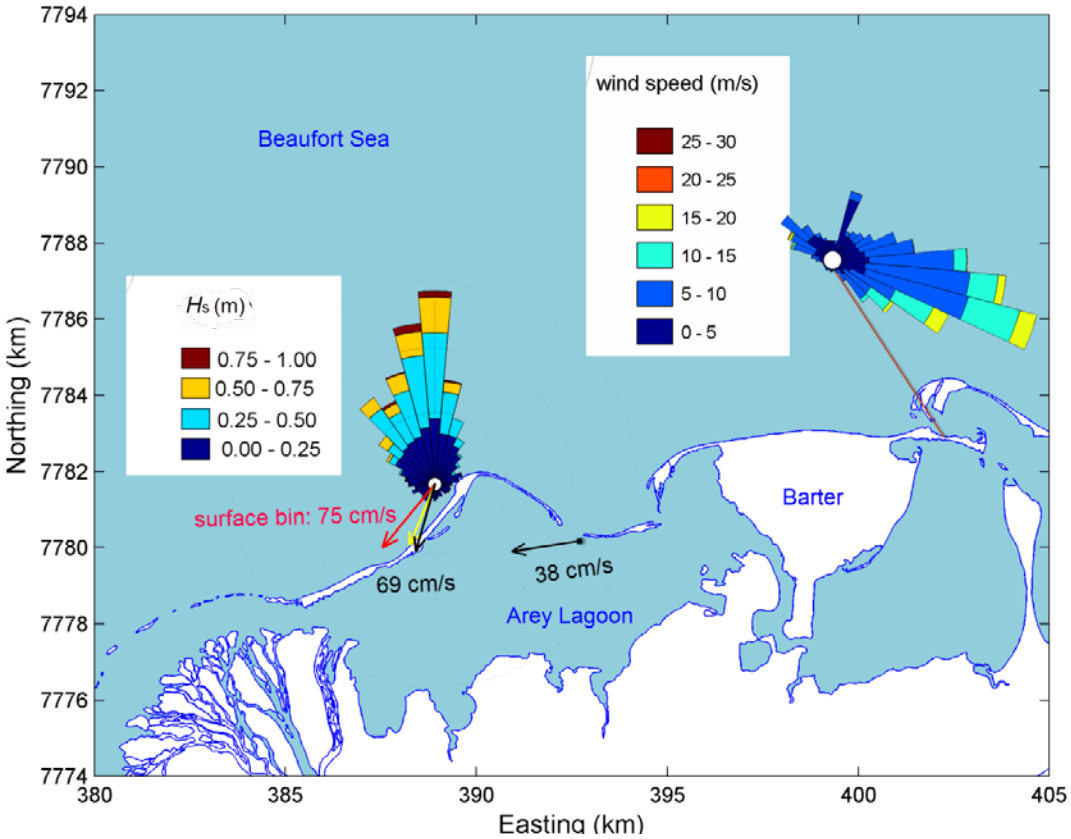

Figure 3.10 Spatial summary plot of measured waves and currents within Arey Lagoon and immediately offshore of Arey Island, Alaska. Roses show direction that waves and winds came from. Wind rose depicts wind magnitude and direction measured at Barter Island Airport (lat. 70.133° N., long. 143.576° W.) during the deployment period. Vectors depict direction (going to) and magnitude of mean measured currents near the surface (red vector) at the middle of the water column (yellow) and near the seabed (black). Because the measurement site inside the lagoon was shallow (1.2 meters [m]), currents were only measured in the bottom bin near the seabed at this site. km, kilometer; m/s, meter per second; cm/s, centimeter per second.

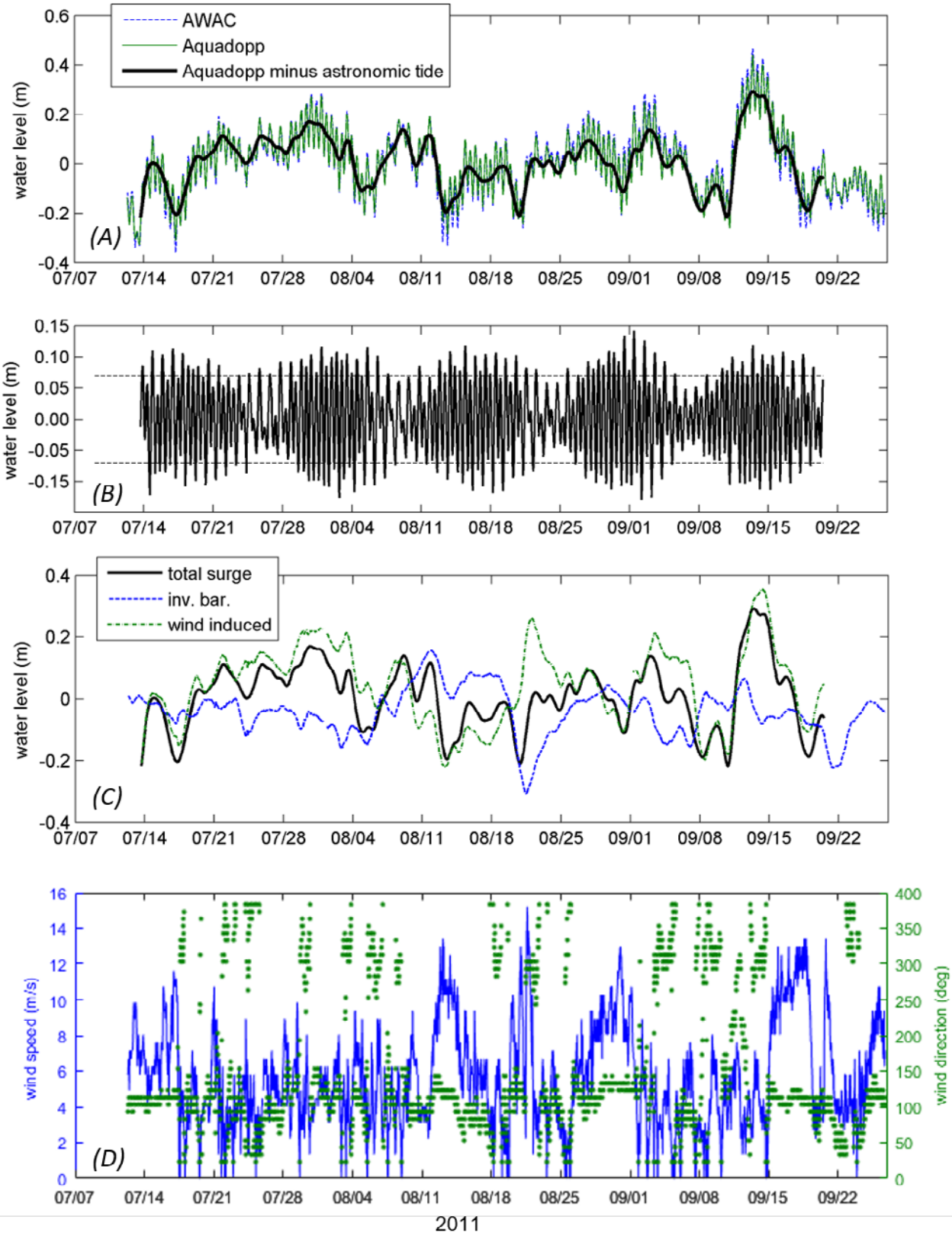

Figure 3.11. Time-series plots of measurements collected offshore of Arey Island, Alaska (AWAC), and in the lagoon (Aquadopp). The overall mean of the time-series has been removed to highlight water-level deviations from the mean. *A*, time-series of total water levels and the low-pass filtered signal at Aquadopp site. *B*, Extracted astronomic tide variations. *C*, Low-pass filtered signal showing total surge and inverse barometer (inv. bar.) and wind-induced components. *D*, Windspeed and direction (National Climatic Data Center, 2013). m, meter; m/s, meter per second; deg, degree.

associated with surge and circulation patterns. Recorded tides were semi-diurnal with a maximum and mean range (peak to trough) of 0.25 and 0.14 m, respectively. Mean high water (MHW), mean low water (MLW), mean higher high water (MHHW), and mean lower low water (MLLW) values were ±0.07 and ±0.10 m, respectively (fig. 3.11*B*). These tide statistics are approximations based on a relatively short time-series (76.4 days) and referenced to the mean water level measured over the duration of the deployment. It is noted that these approximations are not equivalent to the standards of the National Oceanic and Atmospheric Administration (NOAA) tide gauge measurements and calculations, which, to be accurate, require a full epoch (18.6 years) of water-level measurements.

The low-pass filtered signal, which is presumably mostly associated with surge, is shown with the solid black line in figure 3.11*A* and *C*. Surge is primarily the result of three physical processes: (1) a rise or lowering of water levels associated with atmospheric pressure changes ("inverse barometer effect" [IBE]), (2) a rise or lowering of water levels associated with wind setup or setdown in response to wind-drag over open water (static surge), and (3) a rise of water levels associated with the speed at which an atmospheric low-pressure system moves (dynamic surge). IBE is a function of atmospheric pressure gradients that physically draw water levels up in regions of lower pressure and physically push water levels down in regions of higher pressure. IBE is largely independent of bathymetry but continues to act on a given water body even under conditions of sea ice (for example, Wise and others 1981). Water-level variations in response to atmospheric pressure changes (h_{IBE}) can be estimated with the following equation

$$h_{IBE} = \frac{\Delta P}{\rho g} \quad (3.1)$$

where

r is water density (~1,025 kg/m^3),

g is the gravitational acceleration (9.83 m/s^2 at lat. 70.5° N.), and

ΔP is the difference between local and average atmospheric pressures.

Based on equation 3.1, a 100 pascal (Pa) (1 millibar [mbar]) drop in atmospheric pressure can be expected to produce a water level rise of 1 cm. Station pressures (near sea level) have been recorded at the Barter Island airport since 2005 (NOAA, 2016) and were used to estimate the IBE component of the measured surge. The greatest pressure drop thus far recorded was 97.49 kilopascal [kPa] in December 2005 (compared to a mean of 101.2 kPa), corresponding to a water level rise of ~0.15m.

The overall maximum water level recorded at the Aquadopp site (in the lagoon) was +0.29 m on September 13, 2011, and slightly higher at the offshore site (+0.32 m). Sustained winds, recorded at Barter Island Airport 14 km to the east of Arey Lagoon, were on the order of 7 m/s from the west and northwest during several days preceding the relatively higher water levels in mid-September.

Temperature and Salinity Variations

Offshore (AWAC) and Lagoon (Aquadopp) Sites

Comparison between near surface and lower water column temperatures indicate strong stratification under conditions of low wave energy at both the offshore and lagoon measurement sites. Near-surface water temperatures at the deeper (~5 m) offshore site varied from -6.5 °C to as much as 12.8 °C, while overall, temperatures near the seabed increased gradually from -1.7 to -0.6 °C, during the first half of the measurement period from July to mid-August (fig. 3.12). During the latter half of the measurement period, from August 11, 2011, onward, temperature differences between the upper and lower water column were generally less than 1 °C.

Temperatures varied daily near the seabed at the lagoon site, and similar to the offshore site, the variations were limited to the first half of the measurement period from July to mid-August (fig. 3.12*B*). During this time, temperatures ranged from 0.1 °C to as much as 11.3 °C and with a strong diurnal signal, reflecting the long days of the Arctic summer and shallow water depths of the lagoon (~1 m). When air temperatures dropped in mid-August to an average of 5 °C over the remaining measurement period, the diurnal response decreased and eventually ceased as the hours of daylight decreased. From September 15, 2011, to the end of the measurement period, near surface and seabed water temperatures responded in unison to decreasing air temperatures, eventually yielding shorefast ice formation.

The change from a stratified to a well-mixed water column in mid-August, at both the offshore and lagoon sites, coincided with a drop in air temperatures and increased wave energy measured at the offshore site (fig. 3.9). Average air temperatures were 6.7±1.7 °C with a maximum of 14 °C during the first half of the measurement campaign and dropped to an average of 3.4±1.9 °C for the latter part. Wave energy was extremely low (typically significant wave heights <0.20 m) during the first half of the measurement period and thus imparted little energy for mixing of the water column. Although wave energy was still relatively low from mid-August through September (maximum significant wave heights of 0.98 m), it more than doubled compared to the earlier part of the season.

Salinity concentrations computed from conductivity measurements near the seabed at the offshore (AWAC) site were fairly constant at ~36 practical salinity units (psu) with the exception of two events in August and mid-September 2011 (fig. 3.12*C*). The rather high salinity levels are likely due to the accumulation of salt rejected from growing sea ice. An abrupt saline decrease was measured at the lagoon site and coincident with the timing of a rapid increase of salinity concentrations to relative background conditions at the offshore site. Influence of the freshwater from the Hulahula River to the southwest is unlikely as the larger peak in discharge recorded at the newly installed gauge on Hulahula River (USGS gauge 15980000, https://waterdata.usgs.gov) did not result in a

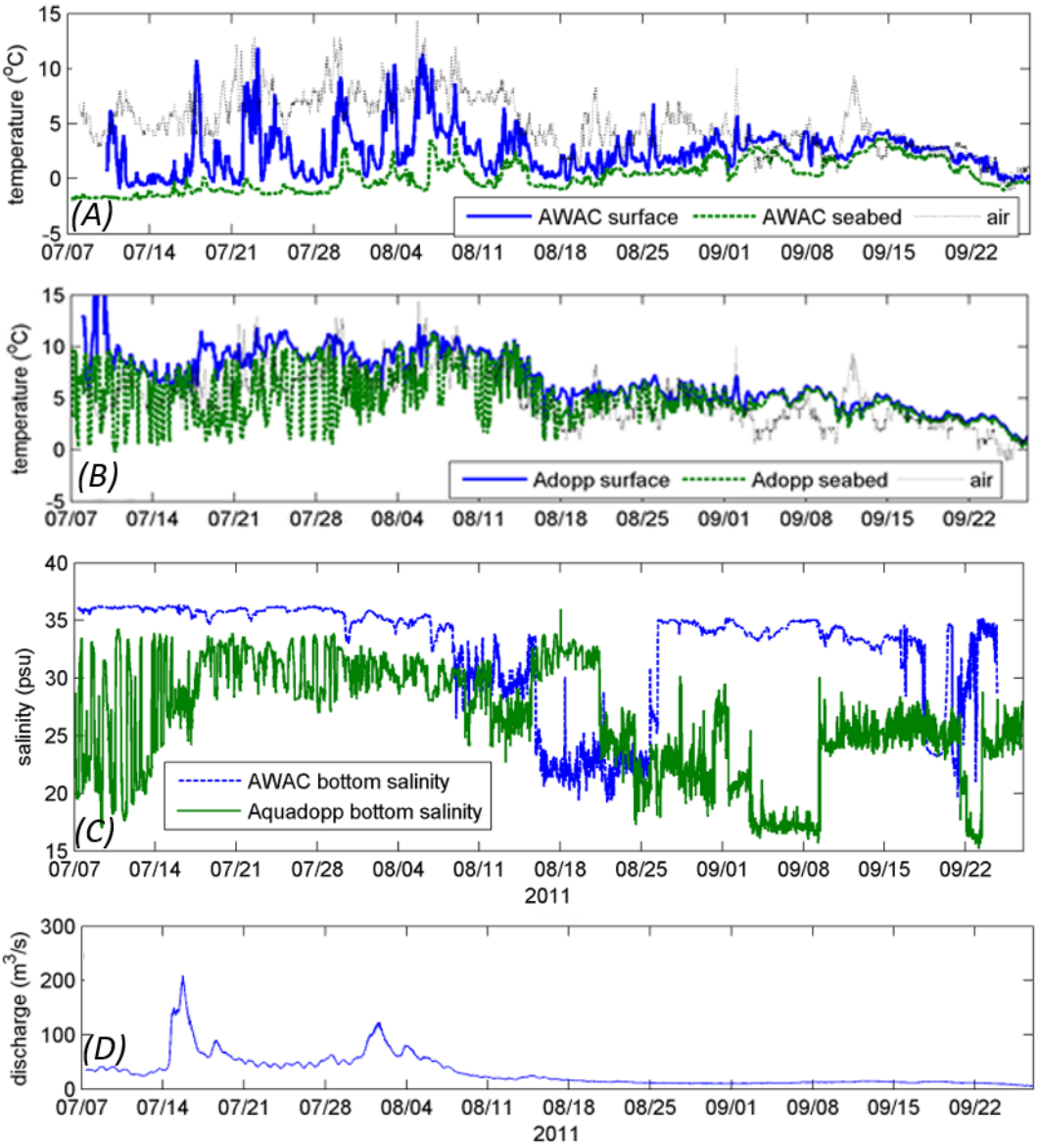

Figure 3.12. Temperatures and salinity concentrations at the AWAC site located offshore of Arey Island and at the Aquadopp site within Arey Lagoon, Alaska. *A* and *B*, Upper and lower water column water temperatures measured at the AWAC and Aquadopp sites, respectively. Air temperatures measured at the Barter Island airport 12 km east-northeast are also shown for reference (gray lines). *C*, Lower water column salinity concentrations at the two sites. Data from August 8, 2011, forward are likely affected by instrument clogging and may not represent true conditions. *D*, Freshwater discharge from the Hulahula River (Arctic Landscape Conservation Cooperative and U.S. Geological Survey, 2013). psu, practical salinity units; m^3/s, cubic meter per second.

salinity drop, and overall, the quantities of freshwater discharge were fairly low (fig. 3.12*D*). There was no shorefast ice in the vicinity of the instrument sites at the time of deployment, but wind-blown icefloes could have been present during the measurement period. It is possible that an icefloe may have been grounded and released large amounts of freshwater as it melted, but based on personal accounts of local residents, the presence of nearshore icefloes in August of 2011 was not very likely. Rather, the coincidence of higher wave energy and abrupt drops in salinity lead us to believe that the instruments may have been temporarily clogged owing to stirring of bottom sediment associated with increased wave activity.

Barrier Island Focus Study Site

The depth to permafrost on Arey Island was investigated by probing a 1.0-m-long pole through the sediment at various places in early July 2011. No permafrost layer was identified using this method, suggesting that the active layer was at least 1 m thick. A ground-temperature array installed on the lagoon side of the barrier island showed a decrease in temperature with depth (fig. 3.13); average values ranged from 7.3 to 5.1 °C between 10 and 50 cm below the surface. Cross-correlation analysis indicates that ground temperatures at 50-cm depth lagged air temperatures by approximately 4 hours. The reason for the abrupt temperature increase at the 50-cm-deep gauge on July 30, 2011, is unknown at this time, but suggests that the thermistor was exposed to air for several days. The thermistor array at this site was found horizontal on the beach and apparently was extruded from the soil in early September, as indicated by the similarity between thermistor and air temperature measurements over the latter part of the record.

Wet Sedge Focus Study Site

Conductivity, temperature, and depth (CTD) measurements in one of the ponds within the wet sedge study site (fig. 3.14) adjacent to Arey Lagoon revealed some interesting processes. Salinity measurements show a strong positive

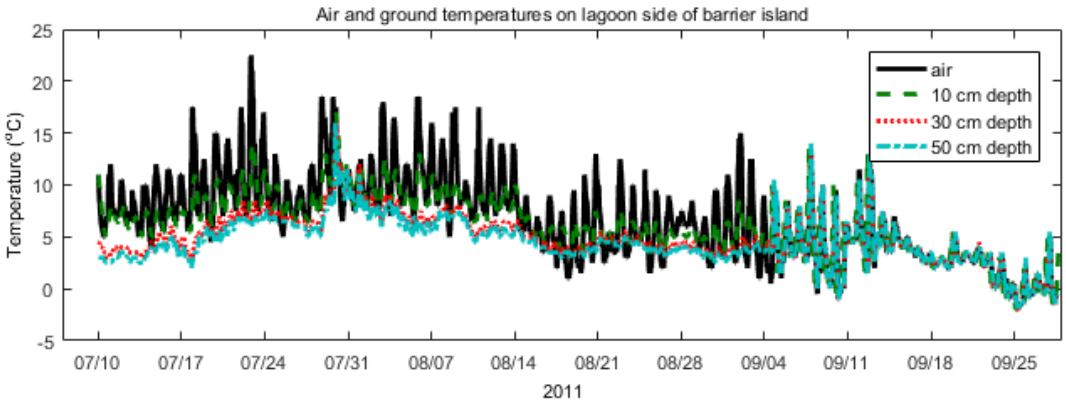

Figure 3.13. Plot of air and ground temperatures on lagoon side of Arey Island, Alaska.

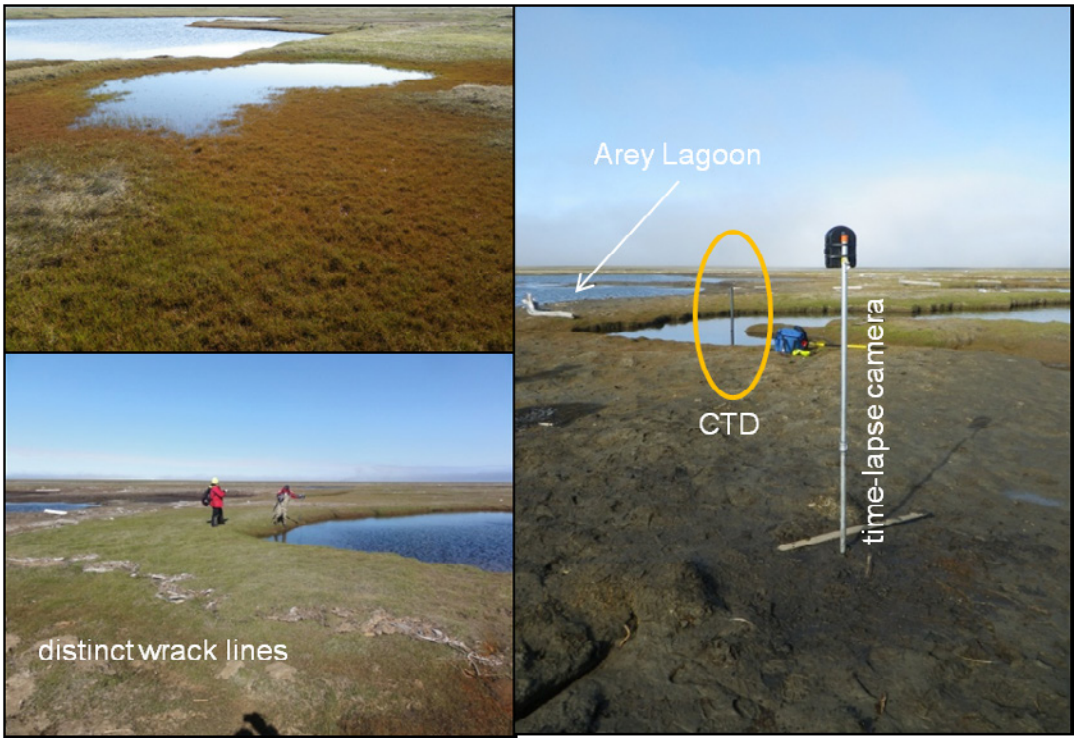

Figure 3.14. Photographs of the wet sedge focus study site near Arey Lagoon, Alaska. Distinct debris wrack lines (lower left panel) were observed throughout the area. Wetland grasses are common along the edges of several of the ponds. A time lapse camera station and conductivity, temperature, and depth (CTD) monitor were established near a pond adjacent to Arey Lagoon (right panel).

trend, with salinity increasing from 15 to more than 40 psu between July 9 and September 25, 2011 (fig. 3.15). This trend was inversely correlated with water temperatures when the temperatures approached the freezing point around September 9, 2011, and likely caused separation of freshwater and brine development. Afterwards salinity continued to increase as temperatures fell. Water temperatures were strongly modulated by air temperatures but, owing to the high heat capacity of water and delayed thermal release, showed an average absolute difference of 2 °C compared to corresponding air temperatures.

Pond salinity values start increasing gradually around the end of July, during open-water season, raising the possibility that the increase was due to evaporation. Estimates of freshwater evaporation (, in mm/d) were made using the modified pan evaporation Penman equation (Shuttleworth, 1993):

$$E_P = \frac{\Delta A' + \gamma[6.43(1+0.536U_2 D)])}{\lambda(\Delta+\gamma)} \qquad (3.2)$$

where

- λ (=2.501-0.002361T) is the latent heat of vaporization of water (in megajoules per kilogram [MJ/kg]), with T representing the air temperature in degrees Celsius;
- Δ is the rate of change of saturated vapor pressure (in kPa/°C) at air temperature;
- A' is the measured or estimated energy available for evaporation of the free water surface expressed as an evaporated water equivalent (mm/d);
- U_2 is the windspeed at 2 m height (m/s);
- D is the vapor pressure deficit (kPa); and
- γ is the psychometric "constant" (=0.0016286 P/γ, kPa/ºC) where P is the atmospheric pressure (kPa).

Studies have shown that evaporation from a natural body of water is usually lower compared to evaporation from a pan where the metal sides affect evaporation. Most textbooks suggest multiplying the pan evaporation by 0.75 to correct for this.

Cumulative volumetric evaporation, calculated with equation 3.2 using measurements at the Barter Island airport and multiplied by the 0.75 correction factor and area of the pond (380 m^2), is plotted with red lines in figure 3.15*B*. Least-squares best-fit lines to the salinity and volumetric evaporation time-series yield similar slopes of 0.40 psu/d and 0.42 m^3/d, respectively. The similar rates suggest that the increase in salinity may have been due in part to evaporative losses. Simple calculations indicate that about 16 m^3 (0.42 m^3/d×37 d) of freshwater was lost owing to evaporation over the measurement period prior to temporary sensor clogging on August 21, 2011, and prior to water temperatures dipping below 4 °C when brine development begins. The pond was shallow, with an estimated depth of ~0.35 m where the water-level gauge was located. Assuming the pond shape can be represented by a sector of a sphere, a rough estimate of the total volume (V) is 90 m^3 (V=(2/3)πr^2, where r is the radius and h is the maximum depth, assumed to be equal to the measured depth).

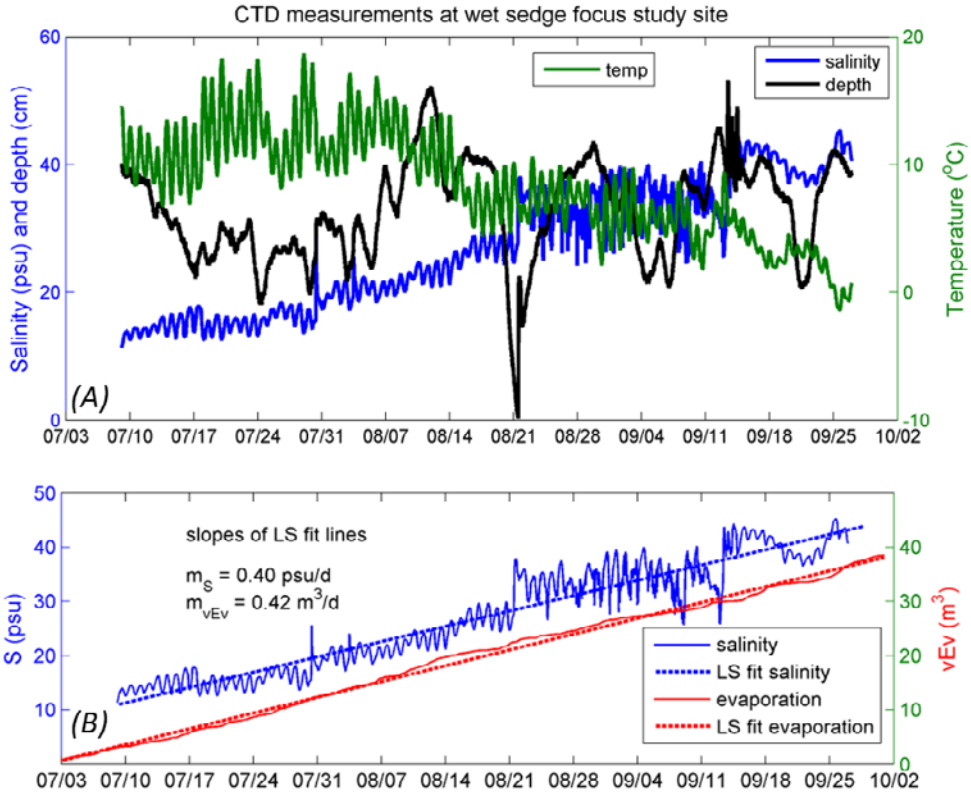

Figure 3.15. Conductivity, temperature, and depth (CTD) measurements within the pond at the wet sedge study site on the southeast shore of Arey Lagoon, Alaska. *A*, Salinity, temperature, and water depth measurements. The apparent depth decreases to 0 m on August 21, 2011, likely was due to a transient blockage in the sensor. *B*, Calculated cumulative volumetric pond evaporation (vEv) and measured salinity values. Least squares linear regression best-fit lines yield similar rates of salinity increase and pond evaporation (0.40 psu/d and 0.42 m^3/d, respectively). psu, practical salinity unit; d, day; cm, centimeter; m^3, cubic meter.

If salinity concentrations increased solely owing to evaporation, then approximately 20 percent (~16/90 m^3) of the pond volume would have been lost. However, there was no clear decrease in the average water depth within the pond, although water levels varied (±8 cm) in response to wind and barometric pressure changes. Thus, either volumetric estimates of pond water and (or) evaporative losses are inaccurate, or other processes also contributed to the observed salinity increases and relatively constant water balance. Because the area is of very low relief it is quite possible that saline lagoon waters overwash into the pond during storm events. The time-lapse camera unfortunately ceased working prior to the higher water levels measured in September and thus cannot be used to verify this hypothesis. However, camera images showed lagoon waters encroaching the pond during rises in lagoon waters as small as 10 cm in July 2011. Although no overwash was evident, the observations suggest that slightly higher lagoon water levels could overtop the land area between the lagoon and pond, resulting in spillover of saline water into the pond. These observations, supplemented by brackish pond-water measurements (not shown) and documented wrack (debris) lines across the wet sedge peninsula strongly indicate that the area was historically inundated, as shown with the numerical model results presented in the main text of this report.

References Cited

Barnard, P.L., Rubin, D.M., Harney, J., and Mustain, N., 2007, Field test comparison of an autocorrelation technique for determining grain size using a digital 'beachball' camera versus traditional methods: Sedimentary Geology, v. 201, p. 180–195.

Buscombe, D., Rubin, D.M., and Warrick, J.A., 2010, A universal approximation of grain size from images of noncohesive sediment: Journal of Geophysical Research, v. 115, no. F02, 17 p., https://doi.org/10.1029/2009JF001477.

Erikson, L.H., Gibbs, A.E., Richmond, B.M., Jones, B.M., Storlazzi, C.D., and Ohman, K.A., 2020, Modeled 21st century storm surge, waves, and coastal flood hazards, and supporting oceanographic and geological field data (2010 and 2011) for Arey and Barter Islands, Alaska and vicinity: U.S. Geological Survey data release, https://doi.org/10.5066/P9LGYO2Q.

Gibbs, A.E., and Richmond, B.M., 2015, National assessment of shoreline change—Historical shoreline change along the north coast of Alaska, U.S.–Canadian border to Icy Cape: U.S. Geological Survey Open-File Report 2015–1048, 96 p., https://doi.org/10.3133/ofr20151048.

Hopkins D.M., and Hartz, R.W., 1978, Coastal morphology, coastal erosion, and barrier islands of the Beaufort Sea, Alaska: U.S. Geological Survey Open-File Report 78–1063, 54 p.

Jorgenson, M.T., J.E. Roth, E.R. Pullman, R.M. Burgess, M.K. Raynolds, A.A. Stickney, M.D. Smith, and T.M. Zimmer. 1996. An ecological land survey for the Colville River Delta, Alaska. Final Report prepared for ARCO Alaska, Inc. Kuukpik Unit Owners. ABR, Inc. Fairbanks, AK.

National Climatic Data Center, 2013, Local Climatological Data (LCD): Tides and Currents web page accessed January 2013 at http://www.ncdc.noaa.gov/data-access/land-based-station-data/land-based-datasets/quality-controlled-local-climatological-data-qclcd.

National Oceanic and Atmospheric Administration, 2012, Bathymetry, National Geophysical Data Center database, accessed September 2012 at https://maps.ngdc.noaa.gov/viewers/bathymetry/.

National Oceanic and Atmospheric Administration, 2016, Prudhoe Bay, AK—Station ID 9497645: Tides and currents database, accessed April 2016 at http://tidesandcurrents.noaa.gov/geo.shtml?location=9497645.

Shuttleworth, W.J., 1993, Putting the 'vap' into evaporation: Hydrology and Earth System Sciences, v. 11, no. 1, p. 210–244,

Soulsby, R., 1997, Dynamics of Marine Sands: London, Thomas Telford Publications, 245 p.

Wise, J.L., Comiskey, A.L., and Becker, R., 1981, Storm surge climatology and forecasting in Alaska: Anchorage, Alaska, University of Alaska, Arctic Environmental Information and Data Center.

Moffett Field Publishing Service Center, California
Manuscript approved for publication December 7, 2020
Edited by Regan Austin
Layout by Kimber Petersen

ISSN 2331-1258 (online)
https://doi.org/10.3133/ofr20201142